PHYSICS

THE APPLICATION OF THE TDI METHOD TO OBSERVATIONS OF LUNAR OCCULTATIONS

LASZLO STURMANN

Dissertation under the direction of Professor David A. Weintraub

In my dissertation, I discuss how the time delay integration (TDI) method can be applied to observations of lunar occultations. The TDI method allows us to track the diffraction pattern of an occulted star by stepping the photon-generated charge packages in a CCD array placed in the pupil plane of a large telescope. The use of TDI should considerably improve the signal-to-noise ratio that can be reached in occultation observations compared with that which can be obtained currently using conventional high-speed photometers. This novel method could extend lunar occultation studies to faint stars and telescopes with large apertures without the aperture distortion effect inherent in the conventional method. The high signal-to-noise ratio allows us to obtain stellar angular diameters with accuracy better than 2% for $m_V < 5$ and $\phi > 1$ mas as well as more accurate photometry in close double systems.

Approved______________________________ Date__________

THE APPLICATION OF THE TDI METHOD

TO OBSERVATIONS OF LUNAR OCCULTATIONS

By

Laszlo Sturmann

Dissertation

Submitted to the Faculty of the

Graduate School of Vanderbilt University

in partial fulfillment of the requirements

for the degree of

DOCTOR OF PHILOSOPHY

in

PHYSICS

December 2001

Nashville, Tennessee

Approved:	Date:

This dissertation is dedicated to my family.

ACKNOWLEDGMENT

The author wishes to express his great appreciation to Professor David A. Weintraub for his guidance and support throughout this work and for his thorough review of the manuscript. I also thank Prof. Douglas S. Hall and Prof. Arnold M. Heiser for their advice and encouragement. I wish to express very special appreciation to Prof. Laszlo Baksay and Prof. Steven E. Csorna for their invaluable guidance in my academic career.

I am in debt to my colleagues at Konkoly Observatory, especially to Dr. Bela Szeidl and Dr. Lajos G. Balazs, for their teaching early in my carrier and for their support during my tenure at Vanderbilt University. Special thanks to Mr. Geza Viraghalmy who introduced me to astronomical instrumentation and lunar occultations.

I would like to express my gratitude to Profs. Janos Sztipanovits, Gabor Karsai, Csaba Biegl and Dr. Akos Ledeczi in the Measurement and Computing Systems Laboratory at Vanderbilt University for many helpful suggestion and discussions about computer programming.

The author wishes to acknowledge the support of the staff of Dyer Observatory, Mrs. Betty Thurston and Mr. Andre M. Hedrick.

Gratitude should also be extended by the author to the Vanderbilt Dissertation Enhancement Grant for financial support.

Finally and most importantly, I would like to express my deepest thanks to my beloved wife Judit for her constant encouragement and untiring assistance throughout these years. This Ph.D. dissertation is a special gift for my dear parents, whose love and support made this possible.

TABLE OF CONTENTS

LIST OF FIGURES

CHAPTER I

INTRODUCTION

The phenomenon, when celestial objects disappear behind the eastern limb of the Moon and reappear at the western limb some time later, is referred as a lunar occultation (LO) event. It occurs when the shadow cast by the Moon on the ground passes over the observer. Because the "edge" of the shadow is not sharp, objects disappear or reappear quickly but not instantaneously. There is a short ($\sim$ 0.1 s) transition time. Herschel, in 1850, noted that close binaries could be discovered by lunar occultations (see Warner 1988). MacMahon (1908) suggested that the time scale of an occultation event could be used to measure the angular sizes of bright stars. However, Eddington (1909) pointed out that the lunar occultation process is a diffraction phenomenon which would prevent the detection of small angular diameters. He concluded that all stars would show spurious occultation diameters of $0''.008$. In 1939, Williams (1939) showed that the character of the oscillation for light from an extended source is not the same as for a point source and it depends, in a predictable manner, on the diameter of the source.

When a telescope is pointed toward an occulted star a diffraction pattern passes over the telescope aperture. Since the diffraction is due to the distant lunar limb and diffraction effects due to the telescope itself play no role, extremely high angular resolution is achievable. The telescope is used merely to sample the irradiance in the passing diffraction pattern. The necessary time resolution is in the order of 1 ms.

The advent of fast photoelectric recording in the 1930s made the LO technique practicable (Whitford 1939). Whitford observed the occultations of β Capricorni and ν Aquarii at Mt. Wilson on 1938 September 6 and 7, respectively. The stars were not large enough to be resolvable. He concluded that the resolution limit was about $0''.005$. His observations also confirmed that the Moon has no appreciable atmosphere; in addition, by comparing the predicted and observed speed of the fringes past the telescope, he could calculate the slope of the lunar surface where the occultations occurred. He also pointed out that, although it might be anticipated that the assumption of a straight lunar limb would turn out to be too optimistic, the observations of the two stars did not show any contradiction to this hypothesis.

A complete set of measurements was carried out by Evans, Heydenrych and van Wyk (1953) and by Cousins & Gulke (1953) on the supergiant Antares on 1950 May 4, 1951 July 15, 1952 April 13, and 1953 March 8. Evans *et al.* concluded that six observations of Antares gave a mean result of $0''.041 \pm 0''.001$ for the angular diameter of the star. The consistency of the six measurements was important because it indicated that the roughness of the Moon along the tens of meters of lunar limb actually involved in an occultation does not necessarily lead to spurious results. The real problem was why the roughness of the lunar limb has so little effect on occultation light curves. Diercks & Hunger (1952) and latter Evans (1955, 1970, 1971) and Morbey (1972) discussed the problem. Nevertheless, during the period 1955 – 68, there was a wide spread uncertainty as to the value of stellar diameters obtained from lunar occultations.

In the 1960's there was a growing interest in radio occultations. Observing lunar occultations of radio sources yields far more accurate positions and diameters of these small sources than does any other method. This was first suggested by Hetmanzev

& Ginzburg (1950) and led to positional accuracies of $3''$ for the source 3C 212, and $0''.7$ for 3C 273. These positions were absolutely necessary for the identification of their optical counterparts. Hoyle (1958) and Hoerner (1961) emphasized the need for statistical investigations of the small diameters of cosmologically important objects. Scheuer (1962) suggested restoring the brightness profile across the source by convolving a restoring function with the observed diffraction pattern. Taylor (1966) reanalyzed the earlier observations of Antares by using Scheuer's method and confirmed the earlier results. More recently (Richichi & Lisi 1990) found that Antares has an angular diameter of 41.3 milli arcsec (mas) at $\lambda = 2.43\ \mu$m and that the profile is slightly asymmetric.

Until 1968, lunar occultations were carried out with measurements of currents and chart recorder displays. With the rapid development of digital electronics, new equipment was developed, including the pulse-counting photometer and the multichannel scaler. The first lunar occultation observation with these new tools was made at McDonald Observatory on 1968 December 29 by Nather & Evans. The Texas group produced a series of papers describing the occultation process (Nather & Evans 1970), the technique of digital recording (Nather 1970), data reduction (Nather & McCants 1970), the discovery of binary systems (Evans 1971), and limb effects (Evans 1970). The success of the Texas group, which demonstrated a new and rewarding use of small telescopes, inspired many other institutions to start lunar occultation programs. Parallel with the observations many attempts have been made to extract the most reliable astrophysical information from occultation traces. However most reduction has been carried out in the manner suggested by Nather & McCants (1970), i.e., by generating theoretical light curves and fitting them to the observed data by the method of least squares.

For several decades, the power of the LO technique has been brought to bear on a broad range of astrophysical problems, including investigations of the presence of a lunar atmosphere, studies of lunar motion, astrometry of radio and X-ray sources, measuring stellar angular diameters and effective temperatures of cool giant stars (Ridgway *et al.* 1980), binaries on the main sequence and among T Tauri stars, and the circumstellar environment of red giants and carbon stars. (See Warner 1988, IAU Col. #62, Evans 1985, McAlister 1985, Richichi 1994).

In 1981, White (White 1981) suggested the use of the developing Charge Coupled Device (CCD) array to record both spectrally and temporally resolved occultations. The first LO observation with a CCD was done by Schmidtke (1986) who successfully applied this technique to the occultation of Antares. In 1987, Gies obtained a series of low-resolution spectra with a sampling rate of 7 ms of the H_α emission line of the Be star Pleione with a special CCD setup during a lunar occultation (Gies 1990). The center of light of the emission envelope was occulted 5.5 ± 1.1 ms before the continuum light of the star itself, which suggested that there is a geometric asymmetry in the envelope. Stecklum (1987) published the first diagram of a CCD occultation spectrophotometer. This instrument would make it possible to obtain high-resolution observations of the diffraction pattern simultaneously at different wavelengths but it required a very high data read-out rate that made it very difficult to implement. In 1994, Sturmann (Sturmann 1994) proposed applying the Time Delay and Integrating (TDI) method to LO studies.

Despite the power of the LO technique, there are inherent limitations. LOs are fixed time events and only objects that happen to lie within approximately $\pm 6°$

of the ecliptic are occulted. This swath of the sky represents about 10% of the celestial sphere. Also a single LO gives only a one-dimensional (1-D) scan across the object and is insensitive to the intensity distribution measured parallel to the lunar limb. In some cases, 1-D information is adequate, e.g., for measurements of stellar diameters or circumstellar shells. In other cases, we can construct two-dimensional (2-D) images from a combination of several LO observations taken at different contact angles (Simon *et al.* 1990).

The LO technique also provides several advantages that more than satisfactorily counterbalance its limitations: small 1-2 m telescopes are adequate for lunar occultation work and this means easy access for an observer; the instrumentation and data reduction are relatively simple; occultations are rather insensitive to seeing and do not require much telescope time.

This dissertation is about an alternative technique for making LO observations. This new method requires a CCD detector and utilizes a novel charge transfer scheme (TDI) for tracking the diffraction pattern of an occulted star. In this dissertation we demonstrate that the TDI method is superior in every sense to the conventional method and worth trying.

In the next chapter we discuss to some extent the main astrophysical motivations for making LO observations. In Chapter III we summarize the straight-edge model of LO light curves and present formulae to compute the diffraction pattern of an arbitrary object in the presence of limb irregularities. In Chapter IV we critique the traditional method of LO observations and address the inherent limitations of the conventional method. We introduce the TDI method in Chapter V and discuss it in great detail by presenting a mathematical model as well as results of computer simulations. In Chapter VI we discuss an algorithm for simulating TDI LO observations. We include a tractable scintillation noise model in our computations. In Chapter VII we compare the two methods from the point of view of the achievable signal-to-noise ratio (SNR). In Chapter VIII we present results from the computer simulations described in Chapter VI. In Chapter IX we present three bench-top experiments for building a LO occultation simulator, in order to measure sensitivity variations along individual pixels of a CCD detector and to evaluate the performance of an HPC-1 CCD camera available at the Dyer Observatory. We summarize our research efforts in Chapter X.

CHAPTER II

MOTIVATION

2.1 Angular Diameters and Effective Temperatures

The determination of stellar angular diameters is of fundamental importance in astrophysics, since it represents the only direct method of measuring the radius and effective temperature of a star. The angular radius can be converted into a reliable radius only if limb darkening and accurate parallax are available[1]. The effective temperature is directly related to the bolometric flux f and angular diameter ϕ according to the definition

$$f = \left(\frac{\phi}{2}\right)^2 \sigma T_e^4 \tag{2.1}$$

and is therefore a valuable check for atmospheric models and for indirect measurement methods. However, the overall accuracy of angular diameters determined by LOs is rarely better than 10-15%. An error of 15% in the diameter leads to an error of about 7% in the temperature. Errors of this magnitude –a few hundred K– are unacceptably large for most theoretical work. Therefore, it is desirable to improve the accuracy of angular diameter measurements.

For spectral types later than K5, the relation between spectrum and T_e was determined for the first time by an analysis based exclusively on LO results (Ridgway *et al.* 1980). More recently, accurate determinations of angular diameters have been obtained by interferometry (Di Benedetto & Rabia 1987, Mozurkewich *et al.* 1990) with comparable accuracy. LOs still represent the only means to reach spectral types

[1]The parallaxes of stars measured by the Hipparcos satellite with an accuracy of 1-2 mas is available.

later than M5, which are not well calibrated yet and for which no stars are bright enough to be measured by other techniques.

2.2 Binary and Multiple Stars

Probably, the most important contribution of LOs to binary star studies is the discovery of tight systems which can then be followed up where possible by other methods. An example of this is represented by the surveys of multiplicity at the early stages of star-formation, conducted by means of LOs, speckle interferometry, and direct imaging in the Taurus and Ophiuchus regions (Leinert *et al.* 1991, Simon 1992). Recently Mason (1994) assembled a catalog of all observed occultation binaries.

According to Richichi & Lisi (1993) a SNR $\simeq 10$ is necessary to resolve binaries with $\Delta m \leq 1.5$ and with separations ≥ 5 mas. A factor of 10 increase in the SNR could improve the detectability limit to $\Delta \mathrm{m} \leq 4$ at separations ≥ 5 mas, thereby decreasing the importance of selection effects in binary frequency studies. Higher SNRs could also improve the accuracy of differential photometry of the components in a close system that is currently not better than about $0^m.2 - 0^m.3$. Also it may be possible to study directly the shape distortion of the components and inhomogeneities in surface brightnesses.

The improved sensitivity makes possible the search for low-mass companions of stars in the solar neighborhood. Within 25 pc from the Sun, there are about 400 stars that can be occulted by the Moon.

2.3 Calibrating and Cross Checking the Interferometers

The angular resolution of LO observations is comparable with that (~ 0.2 mas) of the upcoming generation of Michelson interferometers like the CHARA Array *(http://www.chara.gsu.edu)*. No other method is currently available at this very high angular resolution for calibrating and cross checking the interferometers. Therefore accurate angular diameters obtained from LO observations will be very valuable.

CHAPTER III

MATHEMATICAL MODELLING OF LO LIGHT CURVES

In this chapter we show how the Kirchhoff-Fresnel theory leads to the straight-edge model which is often used in LO simulations and for data reductions. We also present an algorithm to compute the diffraction pattern of extended objects occulted by an arbitrary irregular limb.

The Moon is a very intricate obstacle in the way of light coming from an occulted object during a lunar occultation event. Light emanating from points of the object is diffracted by the lunar limb, resulting in an irradiance pattern that can be observed on the surface of the Earth.

In order for the LO method to be useful, we should be able to compute the diffraction pattern due to the occultation of sources with realistic brightness distributions by solving the scalar wave equation with boundary conditions written for the Moon. Such a general solution is impossible, in the sense that overwhelmingly difficult numerical calculations would be needed even if we had detailed knowledge about the Moon at the occultation position. Thus, we have to make approximations.

Eddington (1909) and Nather & Evans (1970) showed that it is possible to approximate the structure of the diffraction patterns of stars as Fresnel diffraction at a straight edge. Occasional departures of the observed light curve from this diffraction pattern may be explained (Evans 1970) by irregularities in the shape of the limb. It is usually assumed that the lunar limb is an infinitely thin two dimensional object, i.e., it does not have surface structure along the line of sight. Murdin (1971) estimated the effects of the three-dimensional (3-D) Moon on light curves and showed that it represents a timing error of the order of microseconds, and modifies the amplitudes of the fringes by a factor of 10^{-4}, which is too small to be detectable. Therefore, the lunar limb is safely regarded as a two dimensional aperture.

Diffraction of scalar waves on apertures can be described by the Kirchhoff diffraction theory that puts the Huygens-Fresnel theory on a sounder mathematical basis. The basic idea of the Huygens-Fresnel theory is that the light disturbance at a point P_o arises from the superposition of secondary waves that proceed from a surface situated between the point and the light source. Kirchhoff showed that the Huygens-Fresnel principle may be regarded as an approximate form of a certain integral theorem which expresses the solution of the homogeneous wave equation, at an arbitrary point in the field, in terms of the values of the solution and its first derivatives at all points on an arbitrary closed surface surrounding P_o (see Born & Wolf, 1975). The Kirchhoff theory applies strictly to scalar (longitudinal) waves, such as acoustic waves. However, it also turns out to be generally effective for vector (transverse) waves, except for features directly associated with polarization.

The distance to any occulted object is so large that we can assume that the thin lunar limb is illuminated by plane waves. In this case, the Kirchhoff-Fresnel diffraction formula has the form of

$$U(P_o) = -\frac{iA}{2\lambda} \iint\limits_{\mathcal{A}} \frac{e^{iks}}{s} \left[1 - \cos(\mathbf{n}, \mathbf{s})\right] dS, \tag{3.1}$$

where $U(P_o)$ and A are the complex amplitudes in P_o and at the aperture plane $\mathcal{A}$, λ is the wavelength, $\mathbf{n}$ is the surface normal vector, $\mathbf{s} \equiv \overrightarrow{P_oQ}$, and dS is an elementary area at Q (see Fig. 3.1).

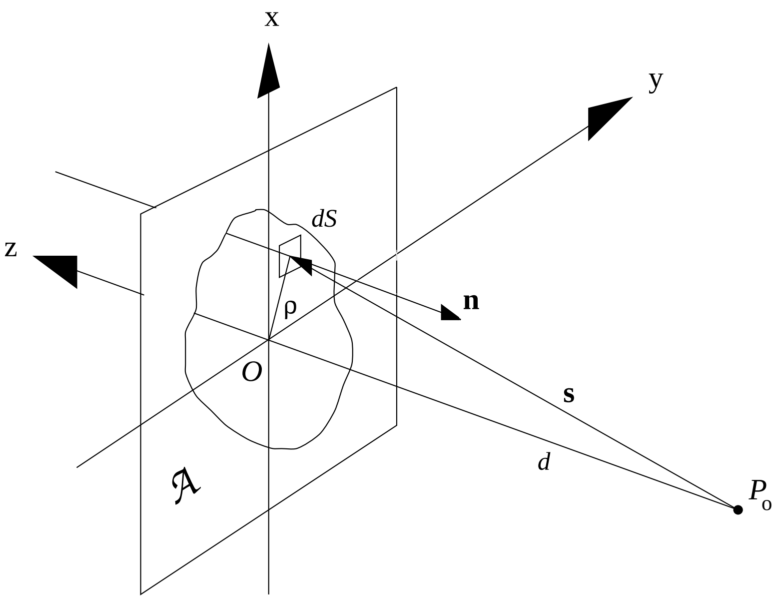

Figure 3.1: Illustration for the Kirchhoff-Fresnel diffraction formula.

Considerable simplifications of (3.1) can be made by noticing that the path length difference varies as

$$ds = \frac{\rho d\rho}{d} \tag{3.2}$$

with ρ. Solving

$$ds = n\frac{\lambda}{2} \tag{3.3}$$

for n yields

$$n = \frac{\rho}{\left(\frac{\lambda d}{2}\right)} d\rho,$$

which means that the elementary contributions from points far ($\rho >> \lambda d/2$) from the line of sight of the source effectively cancel one another because with increasing n the phases of the elementary contributions are distributed almost uniformly in the interval $[0, 2\pi]$.

Additionally, the observed radiation is never monochromatic; therefore, the coherence length of light, $l_c \simeq \bar{\lambda}^2/\Delta\lambda$, is very short, on the order of $\sim 10^{-5}$ m under common observational circumstances ($\bar{\lambda} \simeq 600$ nm, $\Delta\lambda \simeq 30$ nm, for instance). Wavelets from points for which the path length difference is larger than l_c do not contribute to the observed interference pattern appreciably because their phase is uncorrelated and they cancel one another. Consequently, the angle of diffraction is very small, on the order of $0''.05$. For example, at wavelength $\bar{\lambda} = 600$ nm, the distance r from the point where a point source disappears behind the limb to a point where the path-length difference $\rho^2/2d$ is equal to l_c is

$$\begin{array}{ll} \Delta\lambda[\text{nm}] & \rho[\text{m}] \\ 1 & 525 \\ 10 & 166 \\ 100 & 52 \end{array} \tag{3.4}$$

Here $d = 3.84 \times 10^8$ m is the distance to the Moon. Therefore, we can apply the paraxial approximation and substitute $1 - \cos(n, s) \simeq 2$ and $1/s \simeq 1/d$. Then (3.1) can be written as

$$U(P_o) = -\frac{iA}{\lambda d} \iint_{\mathcal{A}} e^{iks} dS. \tag{3.5}$$

3.1 The Straight-Edge Model

On the short distance that matters, the curvature of the lunar limb is completely negligible and the lunar limb is often regarded as an **infinite straight-edge**.

In the paraxial approximation we can expand s as

$$s = \sqrt{d^2 + x^2 + y^2} \simeq d + \frac{x^2}{2d} + \frac{y^2}{2d}, \tag{3.6}$$

where y is the distance of the straight edge from the line of sight. After dropping the overall phase factor e^{ikd}, which does not affect the irradiance on the ground, we obtain the Fresnel diffraction formula

$$U(P_o) = -\frac{iA}{\lambda d} \iint\limits_{\mathcal{A}} e^{ik\frac{(x^2+y^2)}{2d}} dS. \tag{3.7}$$

The straight-edge model approximation reduces the problem to a 1-D integral since only the direction perpendicular to the limb matters. To evaluate (3.7) for a half plane $\mathcal{A}$ we integrate over x and substitute t for y

$$y = t\sqrt{\frac{\lambda d}{2}}, \tag{3.8}$$

which leads to

$$U(P_o) = -\frac{(1+i)A}{2} \int_{-\infty}^{y\sqrt{\frac{2}{\lambda d}}} e^{i\frac{\pi}{2}t^2} dt. \tag{3.9}$$

The integral (3.9) can be evaluated in terms of Fresnel integrals by separating the real and imaginary parts

$$U(P_o) = -\frac{(1+i)A}{2} \left\{ \left[\frac{1}{2} + \mathcal{C}\left(y\sqrt{\frac{2}{\lambda d}} \right) \right] + i \left[\frac{1}{2} + \mathcal{S}\left(y\sqrt{\frac{2}{\lambda d}} \right) \right] \right\}, \tag{3.10}$$

where

$$\mathcal{C}(x) = \int_0^x \cos\left(\frac{\pi}{2}t^2\right) dt, \quad \mathcal{S}(x) = \int_0^x \sin\left(\frac{\pi}{2}t^2\right) dt$$

are the Fresnel integrals. The 1-D monochromatic irradiance distribution due to a point source is obtained from

$$I_\lambda(y) = UU^* = \frac{I_0}{2} \left\{ \left[\frac{1}{2} + \mathcal{C}\left(y\sqrt{\frac{2}{\lambda d}} \right) \right]^2 + \left[\frac{1}{2} + \mathcal{S}\left(y\sqrt{\frac{2}{\lambda d}} \right) \right]^2 \right\}, \tag{3.11}$$

where $I_0 = A^2$ is the irradiance in the absence of the half plane. The variation of irradiance in equation (3.11) may be illustrated by means of a geometrical representation due to Cornu (Fig. 3.2). $\mathcal{C}$ and $\mathcal{S}$ are regarded as rectangular coordinates of a point B. The irradiance at a point y is proportional to the length of vector $\mathbf{R}$.

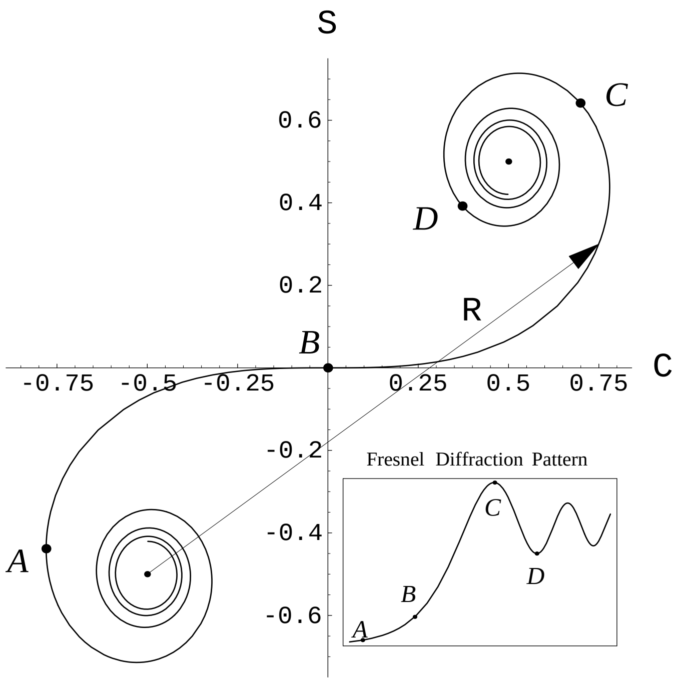

Figure 3.2: Representation of Fresnel diffraction of a monochromatic pointsource on a straight-edge by Cornu spiral. The irradiance at a point in the diffraction pattern is proportional to the length of vector **R**.

Equation 3.11 is the basic equation for modeling LO light curves. The polychromatic diffraction pattern of a point source can be obtained by integrating Eq. 3.11 over a wavelength band (see Section 6.1). Since most astrophysical objects radiate incoherently, the diffraction pattern due to an extended object can be computed by weighting and combining the diffraction patterns due to individual points of the object, where the weighting is done according to the brightnesses of the individual points. We return to the problem of modeling extended polychromatic objects in Section 6.1.

3.2 Limb Effects

It has been recognized for many years that irregularities on the lunar limb can produce significant distortions in light curves of stars that are occulted near these irregularities. Jackson (1950) suggested that the question as to whether distortion ought to be attributed to the lunar limb or intrinsic properties of the star might be resolved by making two observations from different sites, separated by as little as a couple of hundred meters. Diercks & Hunger (1952) investigated the effects produced by elevations and depressions on the lunar limb and concluded that the distortion of occultation light curves could mimic those due to a sensible stellar diameter. Evans (1955, 1970) discussed this problem in detail and argued that "the whole problem may turn out to be of rather minor importance in the interpretation of occultation traces." Evans also proposed making simultaneous observations at the same place in two different colors because the effect of limb irregularities is wavelength dependent.

Limb irregularities can be divided into two groups by the character of their influence on the occultation curve: discrepancy in the inclination of the edge with respect to the computed value and departures of the shape of the limb from a straight edge. The first group of irregularities do not distort the shape of the occultation curve, but they alter the time scale of the occultation curve. The second qroup is capable of causing considerable distortions of an occultation curve, but the probability of their occurence is apparently low [1].

Narrow band TDI LO observations on large telescopes would provide higher signal-to-noise ratios in LO data sets than conventional observations. Narrow bandwidths

[1] Conventional LO observations and the Apollo missions have shown that the surface of the Moon is rather smooth. Steep ($> 30°$) slopes and narrow canyons appear to be rare.

would result in longer coherence lengths of light. Thus, with TDI, a larger part of the limb will contribute to the production of the diffraction pattern. Therefore, we anticipate more noticeable limb effects due to the first group of irregularities on TDI light curves than on conventional LO light curves.

In the following section we investigate how irregularities on the lunar limb can be taken into account in LO model computations. We present a method that can be used to compute LO light curves for arbitrary limb features[2], i.e., the validity of the **straight-edge** model is not assumed.

3.2.1 Diffraction Pattern of a Point Source at an Irregular Limb

Diffraction effects due to irregularities on the lunar limb can be computed using the concept of circular Fresnel zones. We wish to investigate the wave amplitude observed in a wavenumber band $k_o \pm \Delta k$ reaching the observation point P_o from an infinitely distant point source in the presence of a half-plane with an **irregular edge**.

By giving up the straight-edge model the diffraction on the lunar limb no longer can be treated as a 1-D problem; the paraxial approximation, however, is still valid.

To apply the Fresnel diffraction formula (Eq. 3.7), we consider the contribution to the wave at P_o that passes through the infinitesimally thin annular strip at Q, of radius ρ, width $d\rho$, and area $dS = \rho d\rho d\vartheta$ (Fig. 3.3). Assuming that $A \equiv 1$, the net amplitude at P_0 is

$$U(y,k) = -\frac{i}{2\pi d} k \int_0^\infty \int_{\vartheta_1}^{\vartheta_2} e^{ik\frac{\rho^2}{2d}} \rho d\vartheta d\rho. \tag{3.12}$$

We write the angular integral in form of $2\pi\vartheta(\rho, y)$, where $\vartheta(\rho, y)$ represents the visible fraction of the annular strip of radius ρ at a given y. The irregularities along

[2]The lunar limb is still treated as a thin 2-D screen.

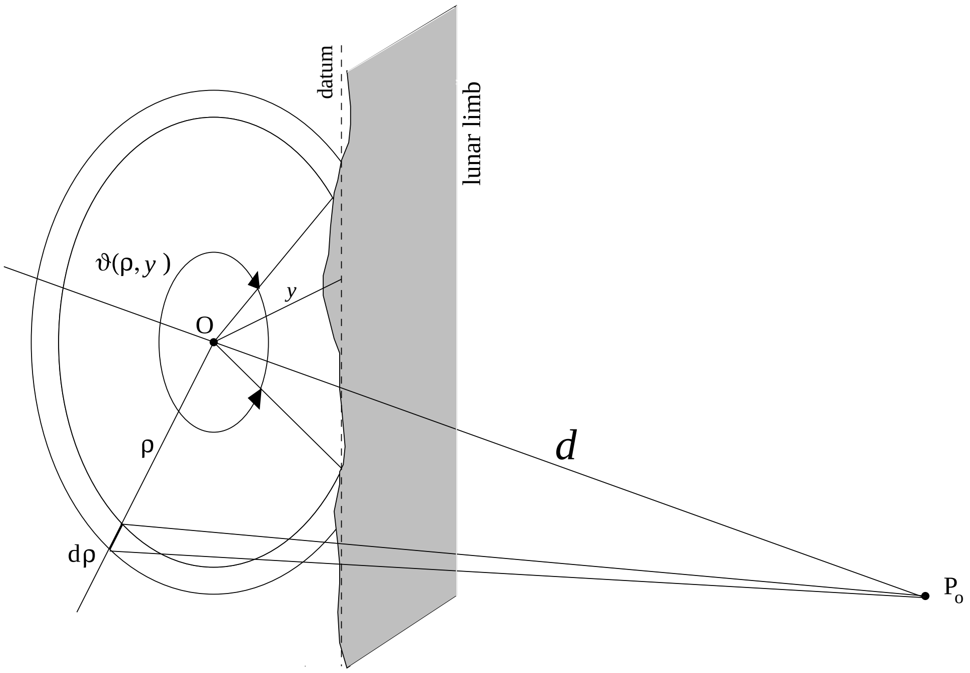

Figure 3.3: The complex amplitude at P_o is expressed in polar coordinates. The limb structure is implicit in the angular integral that is written as $2\pi\vartheta(\rho, y)$, where $\vartheta(\rho, y)$ represents the visible fraction of the annular strip of radius ρ at a given y.

the limb are implicit in $\vartheta(\rho, y)$.

Every observation has finite optical bandwidth. As the optical path-difference is increasing, with increasing ρ, the visibility of the fringes decreases and eventually disappears when the path length difference is larger than the coherence length l_c. We can account for this disappearance of the fringes by noticing that each monochromatic component of the incident wave front produces a diffraction pattern, and as the path difference is increased from zero, these component patterns show increasing mutual displacement because of the difference in wavelength. The visibility of the fringes therefore decreases, and they disappear altogether when the optical path difference is sufficiently large.

Let us assume a Gaussian band $g(k)$ such that

$$g(k) = \frac{\beta}{\sqrt{\pi}} e^{-\beta^2(k-k_o)^2}, \tag{3.13}$$

where $\beta = 2\ln 2/\Delta k$ and Δk is the full-width-at-half-maximum (FWHM). The band $g(k)$ is normalized such that

$$\int_{-\infty}^{+\infty} g(k)dk = 1. \tag{3.14}$$

Integrating (Eq. 3.12) over the optical band $g(k)$ gives the polychromatic complex amplitude at P_o

$$U(y) = -i\frac{\beta}{d\sqrt{\pi}}\int_0^{\infty} \rho\vartheta(\rho, y)\int_{-\infty}^{+\infty} ke^{-\beta^2(k-k_o)^2} e^{ik\frac{\rho^2}{2d}} dk\, d\rho. \tag{3.15}$$

The k integral can be evaluated and yields

$$e^{ik_o\frac{\rho^2}{2d}} e^{-\frac{\rho^4}{16d^2\beta^2}} \int_{-\infty}^{+\infty} e^{-\beta^2\left(k-\left(k_o+\frac{i\rho^2}{4\beta^2 d}\right)\right)^2} dk = e^{ik_o\frac{\rho^2}{2d}} e^{-\frac{\rho^4}{16d^2\beta^2}} \left(k_o + \frac{i\rho^2}{4\beta^2 d}\right)\frac{\sqrt{\pi}}{\beta}. \tag{3.16}$$

Substituting (Eq. 3.16) into (Eq. 3.15) gives the formula

$$U(y) = -\frac{i}{d}\int_0^{\infty} \vartheta(\rho, y)\left(k_o + \frac{i\rho^2}{4\beta^2 d}\right) e^{ik_o\frac{\rho^2}{2d}} e^{-\frac{\rho^4}{16\beta^2 d^2}} \rho d\rho. \tag{3.17}$$

The path-difference $\rho^2/2d$ can be conveniently expressed in terms of the number n of half wavelengths by which the path QP_o is longer than OP_o, that is,

$$\frac{\rho^2}{2d} \equiv \frac{\lambda_o}{2}n = \frac{\pi}{k_o}n. \tag{3.18}$$

The coordinate $\rho = \sqrt{n\lambda_o d}$ is thereby replaced by $0 \leq n < \infty$, a continuous variable. In particular, the aperture area between circles of radii $\rho(n-1)$ and $\rho(n)$ with n integral is known as the n^{th} **Fresnel zone.** We introduce another variable m, similar to n, such that

$$\text{sgn}(y)\frac{y^2}{2d} \equiv \frac{\lambda_o}{2}m = \frac{\pi}{k_o}m, \tag{3.19}$$

where y is the distance of the line of sight of the point source from the limb measured in a direction parallel to the motion of the limb and

$$\mathrm{sgn}(y) \equiv \begin{cases} +1, & y > 0 \\ 0, & y = 0 \\ -1, & y < 0 \end{cases} \cdot \tag{3.20}$$

$m = 0$ at the moment when the point is occulted and $m > 0$ before and $m < 0$ after the occultation.

Substituting (Eq. 3.18) into (Eq. 3.17) yields

$$U(m) = -i\pi \int_0^\infty \vartheta(n, m) \left(1 + \frac{in\pi}{8\log^2 2}\left(\frac{\Delta k}{k_o}\right)^2\right) e^{in\pi} e^{-\frac{\pi^2 n^2}{16\log^2 2}\left(\frac{\Delta k}{k_o}\right)^2} dn. \tag{3.21}$$

Let us introduce

$$\alpha \equiv \frac{\pi}{4\log 2}\frac{\Delta k}{k_o}, \tag{3.22}$$

whereupon

$$U(m) = -\int_0^\infty \vartheta(n, m)\left(i\pi - 2\alpha^2 n\right) e^{in\pi} e^{-\alpha^2 n^2} dn. \tag{3.23}$$

Note that

$$\left(i\pi - 2\alpha^2 n\right) e^{in\pi} e^{-\alpha^2 n^2} = \frac{d}{dn}\left(e^{in\pi} e^{-\alpha^2 n^2}\right) \tag{3.24}$$

and integrating (Eq. 3.23) by parts yields

$$U(m) = -\left[\vartheta(n, m) e^{in\pi} e^{-\alpha^2 n^2}\right]_0^\infty + \int_{n_0(m)+0}^\infty e^{in\pi} e^{-\alpha^2 n^2} \frac{\partial \vartheta(n, m)}{\partial n} dn, \tag{3.25}$$

where $n_0(m)$ is that particular n when the annular strip touches the limb for the first time. For $n < n_0(m)$, $\partial\vartheta(n, m)/\partial n = 0$ and $\partial\vartheta(n, m)/\partial n$ do not exist at $n = n_0(m)$. Since $0 \le \vartheta(n, m) \le 2\pi$, the upper limit of the first term is zero and then the first term is equal to

$$\lim_{n\to 0} \vartheta(n, m) = \frac{1 + \mathrm{sign}(m)}{2}. \tag{3.26}$$

Therefore,

$$U(m) = \frac{1+\operatorname{sgn}(m)}{2} + \int_{n_0(m)+0}^{\infty} e^{in\pi} e^{-\alpha^2 n^2} \frac{\partial \vartheta(n,m)}{\partial n} dn. \tag{3.27}$$

We have two expressions for the complex amplitude U at P_o: (Eq. 3.23) and (Eq. 3.27). By separating the real and imaginary parts in (Eq. 3.23) we obtain

$$\operatorname{Re} U(m) = \int_0^{\infty} \left(2\alpha^2 n \cos \pi n + \pi \sin \pi n\right) e^{-\alpha^2 n^2} \vartheta(n,m) dn, \tag{3.28}$$

$$\operatorname{Im} U(m) = \int_0^{\infty} (2\alpha^2 n \sin \pi n - \pi \cos \pi n) e^{-\alpha^2 n^2} \vartheta(n,m) dn \tag{3.29}$$

and similarly from (Eq. 3.27)

$$\operatorname{Re} U(m) = \frac{1+\operatorname{sgn}(m)}{2} + \int_{n_0(m)+0}^{\infty} e^{-\alpha^2 n^2} \frac{\partial \vartheta(n,m)}{\partial n} \cos \pi n \, dn, \tag{3.30}$$

$$\operatorname{Im} U(m) = \int_{n_0(m)+0}^{\infty} e^{-\alpha^2 n^2} \frac{\partial \vartheta(n,m)}{\partial n} \sin \pi n \, dn. \tag{3.31}$$

The information about the lunar limb is in the factor $\vartheta(n,m)$. $\operatorname{Re} U$ and $\operatorname{Im} U$ can be evaluated numerically for any $\vartheta(n,m)$ and the irradiance distribution due to point source observed at P_o is given by UU^* [3] (see Fig. 3.4 and 3.5).

For a straight-edge lunar limb

$$\vartheta(n,m) = \begin{cases} 1, n \leq m \\ 1 - \frac{1}{\pi} \arccos \frac{m}{n}, n > |m| \\ 0, n \leq -m \end{cases} \tag{3.32}$$

and

$$\frac{\partial}{\partial n} \vartheta(n,m) = \begin{cases} 0, n \leq |m| \\ -\frac{1}{\pi} \frac{m}{n\sqrt{n^2 - m^2}}, n > |m| \end{cases}. \tag{3.33}$$

[3] Ideally, we should have included the explicit time dependence e^{-ikct} in (3.15) since this factor is dependent of k. Then the resultant polychromatic irradiance distribution would be time dependent too. However, it turns out that (see Appendic C), as long as the integration time τ associated with data points is much longer than the coherence time $\tau_c = l_c/c$ of light, the averages of the time varying terms over τ are practically zero, i.e., it does not matter whether the monochromatic intensity is computed first and integrated over a k band to obtain the polychromatic intensity or the time varying amplitude is integrated over a k band first and the intensity is computed after. As long as $\tau \gg \tau_c$,the result will be the same. Here we selected the latter for computational reasons.

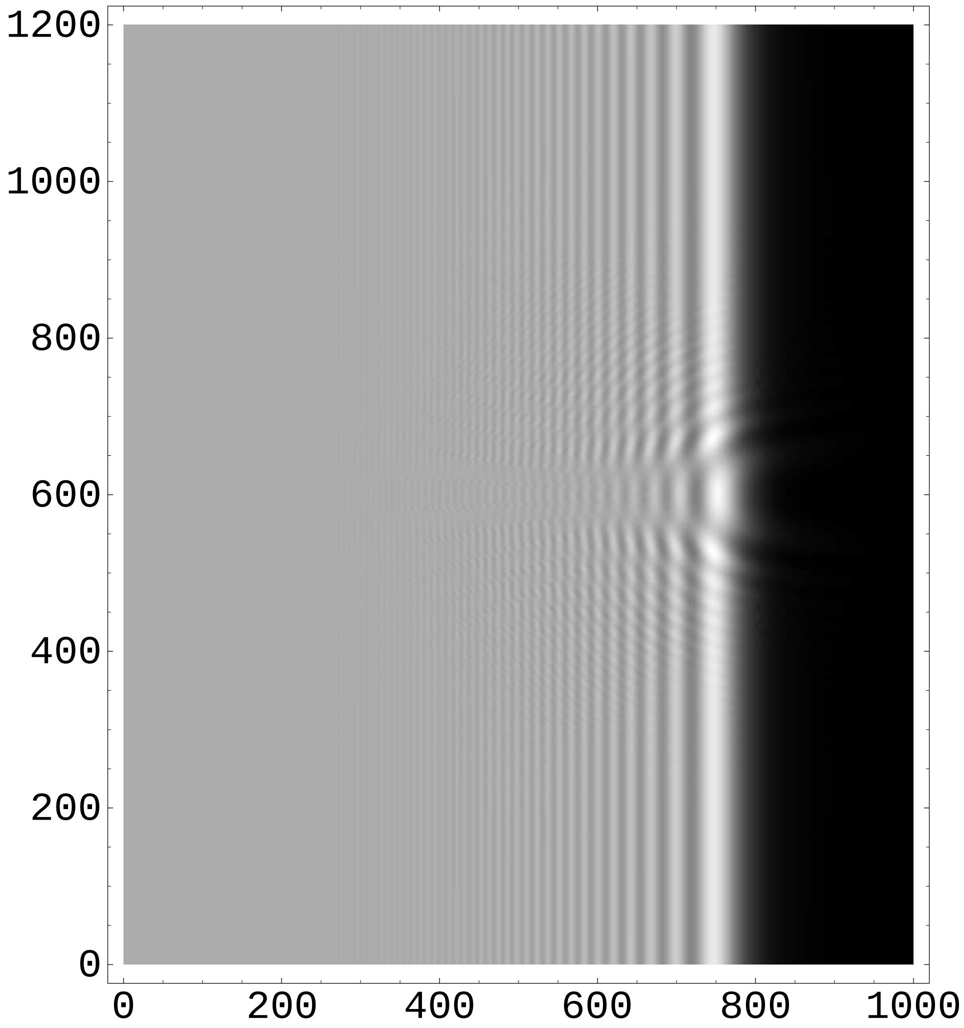

Figure 3.4: The 2-D diffraction pattern of a point source at $\lambda = 600$ nm and $\Delta\lambda = 10$ nm. The occultation occured close to a 10 m wide 5 m deep symmetrical feature on the lunar limb. The scale of the image is 0.25 m/point.

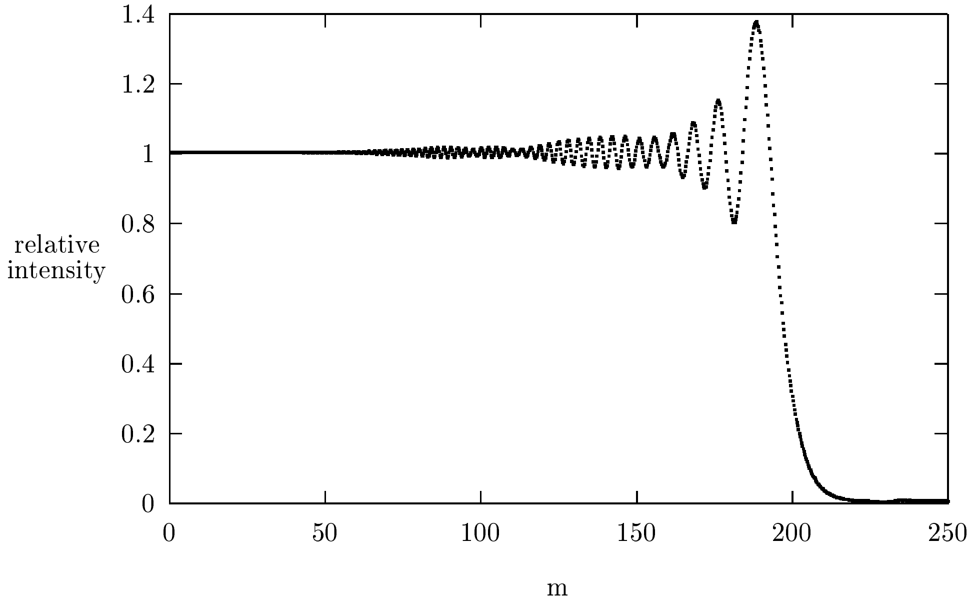

Figure 3.5: The cross section of the 2-D diffraction pattern at 5 m apart from the deepest point of the limb feature. The diffraction pattern resembles to the diffraction pattern of a close binary system occulted by a straight edge. Limb features could result in mistaken identification of binary systems.

Substituting (Eq. 3.33) into (Eq. 3.30) yields

$$\mathrm{Re}\, U(m) = \frac{1+\mathrm{sgn}(m)}{2} - \frac{m}{\pi}\int_{|m|}^{\infty} \frac{e^{-\alpha^2 n^2}\cos \pi n}{n\sqrt{n^2-m^2}}\, dn, \tag{3.34}$$

$$\mathrm{Im}\, U(m) = -\frac{m}{\pi}\int_{|m|}^{\infty} \frac{e^{-\alpha^2 n^2}\sin \pi n}{n\sqrt{n^2-m^2}} dn. \tag{3.35}$$

3.2.2 Extended Objects

The diffraction pattern of an extended object can be obtained from the diffraction pattern of point objects because the points of astrophysical objects radiate independently of one another. Therefore, the diffraction patterns due to different points of the object are simply added together. Points along a chord cc' (Fig. 3.6) produce the same pattern but the patterns are shifted in phase and weighted according to their positions and relative brightnesses, respectively.

The simplest way to compute the diffraction pattern of an extended object is to slice the object into a series of stripes parallel to the motion of the limb. Taking one point from each slice along bb', for example, we compute a series of diffraction patterns as these points are occulted by the limb. Then, we convolve these diffraction patterns with the relative irradiance distributions along the corresponding slices. Finally, we add them together. The result is what an observer would measure with a point detector at P_o. For an extended detector, like the aperture of a telescope, we have to compute a 2-D distribution of irradiance by repeating this procedure and then sampling the irradiance distribution by the aperture.

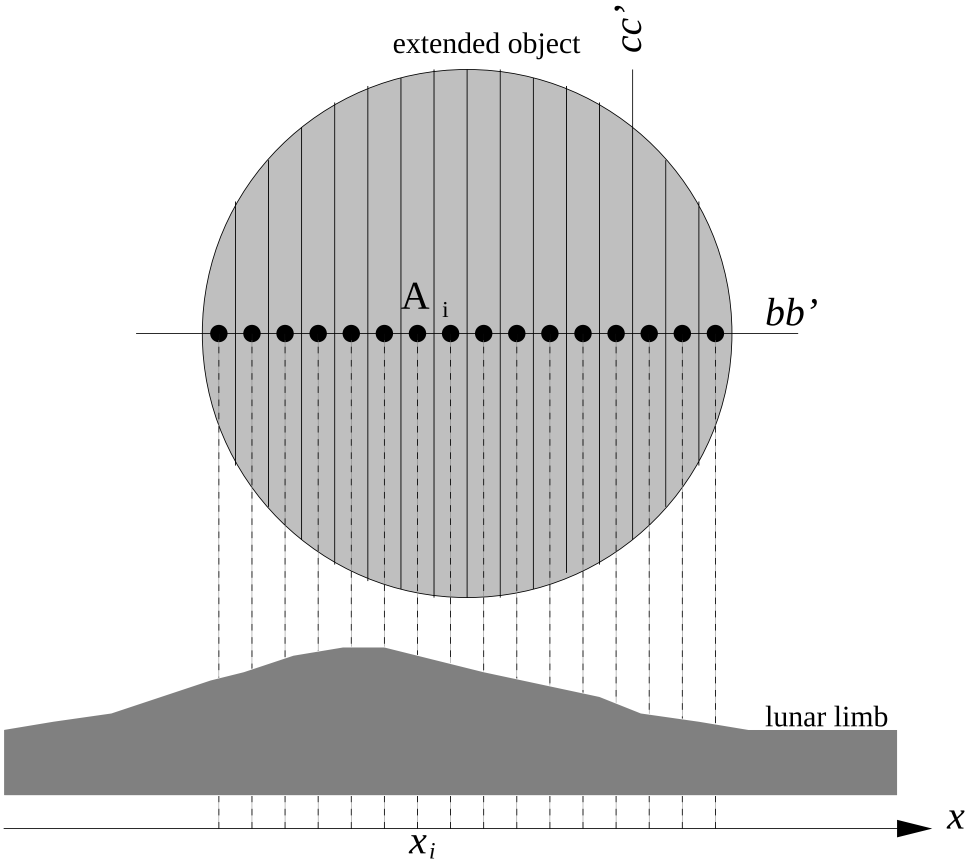

Figure 3.6: The 2-D diffraction pattern of extended incoherently radiating objects can be computed by superposition. The total irradiance produced the diffraction of the light from an extended object is the sum of diffraction patterns due to a large set of point sources. Every point of an object along a stripe perpendicular to the smooth limb produces the same diffraction pattern. The only difference is that these diffraction patterns are shifted in time according to the relative positions of the points. This fact simplifies the computations considerably because we need to compute diffraction patterns only for points along bb'. Then the diffraction pattern for a stripe can be computed as a convolution integral. Finally, the 2-D irradiance distribution in the diffraction pattern of the extended source is the sum of that of the individual stripes.

CHAPTER IV

CRITIQUE OF THE CONVENTIONAL METHOD OF LO OBSERVATIONS

High angular resolution information about an object occulted by the Moon is embedded in the amplitude and shape of the diffraction pattern. When the angular diameter ϕ of the object is small enough, $\phi \lesssim \sqrt{\lambda/d}$, diffraction fringes become evident in the light curve. Here λ is the wavelength of the observation and d is the distance to the Moon[1]. The achievable angular resolution of the LO method is determined by the quality of the recorded light curves. Two things affect the quality of the recorded data:

- a number of instrumental effects, which cause distortion of the light curve, and
- random noise, which is associated with the photon detection process (shot noise) and atmospheric effects (scintillation).

The latter is usually expressed by the SNR of the light curve. Since distortions can be restored as far as the SNR allows during data processing, the determinant factor is the SNR. The possibility of restoration does not mean, however, that minimizing the deterministic distortions is not important.

The conventional lunar occultation observation is known to be a small telescope project. The conventional method applies a high speed photoelectric photometer mounted on a 1-2 m telescope to integrate the passing diffraction pattern in a series of short (1-10 ms) time intervals in the optical or near infrared range of the spectrum.

[1] At $\lambda = 600$ nm, $\sqrt{\lambda/d}$ yields about 8 mas, assuming $d = 3.84 \times 10^8$ m.

This is a fairly simple and inexpensive setup that has comparable resolution to, and higher sensitivity than, the modern Michelson interferometers and a factor of ten higher angular resolution than speckle interferometry.

By the late 1980s, virtually all the available bright stars had been studied in lunar occultation programs. For reasons discussed below, the fainter stars could not be studied at all and no further gains were achievable in studying the bright stars. Thus, the LO method appeared to have been exhausted by the late 1980s. At the same time, with the availability of near-infrared detectors, several groups started infrared LO observation programs (Richichi 1996, Simon 1992)

Although considerable angular resolution can be obtained ($\sim$ 1 mas) for bright ($V < 4$, $K < 4$) stars, the SNR drops rapidly with increasing magnitude and this fact seriously limits the number of resolvable stars[2]. The importance of instrumental factors in limiting the applicability of the conventional LO technique has been discussed by Ridgway (1977) and Richichi (1987).

The most important factors, each of which mitigates against observing faint stars, are:

- the diameter of the telescope aperture. A large aperture improves the SNR, permitting observations of fainter stars, but attenuates the amplitudes in the diffraction pattern, thereby eliminating the high frequency information sought after in LO observations; a small aperture preserves high spatial resolution but

[2]There are approximately 20,400 stars in the SAO catalog close enough to the ecliptic to be occulted by the Moon; however there are only 124 stars listed in the recent catalog of stellar diameters (White & Feierman 1987). The other more than 20 thousand stars are too faint and small to be resolved with existing observational techniques.
More recently, the TIRGO group (Richichi *et al.* 1996) reported 157 NIR observations from 1985 that led to a total of 54 angular diameters and binary separations.

low SNRs limit the observations to very bright stars. The practical resolution limit imposed by the aperture of the 4-m telescope at Kitt Peak is $2.0-2.5$ mas (Ridgway 1982).

- the optical bandwidth. A broad optical band also improves the SNR but decreases the amplitude due to the wavelength dependence of the scale of the diffraction pattern; a narrow bandwidth minimizes the wavelength dependent distortion but results in low SNRs except for very bright stars.

- integration time. A long integration time increases the SNR but contributes to the "aperture smoothing" because the lunar shadow moves across the telescope during exposures. Additionally, long integration times reduce the number of data points because of the finite duration of the occultation event. Thus, increasing the integration time permits us to collect higher quality data for faint stars, in terms of SNR, but wipes out the high angular resolution information we seek in the data.

In the next section we review these factors in detail.

4.1 Aperture Smoothing

The diffraction pattern can be regarded as one-dimensional on the small scale of a telescope aperture. The characteristic scale of the monochromatic diffraction pattern is the radius of the first Fresnel zone, $\sqrt{\lambda d}$, where λ is the wavelength and d is the distance to the Moon (see Eq. 3.11). The distance between the n^{th} and

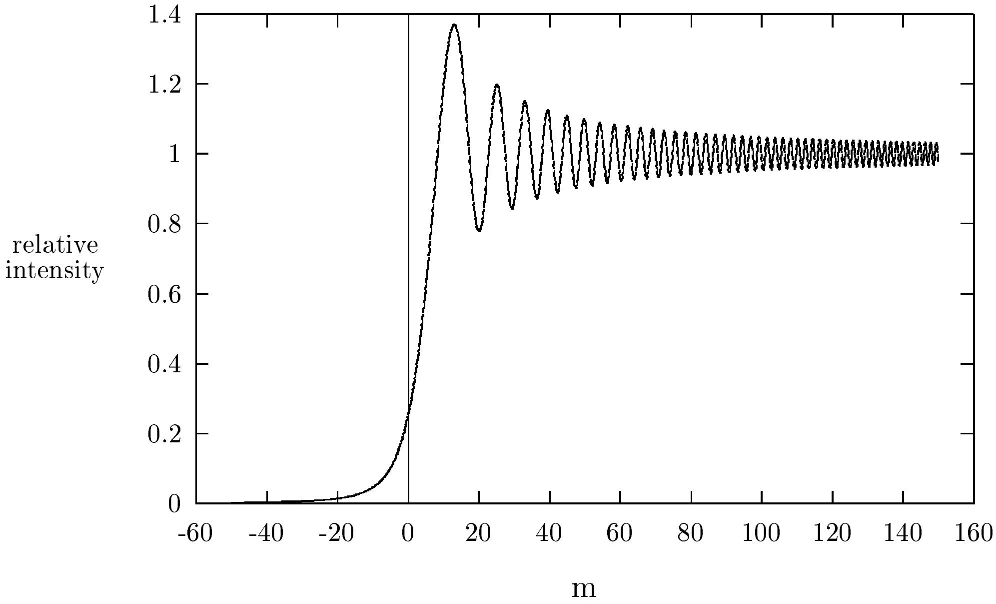

Figure 4.1: The intensity profile in the straight-edge diffraction pattern of a monochromatic point source. The separation between the diffraction fringes is monotonically decreasing with increasing n.

$(n+1)^{\mathrm{th}}$ maxima in the diffraction pattern of a point source occulted by a straight-edge lunar limb is

$$\sqrt{\frac{3+8(n+1)}{4}\lambda d}-\sqrt{\frac{3+8n}{4}\lambda d} \quad (n=0,1,2,...), \tag{4.1}$$

which monotonically decreases with increasing n (Fig. 4.1).

Multiple fringes fall within the aperture of a telescope of diameter D when

$$D \gg \sqrt{\frac{3+8(n+1)}{4}\lambda d}-\sqrt{\frac{3+8n}{4}\lambda d}. \tag{4.2}$$

Simultaneous detection of fringes results in an overall smoothing of fringes that finally leads to the total loss of fringe visibility (Fig. 4.2). In order to describe this smoothing effect quantitatively, we define the aperture function $A(x,y)$ of a circular telescope aperture in a rectangular coordinate system as

$$A(x,y) = \begin{cases} 1, \ \ if \ \ \sqrt{x^2+y^2} < D/2 \\ \quad 0, \ \ \text{otherwise} \end{cases} . \tag{4.3}$$

If the ordinate is oriented perpendicular to the fringes (parallel to their motion), then it is reasonable to define a weighting function w related to $A(x, y)$ such that

$$w(y) = \int A(x, y) dx. \tag{4.4}$$

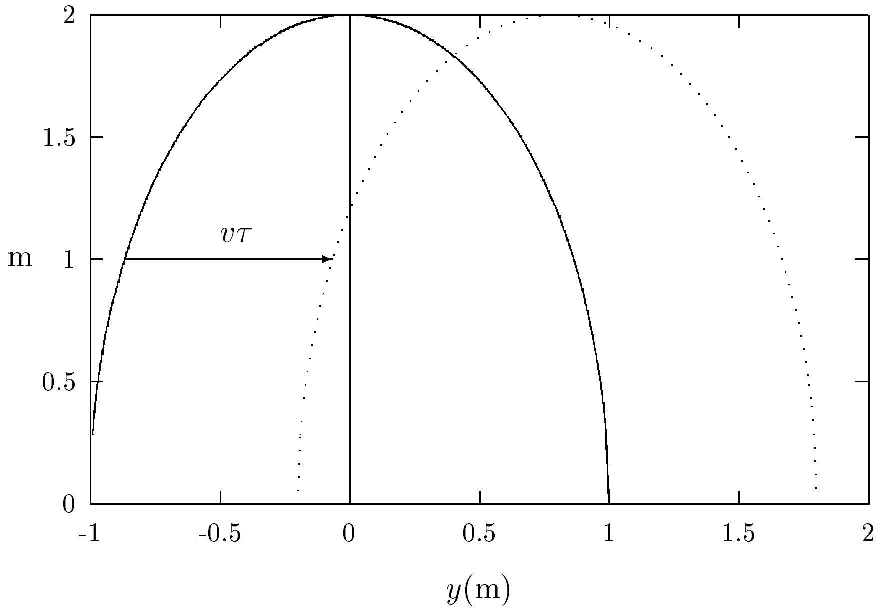

Figure 4.2: The weighting function $w(y)$ for $D = 2$ m, $\tau = 1.0$ ms and $v = 800$ m s^{-1}. $w(y)$ characterizes the weights of different sections of an aperture.

If the velocity of the diffraction pattern is v with respect to the telescope aperture, the i^{th} ($i = 0, 1, 2, ...$) output of the photometer after integration of time τ is proportional to

$$O_i \sim \int_{i\tau}^{(i+1)\tau} \int_{-\infty}^{+\infty} I(x + vt) w(x) \, dx dt, \tag{4.5}$$

where I is the irradiance distribution in the diffraction pattern. By substituting $u \equiv x + vt$ and changing the order of integrations, we get

$$O_i \sim \int_{-\infty}^{+\infty} I(u) \int_{i\tau}^{(i+1)\tau} w(u - vt) dt \, du. \tag{4.6}$$

We introduce a sampling function W (Fig. 4.3) such that

$$W(u - iv\tau) \equiv \int_{i\tau}^{(i+1)\tau} w(u - vt) dt \tag{4.7}$$

and then

$$O_i \sim \int_{-\infty}^{+\infty} I(u)\, W(u - iv\tau) du \; (i = 0, 1, 2, ...). \tag{4.8}$$

The data points ($i = 0, 1, 2, ...$) provided by conventional LO observations are the

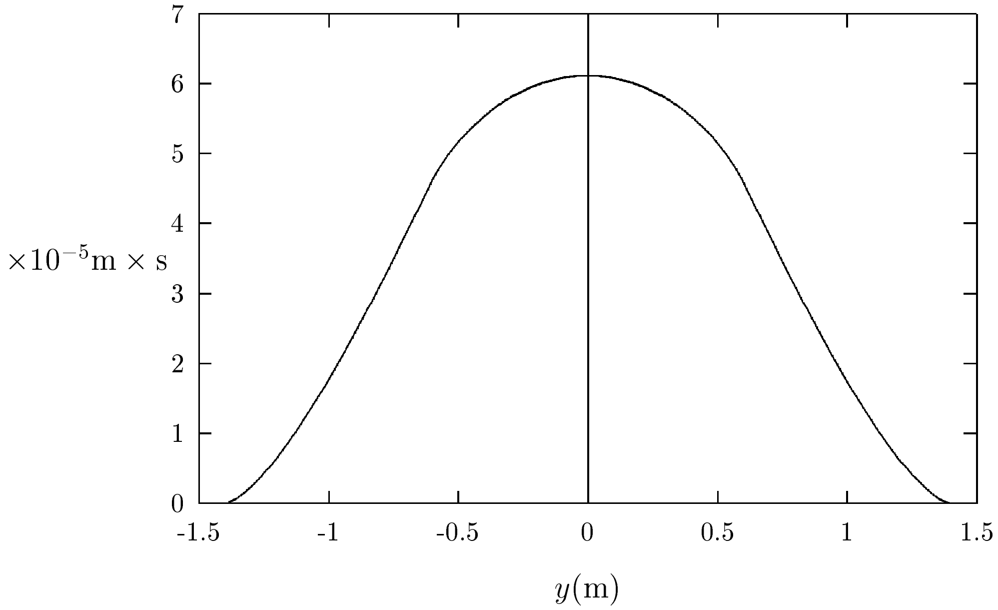

Figure 4.3: The sampling function $W(y)$. Since the diffraction pattern is moving during integrations by a distance of $v\tau$, the finite aperture of the telescope is taken into account by introducing $W(y)$. ($D = 2$ m, $\tau = 1.0$ ms and $v = 800$ m s^{-1})

integral of the diffraction pattern $I(u)$ and a sampling function $W(u)$ that is shifted in discrete steps $v\tau$ according to i. Equation (4.8) can be written as

$$O_i \sim \int_{-\infty}^{+\infty} \delta(y - iv\tau) \int_{-\infty}^{+\infty} I(u)\, W(u - y) du\, dy, \tag{4.9}$$

which is the mathematical sampling of the continuous function

$$O(y) = \int_{-\infty}^{+\infty} I(u)\, W(u - y) du \tag{4.10}$$

in steps $v\tau$. Equation (4.10) describes the LO observation as a linear shift-invariant system with impulse response $W(u)$. The sampling of $O(y)$ by a comb function $\int_{-\infty}^{+\infty} \delta(y - iv\tau)\, dy$ repeats the spectrum of O without distortion in the Fourier space.

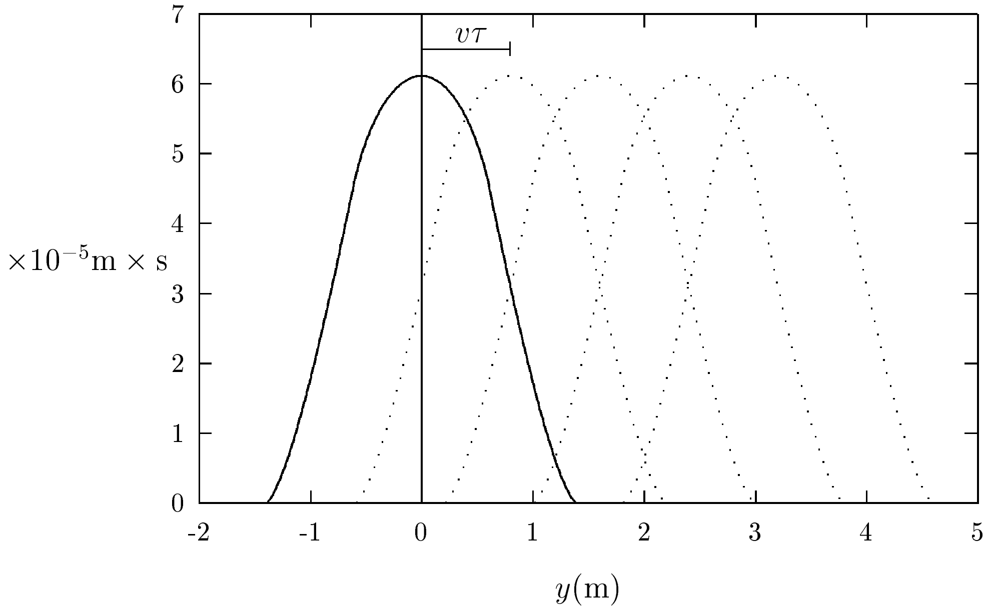

Figure 4.4: The diffraction pattern is sampled by $W(y - iv\tau), (i = 0, 1, ...).(D = 2$ m, $\tau = 1.0$ ms and $v = 800$ m s^{-1})

The separation between the spectra is $1/v\tau$. There is no overlap between the spectra if the data acquisition time[3] is not longer than D/v.

Clearly, a broad impulse response weakens the detect-ability of the fine fringes. The Fourier transform of the impulse response $W(y)$ of a linear system is the transfer function of the system (Fig. 4.5). The transfer function of an ideal system would be independent of frequency. However, real systems always have finite bandwidth. Beyond the upper limit of the band, Fourier components in the input signal are not transferred by the system. In our particular case, Fourier components in the diffraction pattern with spatial frequency $\nu \gg 2/(D + v\tau)$ are not transferred. The loss of high frequency components results in distortion in the light curve. Since a point source measured with a telescope of diameter D produces the same diffraction pattern as a source of angular size D/d measured with a point detector, the distortion

[3]The time between the end of an integration to the start of the next one.

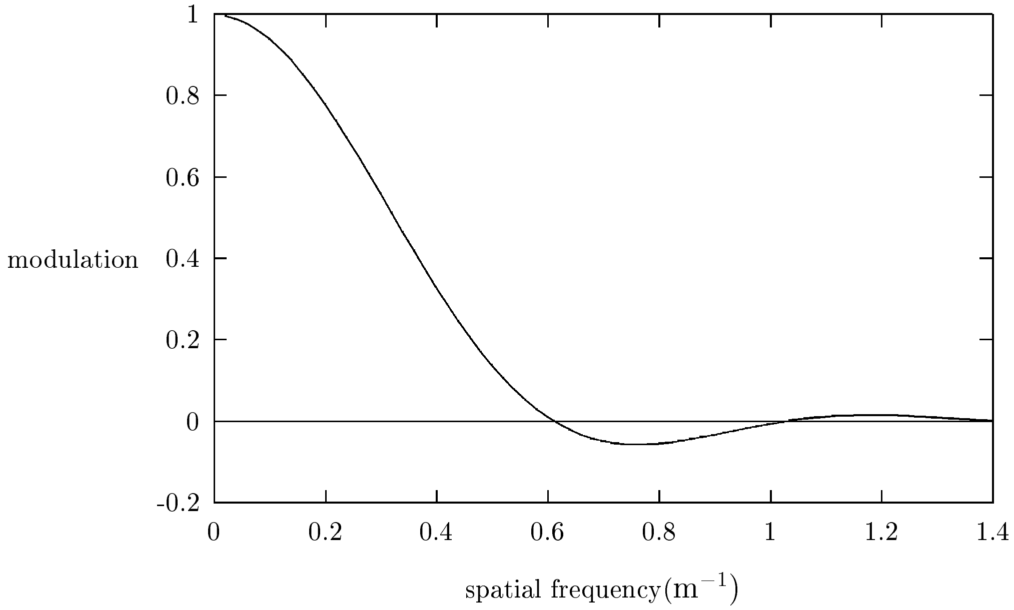

Figure 4.5: The normalized transfer functions of a circular aperture of diameter $D = 2$ m. ($\tau = 1.0$ ms and $v = 800$ m s^{-1}). The measuring system effectively filters out spatial frequencies higher than 0.7 m^{-1}.

in the light curve results in a spurious angular diameter of the source, given by

$$\phi_m \simeq \frac{D + v\tau}{d}. \tag{4.11}$$

Substituting for $d = 3.84 \times 10^8$ m and expressing ϕ_m in mas yields

$$\phi_m \simeq 0.54(D + v\tau). \tag{4.12}$$

In practice, τ is selected to be $1 - 2$ ms and, since 500 m s^{-1} $\leq v \leq$ 1000 m s^{-1}, we can approximate the practical angular resolution limit of a telescope of diameter D by

$$\phi_m \simeq 0.54(D + 1). \tag{4.13}$$

This formula gives $\phi_m = 2.7$ mas for the 4 m telescope at Kitt Peak that is in good agreement with Ridgway's $2 - 2.5$ mas estimate (Ridgway *et al.* 1980).

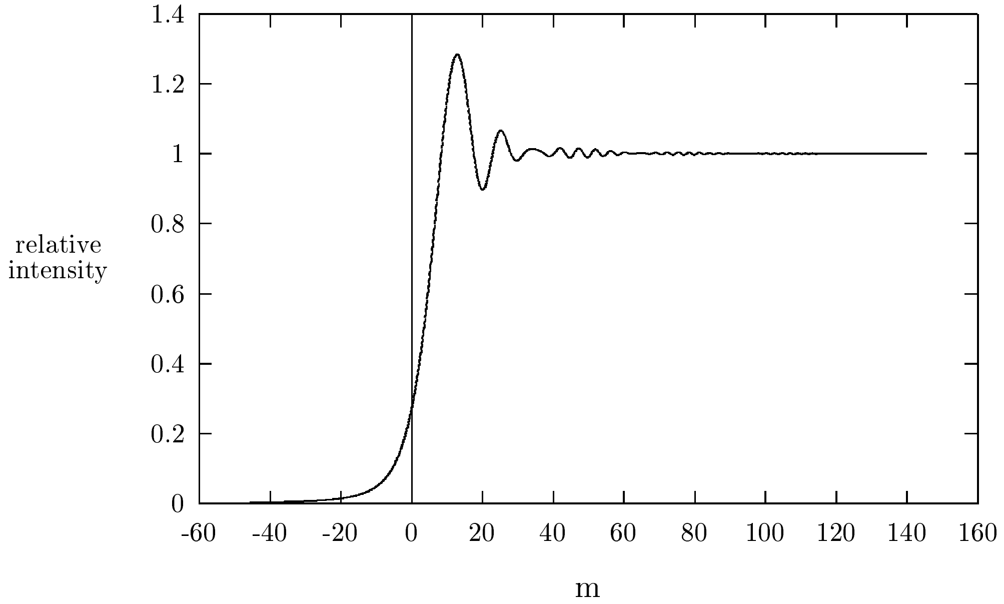

Figure 4.6: Fresnel diffraction pattern of a monochromatic point source detected by an 8-m telescope aperture. The large aperture results in condiderable distortion in the light curve.

4.2 Maximum Optical Bandwidth

We showed in Chapter III that the Fresnel diffraction pattern of a point source due to an infinite straight edge at wavelength λ can be expressed by Fresnel integrals (Eq. 3.11). Due to the argument $y\sqrt{2/\lambda d}$ of the Fresnel integrals, the abscissa scale of $I_\lambda(y)$ is wavelength dependent. However, all $I_\lambda(y)$ have a common point at $y = 0$ regardless of λ. If $G(\lambda)$ characterizes the relative strength of radiation detected in band $d\lambda$ at λ, then the observed[4] diffraction pattern is equal to

$$I(y) = \int_{-\infty}^{+\infty} I_\lambda(y) G(\lambda)\, d\lambda \tag{4.14}$$

because the intensity due to different spectral components can be combined incoherently. The net result of a finite optical band $\Delta\lambda$ is also a distortion in the light curve which attenuates the fringe amplitudes. The attenuation mimics an extended

[4]In order to distinguish between bandwidth and aperture smoothing, a point detector and zero integration time were assumed.

source and results also in a spurious diameter of the object (Fig. 4.7). Unlike Eq.

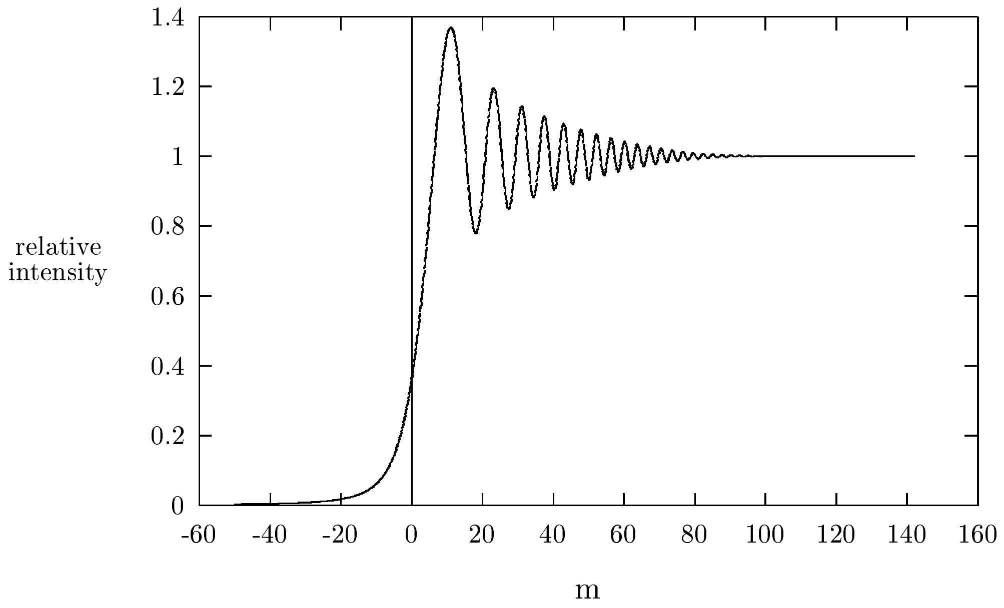

Figure 4.7: Fresnel diffraction pattern of a polychromatic point source detected by a small aperture in a broad (30 nm) optical band. ($D = 2$ m, $\tau = 1.0$ ms and $v = 800$ m s^{-1})

4.10, equation 4.14 is not a convolution integral; therefore, the distortion cannot be expressed in a simple manner. In order to characterize the spurious diameter induced by $\Delta\lambda$ we fitted an artificial light curve at $(\lambda, \Delta\lambda)$ of a point source by a set of monochromatic light curves at λ for sources of different diameters. Then we found the spurious diameter of the source as the diameter of the best fitting monochromatic source.

The position of the maxima and minima in the monochromatic diffraction pattern are at the following arc lengths s (measured along the Cornu spiral from the origin):

$$s = \sqrt{\frac{3+8n}{4}}, \text{ maxima,}$$
$$s = \sqrt{\frac{7+8n}{4}}, \text{ minima, } \; n = 0, 1, 2, \dots . \qquad (4.15)$$

s can be scaled to the corresponding distance on a plane at the telescope perpendicular to the line of sight by the relation

$$y = s\sqrt{\frac{\lambda d}{2}}, \tag{4.16}$$

where d is the observer's distance to the lunar limb. Then the locations of maxima and minima are

$$\begin{aligned} y_{\max} &= \sqrt{\frac{3+8n}{4}\lambda d}, \\ y_{\min} &= \sqrt{\frac{7+8n}{4}\lambda d}. \end{aligned} \tag{4.17}$$

Suppose the central wavelength of the optical band is λ_0. For $\lambda > \lambda_0$ ($\lambda < \lambda_0$) the positions of minima and maxima are farther from (closer to) the origin. No matter how small $|\lambda - \lambda_0|$ is, there is an n such that $y_{\max}(n, \lambda_0) = y_{\min}(n, \lambda < \lambda_0)$ or $y_{\max}(n, \lambda_0) = y_{\min}(n-1, \lambda > \lambda_0)$, i.e., the n^{th} maximum for wavelength λ_0 coincides with the n^{th} minimum for wavelength $\lambda < \lambda_0$ or the $(n-1)^{\text{th}}$ minimum for wavelength $\lambda > \lambda_0$. The diffraction pattern beyond $y_{\max}(n)$ is seriously distorted due to destructive interferences. Therefore, it is reasonable to define the maximum allowable bandwidth $\Delta\lambda$ by requiring the minimum n at which this distortion occurs.

We have already shown that an "effective" aperture $D_{eff} = 2D$ filters out spatial frequencies larger than $1/D_{eff}$. In order to keep balance between the aperture and bandwidth smoothing, let us chose the minimum required n such that

$$y_{\max}(n+1, \lambda_0) - y_{\max}(n, \lambda_0) < D \tag{4.18}$$

holds only when $n > n_{\min}$. By solving (4.18) for n

$$n = \frac{D^4 - 7dD^2\lambda_0 + 4d^2\lambda_0^2}{8dD\lambda_0}. \tag{4.19}$$

The maximum and minimum allowable wavelengths $\lambda_{\max}$ and $\lambda_{\min}$ for this n are

$$\begin{aligned}\lambda_{\max} &= \lambda_0 + \frac{D^2}{d} + o(\frac{D^2}{d})^2, \\ \lambda_{\min} &= \lambda_0 - \frac{D^2}{d} + o(\frac{D^2}{d})^2\end{aligned} \tag{4.20}$$

and the maximum bandwidth $\Delta\lambda = \lambda_{\max} - \lambda_{\min}$ is

$$\Delta\lambda \simeq \frac{2D^2}{d} \tag{4.21}$$

independently of λ_0. Expressing $\Delta\lambda$ in nanometers and D in meters yields

$$\Delta\lambda\,[\mathrm{nm}] \simeq 5.2D^2. \tag{4.22}$$

For a telescope with $D = 2$ m, equation (4.22) yields $\Delta\lambda \simeq 21$ nm. However, for a small ($D = 0.5$ m) telescope, the bandwidth limit is about $\Delta\lambda = 1.3$ nm. The optical band used in traditional LO observations is usually selected from the standard UBVRI system where the bandwidths are much broader than 1.3 nm or even 21 nm; therefore, the bandwidth is the dominant smoothing factor although the SNR may not be high enough for this to be noticed.

From (Eq. 4.13) and (Eq. 4.22) the bandwidth-limited resolution in mas is

$$\phi_m \simeq 0.5\sqrt{\Delta\lambda[\mathrm{nm}]}, \tag{4.23}$$

which is in good agreement with the value of Ridgway (1977) .

4.3 Sampling Time

LO events have a characteristic time scale determined by the speed of the diffraction pattern with respect to the observer and by the extent of resolvable features along the diffraction pattern. Therefore, the sampling time affects the performance of LO observations not only because long exposure tends to smooth out the fine fringes but it also limits the number data points available for model fitting procedures (Richichi 1996).

4.4 Conclusion

As we have seen in this chapter, there is an **unresolvable trade-off** between obtaining high SNR and low distortion in the light curve. A large telescope aperture and/or long integration time and/or broad optical bandwidth would result in a high SNR but all of these tend to limit the spatial bandwidth, i.e., we obtain high SNR but lose most of the desired spatial information embedded in the data. Or, one can improve the spatial resolution without limit by decreasing the telescope aperture, applying a narrow optical filter and very short integration time the expense of SNR. The observer has to compromise between high SNR and high spatial resolution[5]

[5]In the near infrared the scale of the diffraction pattern is larger. Therefore, these restrictions are not as severe as in the optical range of the spectrum.

CHAPTER V

THE TDI METHOD

5.1 How TDI Works

Two different approaches are used for recording moving objects. The first, used in drum cameras, involves taking a series of snap-shots with exposures much shorter than the characteristic time scale of the motion. This is a fairly general approach that does not require detailed *a priori* knowledge about the motions of the objects being recorded, and can be employed to record the simultaneous movement of many differently moving objects. For example, this technique is used to record the outrush of the fragments of an explosion, the rapid flapping of the wings of a hovering hummingbird, or the myriad activities of actors in a movie scene in Hollywood. A serious problem with this approach is that, with increasing object speeds, the time durations of individual snap-shots have to be decreased to avoid blurring. Shorter exposures require very strong illumination which is, in many cases, too expensive to implement or impractical to apply. The conventional method of observations of LOs follows this approach.

The second approach involves tracking moving objects during exposures. This approach is not as general as the former because, at any given time, only one object with predictable motion can be tracked. Nevertheless, there are many situations when objects move uniformly in one direction with known velocity, for example products moving on a conveyor belt, a document in a scanner, and stars in the focal plane of a telescope.

Time-delay integration (TDI) is a scanning technology that utilizes the second concept, i.e., tracking moving objects during exposures. This technology has been in extensive use for close to 20 years in industrial applications (Barbe 1976; Washkurak *et al.* 1989, Chamberlain & Washkurak 1990) and occasionally in astronomy since 1982 (Mackay 1982). The benefits offered by TDI over conventional CCD imaging in large area surveys of low surface brightness astronomical objects are considerable (McGraw 1982; Sloan Sky Survey; Zaratsky *et al.* 1996). Early use of TDI was limited by the high cost of TDI devices at that time, but favorable trends in cost and ease of use have greatly increased TDI usage.

Tracking itself is hardly a new concept in astronomy; however, the way in which tracking is implemented here is new and requires CCDs. The CCD is steady and must be oriented in such a way that electron transport in the parallel register of the CCD matches the direction of motion of the astronomical object or light pattern. As the optical image of the moving object shifts across the CCD, its electronic counterpart, the photoelectron image, is shifted synchronously with it by proper control of the CCD. The total exposure possible with this method can be as long as the time required for the image of the object to move completely across the stationary CCD, since during that time the photoelectrons continue to accumulate. If the synchronization of the speeds of the moving optical image with the moving electronic image is accurate, the net result is a sharp image of the moving object. The longer exposure increases the sensitivity of the method, but does not cause image blurring.

5.2 Application of TDI to Lunar Occultations

The rapidly moving diffraction pattern of an occulted star is ideally suited to TDI observations because the pattern moves at uniform speed and can be considered one-dimensional on the small scale of a single telescope aperture. The advantages of the TDI concept in LO studies was suggested by Sturmann (1994). A CCD camera operating in TDI mode on a large telescope could considerably improve the sensitivity of LO measurements by increasing the total integration time without the drawbacks of losing time resolution and/or causing increased blurring by the large aperture. The CCD has to be placed in the pupil plane of the telescope by re-imaging the telescope aperture on the CCD with a short focal length objective[1] (Fig. 5.1). Ideally, the CCD should be oriented in such a way that the direction of the electron transport in the parallel register matches the direction of motion of the fringes to better than $1/2N$ radians, where N is the total number of pixels in a column of the CCD. The passing diffraction fringes are tracked by shifting the photoelectrons in the parallel register row by row synchronously with the moving fringes (Fig. 5.2). Projecting the rows of the CCD back onto the telescope primary, we have effectively sliced the aperture –and the passing diffraction pattern– into a series of strips or sub-apertures. Each sub-aperture corresponds to one row and each row receives photons from its own sub-aperture. The sub-apertures have identical widths p but different light collecting areas a_i. While the diffraction pattern is moving in front of the "sliced" aperture with speed v, the rows in the parallel register integrate the corresponding parts of the pattern for time p/v during which the pattern advances with p. After time p/v, the accumulated

[1] The objective could be cylindrical, forming a line image of the telescope aperture on the CCD, since the diffraction pattern is one- dimensional. This would increases the illumination on the CCD but would make it impossible to detect possible alignment errors in the orientation of the CCD.

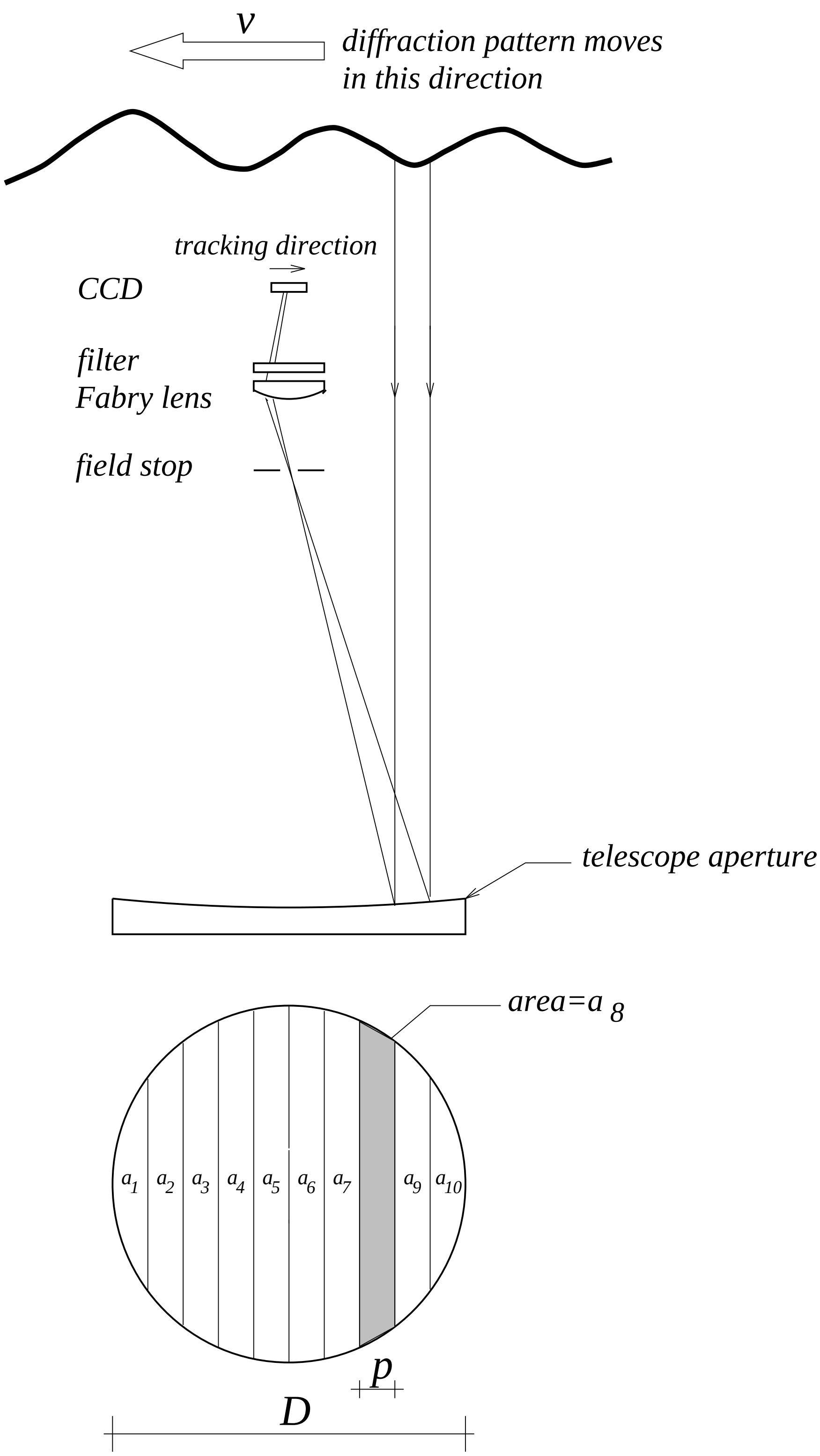

Figure 5.1: The moving diffraction pattern of an occulted star is reimaged onto a properly oriented CCD array. The rows of the CCD effectively slice the aperture of the telescope into strips of uniform width p. By binnig k rows, we can define wider superstrips of width P.

photoelectrons are passed into the next row and from the last row into the serial shift register to be read out (Fig. 5.2). The number of photoelectrons corresponding to each strip of the diffraction pattern continues to grow as the electrons are stepped all the way across the parallel register.

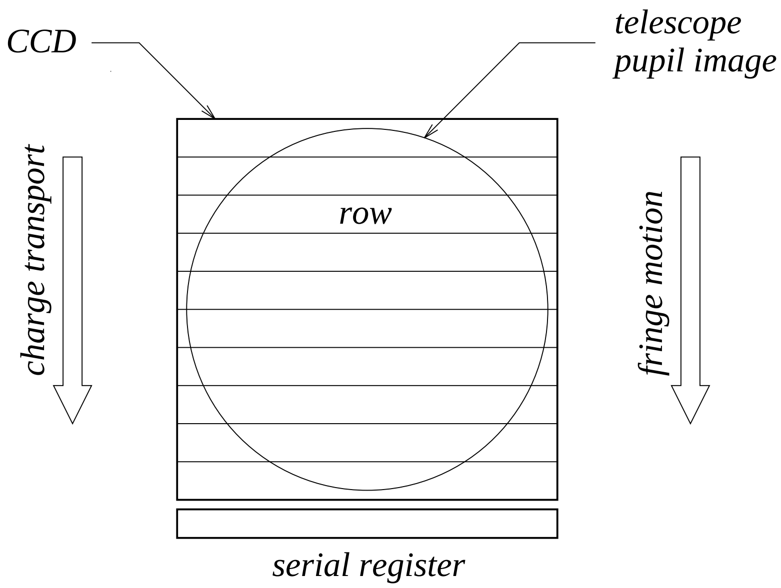

Figure 5.2: By stepping the photoelectrons in the parallel register synchronously with the moving diffraction pattern, we can increase the effective integration time yet preserve the high angular resolution information in the diffraction pattern.

5.3 Technical Feasibility

There are two requirements for keeping the tracking synchronous with the moving diffraction pattern: the speed of shifting the electrons across the parallel register and the speed of reading out the electrons from the serial register. If the projected pixel size on the telescope aperture is p and the speed of the diffraction pattern is v, the electronic image will not be left behind by the optical image if the minimum time required to shift the electronic image by one row is less than or equal to p/v. This minimum time, which is determined by the time constant of electron diffusion between adjacent electrodes, is less than a microsecond. Proper timing is necessary, however, to achieve high charge transfer efficiency.

Between subsequent parallel shifts we want to read out D/p pixels from the serial register. This leads to a read-out rate of Dv/p^2 pixels/sec. Since it is unreasonable to use $p < 0.2$ m due to the seeing (Young 1971), the read-out rate will be less than 250 $\mathrm{kpx\,s^{-1}}$ even with $D = 10$ m and $v = 1\ \mathrm{m\,ms^{-1}}$ (worst case scenario).

Slow-scan astronomical CCD cameras provide read-out rates of about 50 kpx s^{-1} to achieve 16-bit dynamical range. However, the read-out rate can be increased considerably by decreasing the digital depth. 4 Mpx s^{-1} readout rate at a dynamic range of 3000 ($>$ 11 bit) is readily available (DALSA IA-D1 Turbosensor) and 8 bit dedicated TDI sensors provide more than 15 Mpx s^{-1}. Although 8-bit is not enough for TDI lunar occultation studies, 11-12 bits seems to be adequate. Therefore, the application of CCDs in TDI mode to LO observations is technically feasible.

5.4 Benefits of TDI

By tracking the diffraction pattern, we are able to use large telescope apertures. This yields long total integration times and high SNRs without sacrificing the spatial resolution in the diffraction pattern.

Let the total area of the aperture of the telescope be

$$\sum a_i \simeq \frac{\pi D^2}{4}, \tag{5.1}$$

where we neglect the central obscuration of the telescope. A particular element of the diffraction pattern spends time p/v in front of each strip with area a_i. Therefore, the net signal in one data point is proportional to $a_1 p/v + a_2 p/v + ...$

$$\frac{p}{v}\sum a_i \simeq \frac{p}{v}\frac{\pi D^2}{4}. \tag{5.2}$$

The total exposure for each data point is

$$\tau_{tot} = \frac{D}{v}. \tag{5.3}$$

Assuming that every k rows are binned together into the serial register before readout, the effective diameter D_{eff} of a telescope that would produce the same signal during total exposure τ_{tot} as the "sliced" telescope is found from

$$\frac{D}{v}\frac{\pi D_{eff}^2}{4} = k\frac{p}{v}\frac{\pi D^2}{4} \tag{5.4}$$

and

$$D_{eff} = \sqrt{PD}, \tag{5.5}$$

where $P \equiv kp$. For example, if the projected width of a CCD row were $p = 0.2$ m and we were to slice the aperture of a $D = 8$ m telescope into $P = 1$ m wide strips by binning into every $k = 5$ rows, the effective light-gathering capability of this system would be equivalent to that of a $D_{eff} = 2.8$ m telescope. If the speed of the diffraction pattern was $v = 0.8$ m ms^{-1}, the total integration time would be $\tau_{tot} = 10$ ms for every strip across the 8-m aperture. Despite the large aperture and long integration time, the overall smoothing of the fringes would be equivalent to that of a 1 m telescope[2] with an integration time[3] of 0.25 ms.

[2]If the alignment of the CCD were perfect.

[3]During this 0.25 ms the diffraction pattern moves although we are not tracking. This discrete time interval p/v between each step induces a small amount of blurring. A similar blurring effect is present in the conventional method at a larger scale due to the longer integration time (≈ 1 ms).

In order to compare SNRs obtainable by the conventional and TDI methods, let us first take a telescope with diameter D that is equipped with a conventional single-channel photometer (Fig. 5.3). When the total number of photons due to a star and sky background at the detector are N_* and N_b, respectively, then the input SNR is

$$SNR_{cnv} = \frac{N_*}{\sqrt{N_* + N_b}}. \tag{5.6}$$

Now, let us take a telescope with diameter of nD ($n > 1$) that utilizes a TDI

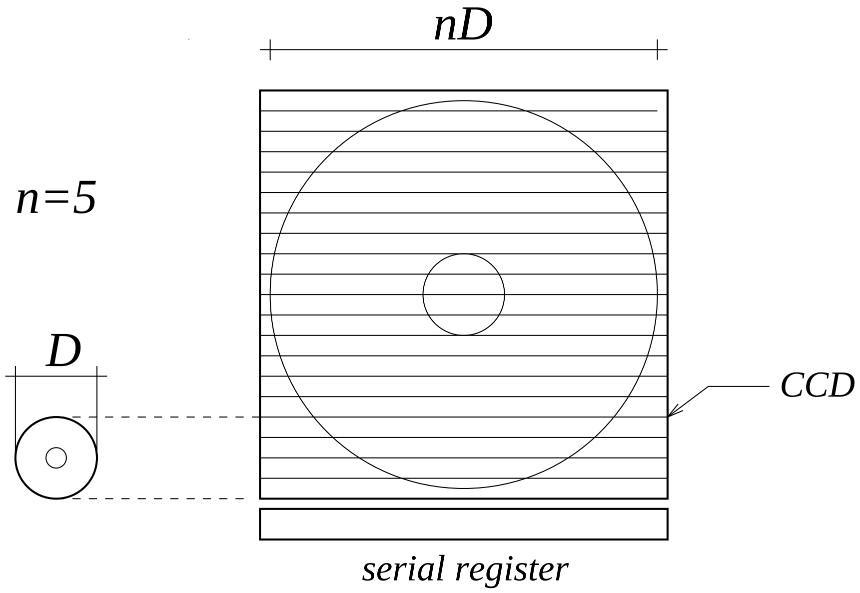

Figure 5.3: An n times larger telescope aperture provides n times larger SNR at the same level of distortion in the light curve.

detector. Note that this telescope, even with an aperture n times larger, results in no more distortion in the light curve than the smaller telescope of diameter D. The total signal at the TDI detector is $n^2N_* + n^2N_b$; therefore, the SNR is

$$SNR_{TDI} = \frac{n^2N_*}{\sqrt{n^2N_* + n^2N_b}} = n\,SNR_{CNV}, \tag{5.7}$$

i.e., there is a gain of a factor of n in the SNR. If we assume that the achievable angular resolution goes like SNR^{-1} (Lang 1971, Richichi 1996), then a telescope n times larger could provide angular resolution n times higher.

5.5 Mathematical Modeling of TDI

The telescope aperture is imaged by a Fabry lens onto the CCD where the image of the telescope aperture covers a number of pixels. The spatial resolution in the diffraction pattern will be limited by the projected size p of pixels on the telescope aperture[4]. The size p can be changed by adjusting the focal lens of the Fabry lens according to the actual observational circumstances. If the diameter of the telescope aperture is D, then the number of tracking steps is $N = D/p$. The tracking occurs in discrete steps in the CCD. Between tracking steps the diffraction pattern moves while we are not tracking. This results in blurring that decreases the spatial resolution.

In conventional LO observations the direction of fringe motion does not play any significant role due to the circular symmetry of the telescope-detector system. The TDI occultation setup is not circularly symmetric. The CCD has to be oriented properly to match the direction of fringe motion. However, this direction is *a priori* unknown and the CCD can be oriented only according to the predicted direction of fringe motion. This orientation error is unavoidable because of our imperfect knowledge about the shape of the lunar limb.

The effect of finite pixel sizes, the discreteness of tracking, and the alignment error of the CCD are interrelated. In this section we develop a mathematical model that can be used to evaluate the impact of these three factors on the spatial resolution in the diffraction pattern.

[4]The tracking will be described in the aperture plane of the telescope.

5.5.1 Pixel Weighting Function

The finite sizes of pixels and the continuous motion of the fringe pattern can be conveniently described by introducing the pixel weighting function W.

Let us define a Cartesian coordinate-system with base vectors $\mathbf{i}, \mathbf{j}$ such that the diffraction pattern moves in the $-\mathbf{j}$ direction (Fig. 5.4). Let $\mathcal{A}$ represent a fully illuminated domain (pixel) in the aperture plane[5]. Between any two tracking steps,

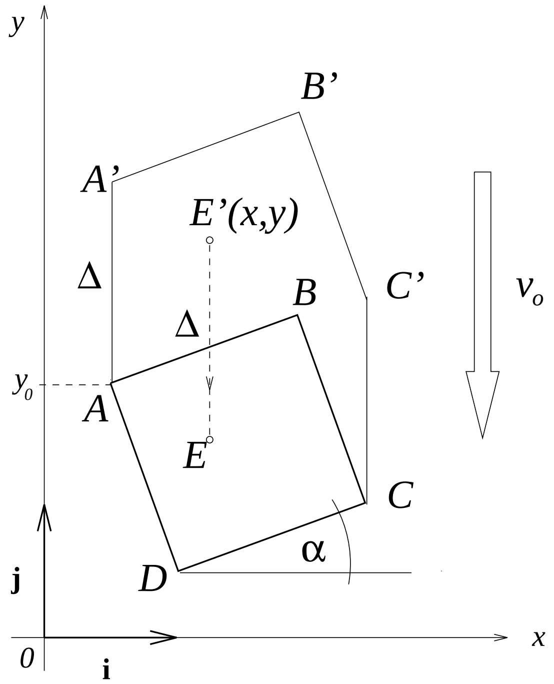

Figure 5.4: The rectangle $\mathcal{A} = ABCD$ represents a pixel. The diffraction pattern moves in the $-\mathbf{j}$ direction. There is an error α in the orientation of the CCD.

the diffraction pattern shifts by $\overline{AA'} = \Delta$ with respect to the telescope. Let us define another domain $\mathcal{B} = AA'B'C'CD$ whose points are seen for some time ($< \tau$) by $\mathcal{A}$ during τ. Some points in $\mathcal{B}$ shift in front of $\mathcal{A}$, some of them leave $\mathcal{A}$ before the end of an integration. Let $w(A)$ be the total exposure of the point A during τ, i.e.,

[5]We introduce W in a general form for a domain of arbitrary shape. If $\mathcal{A}$ is a fully illuminated pixel, then $\mathcal{A}$ is a square domain of size p; otherwise it has a more complicated shape. Additionally, the border of a pixel is not necessarily aligned parallel to the coordinate axes, because of the alignment error in the orientation of the CCD.

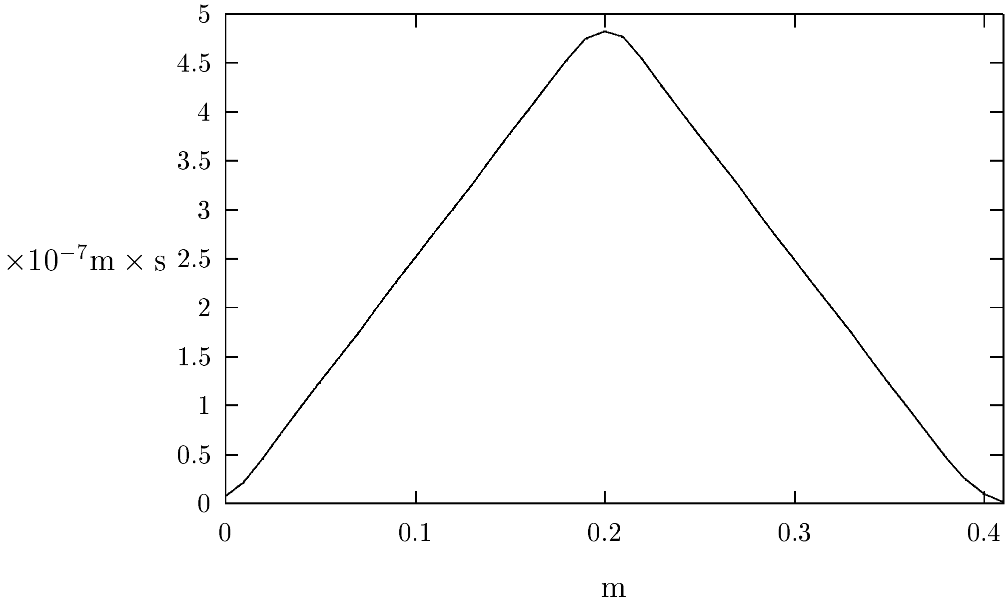

Figure 5.5: The pixel weighting function $W(y)$ for $\alpha = 10°$, $\varphi = 40°$, and $p = 0.2$ m.

$$w\left(A\right) \equiv \frac{\text{section of } \overline{AA'} \text{ inside } \mathcal{A}}{\Delta}\tau. \tag{5.8}$$

Note that $w \equiv 0$ for points outside domain $\mathcal{B}$.

Since the diffraction pattern can be regarded as one-dimensional and the fringes are perpendicular to $\mathbf{j}$ due to the special selection of the coordinate system, the irradiance pattern is independent of the coordinate x. Therefore, it is reasonable to define the pixel weighting function $W(y)$ such that

$$W(y) \equiv \int_{-\infty}^{+\infty} w(x,y)\,dx \tag{5.9}$$

and

$$\int_{-\infty}^{+\infty} W(y)\,dy = area(\mathcal{A})\tau. \tag{5.10}$$

If the irradiance in the moving diffraction pattern is $I(y + v_o t)$, then the i^{th} ($i = 0, 1, 2...$) output of a single pixel ($\mathcal{A}$) is proportional to

$$O_i = \int_{-\infty}^{+\infty} I(y + iv_o\tau)W(y)dy. \tag{5.11}$$

It is equivalent to say that O_i is the convolution of domain $\mathcal{A}$ and the moving diffraction pattern

$$O_i = \int_{i\tau}^{(i+1)\tau} \int_{-\infty}^{+\infty} I(y + vt) \int_{-\infty}^{+\infty} \mathcal{A}(x, y) dx\, dy dt. \tag{5.12}$$

The justification of introducing $W(y)$ is that (Eq. 5.11) can be computed much faster than (Eq. 5.12) since $W(y)$ can be computed in advance and (Eq. 5.11) is a simple integral for every i while (Eq. 5.12) is a convolution integral for every i.

If the number of illuminated pixels is large, then only a small percentage of them are not fully illuminated [6] and we can assume the same $W(y)$ for every pixel. The situation is somewhat more complicated when the telescope aperture is imaged to only a small number of pixels and $W(y)$ is not the same for different pixels.

Let us now turn to the effects of alignment error.

Suppose the lunar limb at the location where the occultation occurs can be characterized as having an inclination angle α to the datum that represents the theoretical smooth limb[7]. The predicted direction of fringe motion is based on the angle of incidence φ of the occultation. Assume the CCD has been oriented properly, with the rows parallel to the theoretical smooth lunar limb. If α were zero, the diffraction fringes would be parallel to the rows of the CCD and they would move perpendicularly to the rows with velocity of $v \cos\varphi$, where $v = |\mathbf{v}|$ and $\mathbf{v}$ is the projected velocity of the center of the Moon to the sky. If $\alpha \neq 0$, the fringes not only are inclined to the rows but their velocity projected to the direction of tracking also differs from the predicted value and that causes blurring in the recorded fringe pattern. The predicted

[6] There are partially illuminated pixels at the edge of the pupil image on the CCD.

[7] We do not consider crevasses and sharp peaks on the limb due to their apparent rarity and due to the mathematical intractability of including them in the analysis.

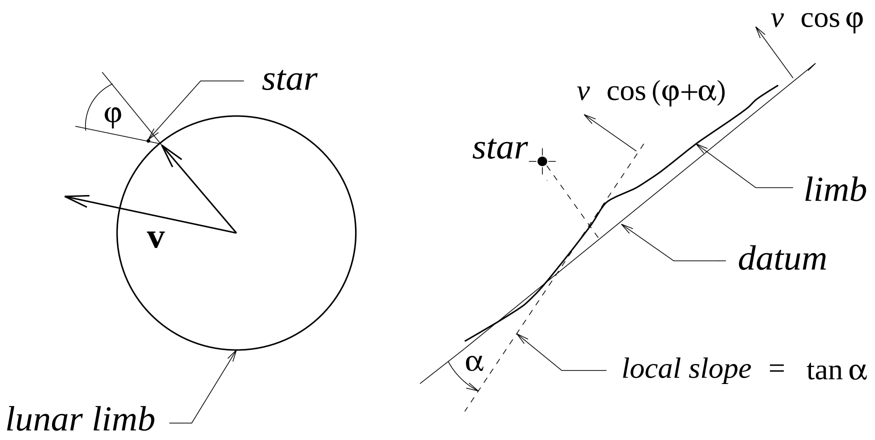

Figure 5.6: The local limb can be characterized by its inclination α to a datum. φ is the angle of incidence (or contact angle), the angle where the occultation occurs with respect to the velocity vector $\mathbf{v}$.

speed of the fringes is

$$v_c = v \cos\varphi \tag{5.13}$$

while their observed speed is

$$v_o = v \cos(\varphi + \alpha). \tag{5.14}$$

The predicted time between charge shifts in the parallel register is

$$\tau = \frac{p}{v_c}, \tag{5.15}$$

where p is the projected width of CCD rows on the aperture of the telescope. Between each two shifts, the diffraction pattern moves by

$$\Delta = \tau v_o = p\frac{v_o}{v_c} = p\frac{\cos(\varphi + \alpha)}{\cos\varphi}, \tag{5.16}$$

while the photoelectrons are shifted by p. Since we are concerned only with motion along $\mathbf{j}$, the tracking is synchronous if and only if $\Delta = p\cos\alpha$, i.e.,

$$\frac{\cos(\varphi + \alpha)}{\cos\varphi\cos\alpha} = 1. \tag{5.17}$$

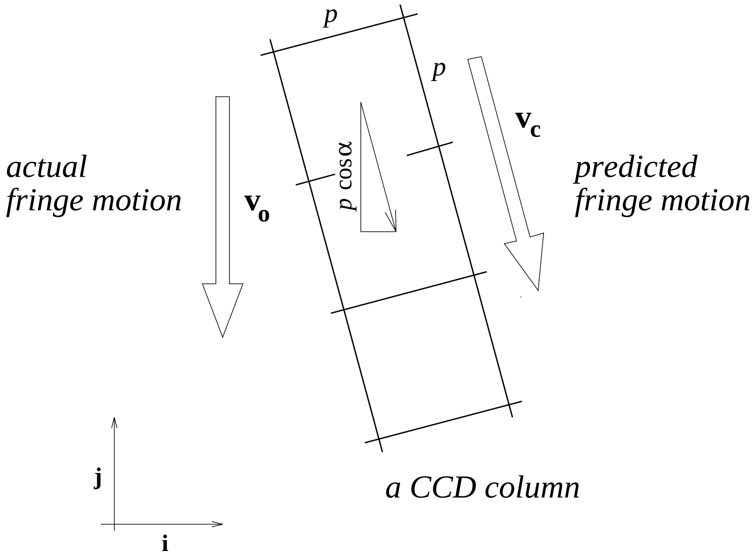

Figure 5.7: The tracking is strictly synchronous when $\Delta/\cos\alpha = p$.

Therefore, the tracking is perfect only when $\alpha = 0$ and/or $\varphi = 0$. The electronic image and the fringes gradually go out of phase as the tracking progresses across the CCD. However, the TDI method has a certain tolerance against the tracking error due to the finite p and the finite number of tracking steps N. After N steps of tracking, the separation between the optical and electronic image due to a velocity mismatch $\Delta v = |v_o - v_c|$ is $Np\Delta v/v_c$. If the separation is less than $2p$, the velocity mismatch has minor effect on the spatial resolution (Barbe 1976), i.e.,

$$\frac{\Delta v}{v_c} N < 2. \tag{5.18}$$

Even when this factor is greater than 2, the effect is incremental and may not be noticeable until a value greater than $\sim$4 is reached. Therefore, if we have $N = 64$, then $\Delta v/v$ can be as high as 3% without causing any significant resolution degradation effects.

In order to evaluate the impact of the unknown α to the spatial resolution we have computed domains in the (φ, α) space in which (5.18) is satisfied for $N = 8$, 16,

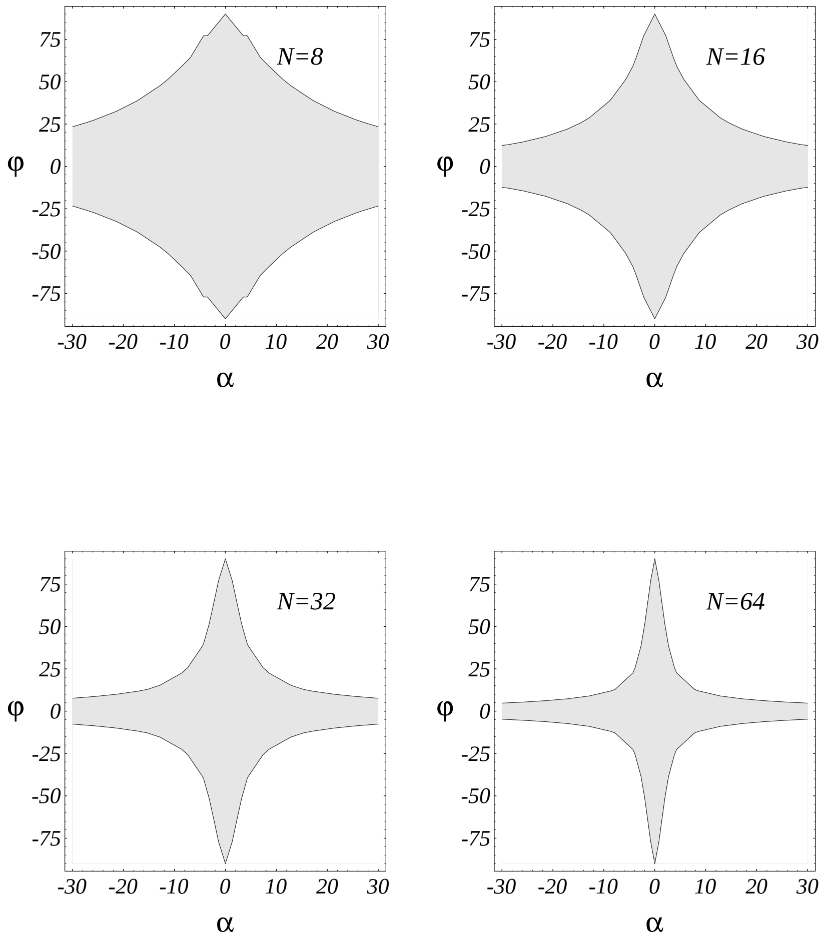

Figure 5.8: $N\Delta v/v < 2$ in the shaded areas for $N = 8, 16, 32$ and 64. If the occultations occurs in the shaded parameter space (α, φ) then the velocity mismatch between the tracking and the actual motion of the sky has minor effect on the spatial resolution.

32, and 64 tracking steps corresponding to 8×8, 16×16, 32×32 and 64×64 arrays (Fig. 5.8).

The probability density function of α is unknown; however, from LO observations we know that $|\alpha|$ almost never exceeds 30°. Since it is likely, that the probability density function for α is concentrated around $\alpha = 0$, we assume a Gaussian distribution with density function of

$$f_\alpha(\alpha) = \frac{1}{\sigma_\alpha \sqrt{2\pi}} e^{-\frac{\alpha^2}{2\sigma_\alpha^2}} \tag{5.19}$$

and with $2\sigma_\alpha = 30°$.

The occurrence of an occultation is equally probable in the cross-section of the lunar limb therefore, the angle of incidence φ is not uniformly distributed over the range $(-90°, +90°)$. φ is more likely close to 0° than to ±90°. We define a function

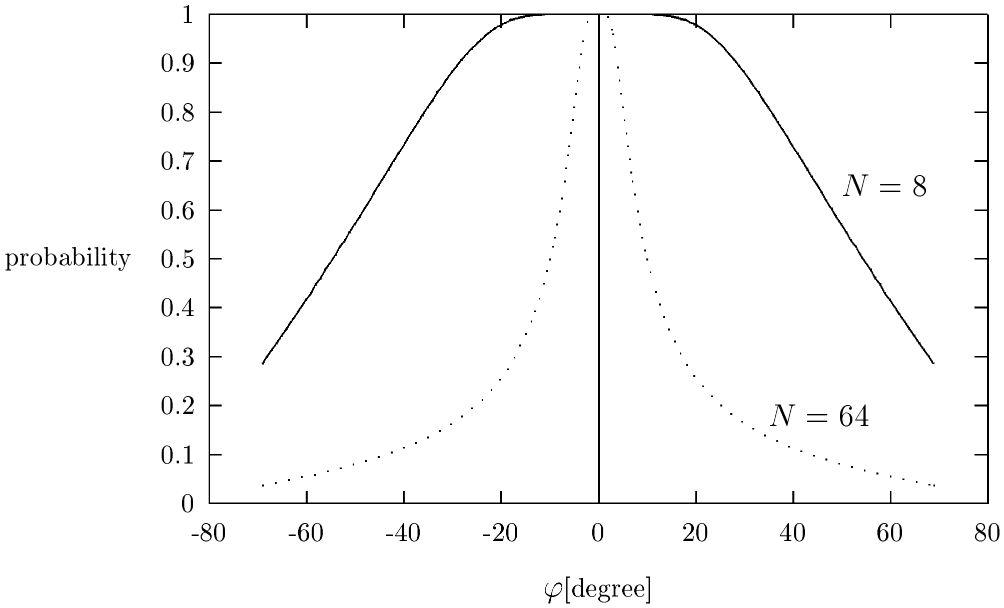

Figure 5.9: The probability that an unknown α does not cause noticeable distortion in the light curve as a function of φ. We assume that α has Gaussian distribution with mean and standard deviation of $(0, 15^{circ})$.

which provides the probability of not having noticeable distortion in the light curve due to α at a given φ by integrating the shaded domains over α. The blurring in the fringe pattern can be too small to notice even at $\alpha \neq 0$.

5.5.2 The Tracking

For the sake of simplicity, let us assume a perfect CCD of $N \times N$ pixels and with no noise sources. Also, we neglect all noises associated with photon detection process and with atmospheric turbulence (these noises and their effects are discussed in Chapter 6.2) and we assume a quantum efficiency of unity and uniform sensitivity over all pixels.

Let $I(y)$ be the photon irradiance in the pupil plane in units of photons m^{-2} s^{-1} integrated over the wavelength band of width $\Delta\lambda$ at central wavelength λ. Let us consider first only one pixel (i, j), where $i = 1...N$ for the rows and $j = 1...N$ for the columns (Fig. 5.10). Let the pixel $(1, 1)$ be at $y - y_0$, where y_0 is an arbitrary point to fix the position of the diffraction pattern at $t = 0$. Then, after i steps, the pixel (i, j) integrates the diffraction pattern at

$$y_{ij} = y - y_0 + (i-1)(\Delta - p\cos\alpha) + (j-1)p\sin\alpha, \tag{5.20}$$

where α is the alignment error due to the unknown inclination of the lunar limb and Δ is the amount of shift of the diffraction pattern during an exposure τ (Fig. 5.10). After N steps the number of electrons transferred to the j^{th} pixel in the serial register is proportional to

$$s_{1j} = \sum_{i=1}^{N} T_{ij} \int_{-\infty}^{+\infty} I(y - y_0 + (i-1)(\Delta - p\cos\alpha) + (j-1)p\sin\alpha) W(y) dy, \tag{5.21}$$

where W is the pixel weighting function and T_{ij} is the telescope aperture function. T_{ij} is ratio of the illuminated and total areas of pixel (i, j). Substituting $y' \equiv y + (i -$

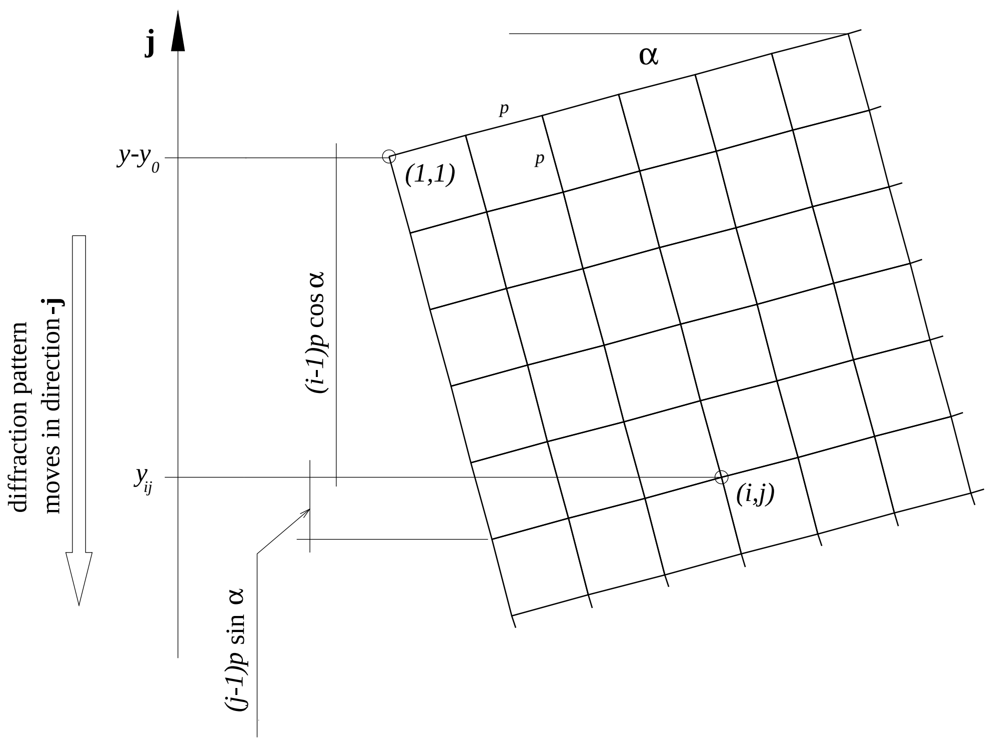

Figure 5.10: Illustration for tracking.

$1)(\Delta - p\cos\alpha)$ into (Eq. 5.21) and suppressing the prime leads to

$$s_{1j} = \int_{-\infty}^{+\infty} I(y - y_0 + (j-1)p\sin\alpha) W_j^c(y)dy, \tag{5.22}$$

where we introduced the weighting function $W_j^c(y)$ (Fig. 5.11) of an entire column as

$$W_j^c(y) = \sum_{i=1}^{N} T_{ij} W(y - (i-1)(\Delta - p\cos\alpha)). \tag{5.23}$$

The first row in the output of the TDI camera would be $\{s_{11}, s_{12}, ..., s_{1N}\}$ if we were to read out the serial register without binning.

The signal in the j^{th} $(j = 1, 2, ..., N)$ pixel of the k^{th} $(k = 1, 2, ...)$ output row can be found easily because the only difference between the first and k^{th} row is that the integration of the k^{th} row starts time $(k-1)\tau$ later during which the diffraction pattern moved $(k-1)\Delta$. Consequently, the signal in the k^{th} output row is

$$s_{kj} = \int_{-\infty}^{+\infty} I(y - y_0 + (j-1)p\sin\alpha + (k-1)\Delta) W_j^c(y)dy. \tag{5.24}$$

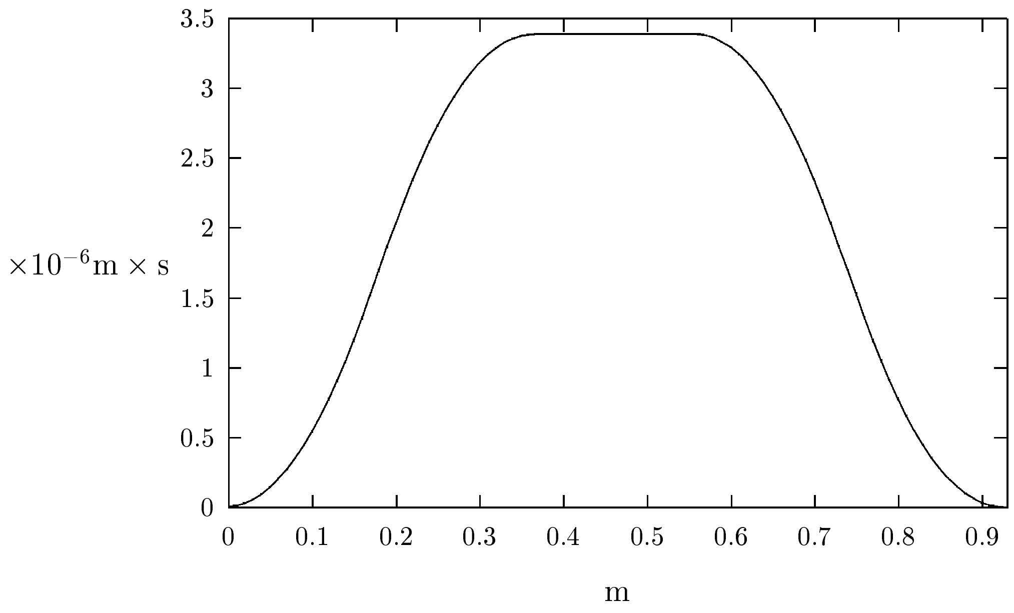

Figure 5.11: The column weighting function $W_{12}^c(y)$ for column #12. ($N = 20$, $\alpha = 10°$, $\varphi = 40°$, $p = 0.2$ m and $v = 800$ m s^{-1}).

Changing the variable $y \to y - (j-1)p\sin\alpha - (k-1)\Delta$ yields

$$s_{kj} = \int_{-\infty}^{+\infty} I(y - y_0) W_j^c(y - (j-1)p\sin\alpha - (k-1)\Delta)dy. \tag{5.25}$$

Thus the $(k,j)^{\text{th}}$ output of the camera is the discrete convolution of I with the properly shifted column weighting function. From (Eq. 5.23) we can see that $\alpha \neq 0$ results in broadening $W_j^c(y)$ by $\Delta - p\cos\alpha$ for every tracking step. It means that there is a practical limit $N_{\max}$ in tracking steps (5.18). Since the width of W is about $2p$ depending on α and φ, we define the practical maximum of N such that

$$N_{\max}(\Delta - p\cos\alpha) \leq 2p. \tag{5.26}$$

Substituting (Eq. 5.16) for Δ gives

$$N_{\max} \leq \frac{2\cos\varphi}{|\sin\varphi\sin\alpha|}. \tag{5.27}$$

5.5.3 On-Chip Binning

On-chip binning is a way to increase the signal output and dynamic range of the CCD at the expense of spatial resolution by shifting more than one row into the serial register (vertical binning) and/or into the summing node of the output amplifier (horizontal binning) before the read-out occurs. On-chip binning is useful for low light-level applications because it increases the SNR.

After a V fold vertical and H ($N/H \equiv L \in \mathbf{N}^{+}$) fold horizontal binning the $(m,n)^{\text{th}}$ pixel in the output image ($m = 1, 2, \ldots\ n = 1, 2, \ldots, L$) is

$$O_{mn} = \sum_{j=(n-1)H+1}^{nH} \sum_{k=(m-1)V+1}^{mV} \int_{-\infty}^{+\infty} I(y-y_0) W_j^c(y-(j-1)p\sin\alpha-(k-1)\Delta)dy. \tag{5.28}$$

Changing the order of summations and integration yields

$$O_{mn} = \int_{-\infty}^{+\infty} I(y-y_0) \sum_{j=(n-1)H+1}^{nH} \sum_{k=(m-1)V+1}^{mV} W_j^c(y-(j-1)p\sin\alpha-(k-1)\Delta)dy. \tag{5.29}$$

We can introduce the array weighting function such that

$$W_{mn}^a(y) \equiv \sum_{j=(n-1)H+1}^{nH} \sum_{k=(m-1)V+1}^{mV} W_j^c(y-(j-1)p\sin\alpha-(k-1)\,\Delta) \tag{5.30}$$

and then

$$O_{mn} = \int_{-\infty}^{+\infty} I(y-y_0) W_{mn}^a(y)\,dy. \tag{5.31}$$

Thus the $(m,n)^{\text{th}}$ output can be obtained by integrating the product of I and the array weighting function. Substituting (Eq. 5.23) into (Eq. 5.30) yields

$$\begin{aligned} W_{mn}^a(y) \equiv \textstyle\sum_{j=(n-1)H+1}^{nH} \displaystyle\sum_{k=(m-1)V+1}^{mV} \textstyle\sum_{i=1}^{N} T_{ij} W(y-(i-1)(\Delta-p\cos\alpha)-\\ (j-1)p\sin\alpha-(k-1)\,\Delta). \end{aligned} \tag{5.32}$$

5.5.4 The Output Image

We compute the response of a TDI camera for a set of equally spaced line images (a comb function input) in order to learn how the sampling and alignment error affects the output image.

Let I be

$$I(y-y_0) \equiv \delta(y-y_0-lY),\ l=0,1,2,\dots, \tag{5.33}$$

a periodic function with period Y. Substituting (5.33) into (5.31) we get

$$O_{mn} \equiv \sum_{j=(n-1)H+1}^{nH} \sum_{k=(m-1)V+1}^{mV} \sum_{i=1}^{N} T_{ij} W(y_0+y_1-(i-1)(\Delta-p\cos\alpha)- \\ (j-1)p\sin\alpha-(k-1)\,\Delta). \tag{5.34}$$

For the sake of simplicity, let us assume that $T_{ij} \equiv 1$ and that there is not binning ($V=H=1$), so that

$$O_{mn} = \sum_{i=1}^{N} W(y_0+lY-(i-1)(\Delta-p\cos\alpha)-(n-1)p\sin\alpha-(m-1)\,\Delta). \tag{5.35}$$

O_{mn} is also a periodic function naturally. In order to compute its period, let us take only one column (n). The period of O_{mn} is found by solving the equation

$$\arg(W_{l,i,n,m}) \text{ at the } l^{\text{th}} \text{ line image} = \arg(W_{l+1,i,n,m'}) \text{ at the } (l+1)^{\text{th}} \text{ line image} \tag{5.36}$$

for $m'-m$, i.e.,

$$lY-(m-1)\,\Delta = (l+1)Y-(m'-1)\,\Delta. \tag{5.37}$$

The period in the image with no alignment error ($\alpha=0$) is Y/p. With $\alpha \neq 0$ the period is Y/Δ, as can be seen after rearranging (5.37) such that

$$(m'-m)\Delta = Y. \tag{5.38}$$

Since $m' - m$ is independent of m, an alignment error rescales the output uniformly.

Now, take only a single line image from the input (5.33) and investigate the output for this line image. Let (m, n) be a pixel in the output of that particular line image. Then those (m', n') pixels in the output where the signal level is the same as at (m, n) can be found from

$$\arg(W_{l,i,n,m}) = \arg(W_{l,i,n',m'}), \tag{5.39}$$

i.e.,

$$(n-1)p \sin\alpha + (m-1)\Delta = (n'-1)p \sin\alpha + (m'-1)\Delta. \tag{5.40}$$

This is the equation of a line

$$-\frac{p \sin\alpha}{\Delta}(n' - n) = (m' - m) \tag{5.41}$$

with slope

$$\text{slope} = -\frac{p \sin\alpha}{\Delta} = \frac{\tan\alpha}{\tan\varphi \tan\alpha - 1}. \tag{5.42}$$

Therefore, the image of a line input is also a line that is inclined to the rows of the CCD by an angle of $\vartheta = \arctan(\text{slope})$. Since the scaling is uniform in the output image, the output for the comb function input is a set of uniformly spaced lines with slope (Eq. 5.42). In that particular case, when the denominator $\tan\varphi \tan\alpha - 1$ is zero, the limb shifts parallel to the motion of the Moon and occultation does not occur. The only task left is to investigate the profile[8] of an output line image. The output (Eq. 5.35) is a set of column weighting functions shifted according to (n, m). The column weighting function from (Eq. 5.23) is

$$W_j^c(y) = \sum_{i=1}^{N} T_{ij} W(y - (i-1)(\Delta - p\cos\alpha)). \tag{5.43}$$

[8]The impulse response function.

At perfect alignment $W_j^c(y)$ has a triangular shape with base $2p$ and height

$$p\tau \sum_{i=1}^{N} T_{ij}. \tag{5.44}$$

In this optimal case, the pixel values could be added together along the rows without affecting the spatial resolution that is proportional to $2p$. The maximum of the weighting function was increased to

$$p\tau \sum_{j=1}^{N} \sum_{i=1}^{N} T_{ij} \simeq p\tau N^2 \pi/4 = D^2 \pi/4 v_c. \tag{5.45}$$

When $\alpha \neq 0$ the light spreads over more pixels; therefore, both the angular resolution and the efficiency decrease.

Sampling the moving diffraction pattern with a TDI camera transforms the continuous irradiance distribution $I(y)$ into a discrete set of data O_{mn}. The finite size of pixels can be taken into account by introducing a weighting function W and then O_{mn} is obtained by the discrete convolution of I and W. An alignment error α rotates and uniformly rescales the output and also causes blurring because of the loss of synchronization. The aperture function T results in a modulation along the fringes.

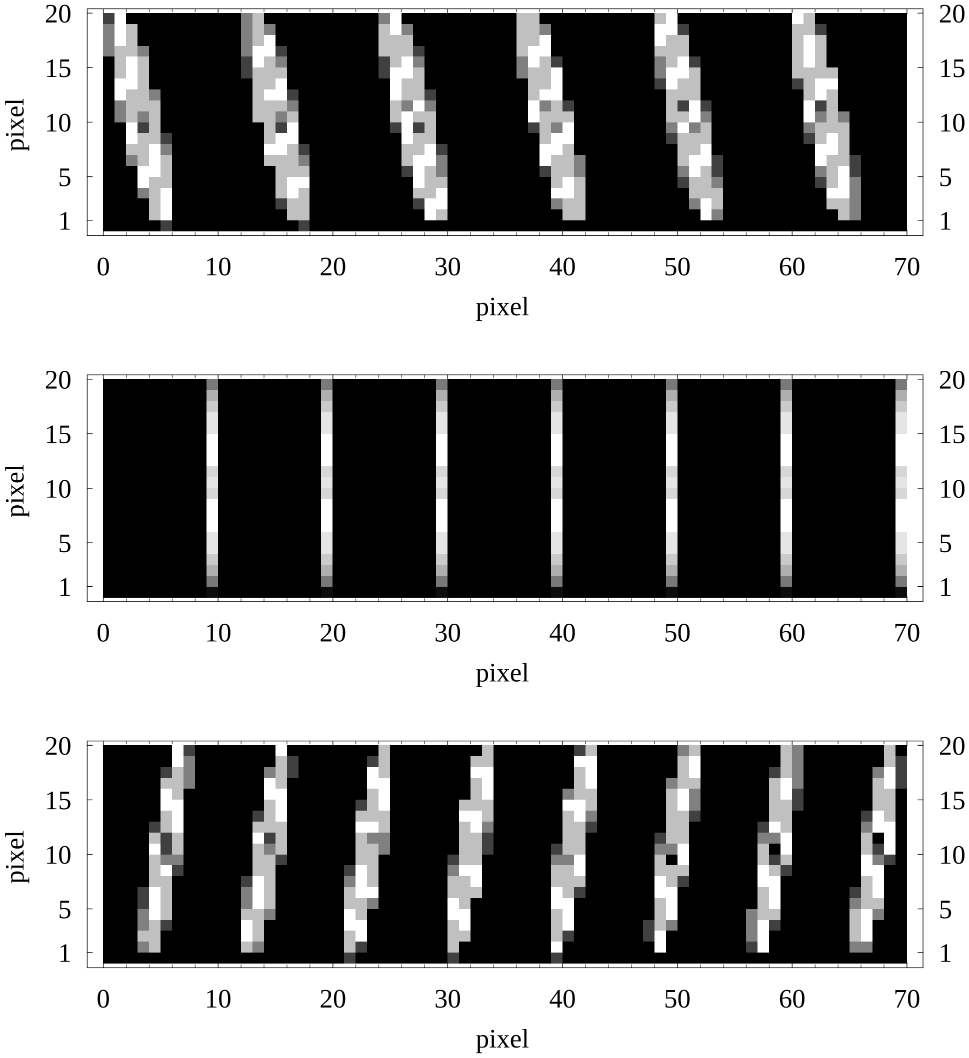

Figure 5.12: The output of a TDI camera for a comb function input when $\alpha = 10°$ (top), $\alpha = 0°$ (middle), $\alpha = -10°$ (bottom) and $\varphi = 40°$, (19×19 CCD)

CHAPTER VI

COMPUTER SIMULATIONS

The read-out rate of the HPC-1 camera at Dyer Observatory is not fast enough to permit me to conduct real TDI LO observations (see 9.1). Therefore, I have written a set of computer programs to simulate TDI LO observations under a wide variety of observational conditions. Great care has been taken to simulate all important aspects of real observations. However, as in all simulations, simplifications are unavoidable.

The programs can be divided into the following three groups:

- the **generator** program, whose output is the normalized theoretical light curve of an extended astrophysical object that is occulted by a straight edge,
- the **observer** program, which scales the normalized light curve according to the brightness of the object, corrupts the data with noise, simulates the operation of a TDI camera, and produces the "real" light curve,
- the **reducer** program, which extracts astrophysical information from the "real" light curve.

6.1 The Generator

The purpose of the generator program is to build the polychromatic diffraction pattern of an arbitrary extended object. In order to reduce this very complicated process to something tractable, I have adopted the model (see Chapter III) that the theoretical diffraction pattern on the ground results from Fresnel diffraction on an infinite straight edge –representing the lunar limb– perpendicular to the line of sight. This greatly simplifies the problem since the irradiance in the diffraction pattern can be described by a one-dimensional function $f(y)$, where y is measured in the direction perpendicular to the lunar limb.

Let the angular distribution of the monochromatic radiant flux of an extended object at wavelength λ be $I_a(\xi, \eta, \lambda)$. We can convert the angular scale to a linear scale in the pupil plane of a telescope by the formulae

$$x \equiv \xi d_{moon} \ , \quad y \equiv \eta d_{moon} \tag{6.1}$$

$$I_a(\xi, \eta, \lambda) = I_a(\frac{x}{d_{moon}}, \frac{y}{d_{moon}}, \lambda) \equiv I(x, y, \lambda), \tag{6.2}$$

where d_{moon} is the distance to the Moon. Let $F_{\lambda_0}(y)$ be the Fresnel diffraction pattern in the pupil plane at wavelength λ_0 due to the infinite straight edge. The transformation of the pattern to another λ can be carried out by

$$F_\lambda(y) = F_{\lambda_0}\left(y\sqrt{\frac{\lambda_0}{\lambda}}\right). \tag{6.3}$$

The infinitesimal element $dx'dy'$ at (x', y') of the object produces a diffraction pattern

$$I(x', y', \lambda)F_\lambda(y - y')dx'dy' = I(x', y', \lambda)F_{\lambda_0}\left((y - y')\sqrt{\frac{\lambda_0}{\lambda}}\right)dx'dy' \tag{6.4}$$

on the ground at wavelength λ. If the relative spectral sensitivity[1] of the measurement is $S(\lambda)$, then the polychromatic diffraction pattern due to this point is

$$dx'dy' \int_{\lambda_1}^{\lambda_2} I(x', y', \lambda)F_{\lambda_0}\left((y - y')\sqrt{\frac{\lambda_0}{\lambda}}\right)S(\lambda)d\lambda. \tag{6.5}$$

[1] $S(\lambda) = A(\lambda)T(\lambda)Q(\lambda)$, where $A(\lambda)$ is the relative spectral transmission of the atmosphere, $T(\lambda)$ is the net relative transmission of all optical elements involved in measuring system, and $Q(\lambda)$ is the quantum efficiency of the detector.
$S(\lambda)$ is normalized such that

$$\int_{\lambda_1}^{\lambda_2} S(\lambda)d\lambda = 1.$$

The overwhelming majority of astronomical objects radiate incoherently. Therefore, an extended object can be regarded as a large set of independently radiating point sources. Thus, the diffraction pattern of an extended object can be computed by dividing the object into a set of point sources and superimposing the diffraction patterns of the individual points sources. In our model the diffraction occurs on an infinite straight edge parallel to x; therefore, all points with the same y' coordinate produce the same pattern. Thus the net diffraction pattern due to all points with the same y' is

$$dy' \int_{-\infty}^{+\infty} \int_{\lambda_1}^{\lambda_2} I(x', y', \lambda) F_{\lambda_0} \left((y - y') \sqrt{\frac{\lambda_0}{\lambda}} \right) S(\lambda) d\lambda dx'. \tag{6.6}$$

The contribution of all points at different y' to the diffraction pattern is taken into account by integrating (Eq. 6.6) over y' and thus the polychromatic diffraction pattern of the extended object is

$$f(y) = \int_{-\infty}^{+\infty} \int_{-\infty}^{+\infty} \int_{\lambda_1}^{\lambda_2} I(x', y', \lambda) F_{\lambda_0} \left((y - y') \sqrt{\frac{\lambda_0}{\lambda}} \right) S(\lambda) d\lambda dx' dy'. \tag{6.7}$$

Changing the order of integrations and introducing $J(y', \lambda)$ as the one dimensional intensity distribution of the object

$$J(y', \lambda) \equiv \int_{-\infty}^{+\infty} I(x', y', \lambda) dx' \tag{6.8}$$

leads to

$$f(y) = \int_{-\infty}^{+\infty} \int_{\lambda_1}^{\lambda_2} J(y', \lambda) F_{\lambda_0} \left((y - y') \sqrt{\frac{\lambda_0}{\lambda}} \right) S(\lambda) d\lambda dy'. \tag{6.9}$$

If the spectral band of the observation is sufficiently narrow, we can assume that

$$J(y', \lambda) \simeq J(y'), \tag{6.10}$$

i.e., the one-dimensional intensity profile $J(y')$ of the object is independent of wavelength. Thus, if the spectral band of the observations does not include strong lines,

$J(y', \lambda)$ can be taken out from the inner integral in (6.9) and

$$f(y) = \int_{-\infty}^{+\infty} J(y') \int_{\lambda_1}^{\lambda_2} F_{\lambda_0}\left((y - y')\sqrt{\frac{\lambda_0}{\lambda}}\right) S(\lambda) d\lambda\, dy'. \tag{6.11}$$

Let $F(y)$ be the normalized polychromatic diffraction pattern of a point source through the system characterized by $S(\lambda)$

$$F(y) = \int_{\lambda_1}^{\lambda_2} F_{\lambda_0}\left(y\sqrt{\frac{\lambda_0}{\lambda}}\right) S(\lambda) d\lambda. \tag{6.12}$$

Then $f(y)$ can be expressed as a convolution integral

$$f(y) = \int_{-\infty}^{+\infty} J(y')\, F(y - y') dy'. \tag{6.13}$$

Computation of $f(y)$ is quite straightforward. $J(y)$ is computed first from $I(x, y, \lambda)$ by assuming (6.10). $F_{\lambda_0}\left(y\sqrt{\frac{\lambda_0}{\lambda}}\right)$ is computed and tabulated at $\lambda_0 = 600$ nm in steps of $\Delta y = 0.01$ m. The shape of $S(\lambda)$ is dominated by the transmission profile of a narrow interference filter because the spectral characteristics of the atmosphere and other optical elements in the system are flat in the $400 - 900$ nm range over which the CCD is sensitive. The transmission profile of a narrow interference filter can be approximated by a Gaussian function, therefore, $S(\lambda)$ was assumed to be Gaussian too. With the assumed $S(\lambda)$, $F(y)$ is computed from (Eq. 6.12). Finally, the numerical convolution (Eq. 6.13) of $F(y)$ and $J(y)$ provides $f(y)$. Note that $f(y)$ is normalized that $\lim_{y\to\infty} f(y) = 1$ and $\lim_{y\to-\infty} f(y) = 0$.

As an illustration we provide a model double star system (Fig. 6.1) where the angular vector separation of the components is 16 mas, the individual angular sizes are $\phi_1 = 2$ mas and $\phi_2 = 4.2$ mas and the luminosity ratio in the $\Delta\lambda = 10$ nm wide observational band is $L_1/L_2 = 40$. The one-dimensional intensity distribution perpendicular to the lunar limb is shown on Fig. 6.2 and the polychromatic one-dimensional diffraction pattern is shown on Fig. 6.3.

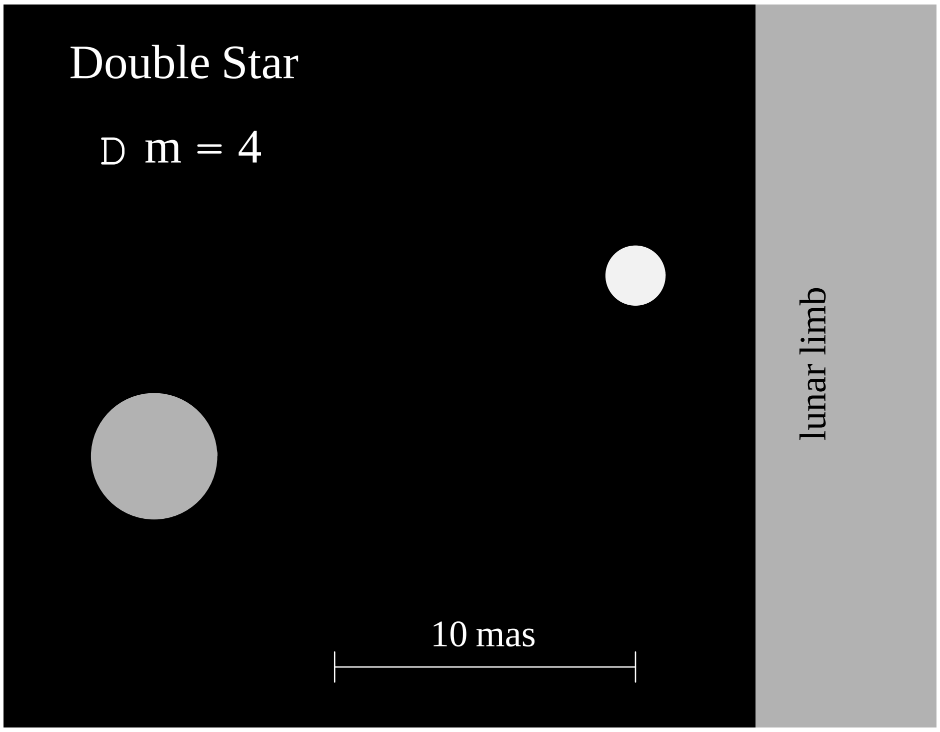

Figure 6.1: A model double star system $R_1/R_2 = 2.2$ and $\Delta m = 4$.

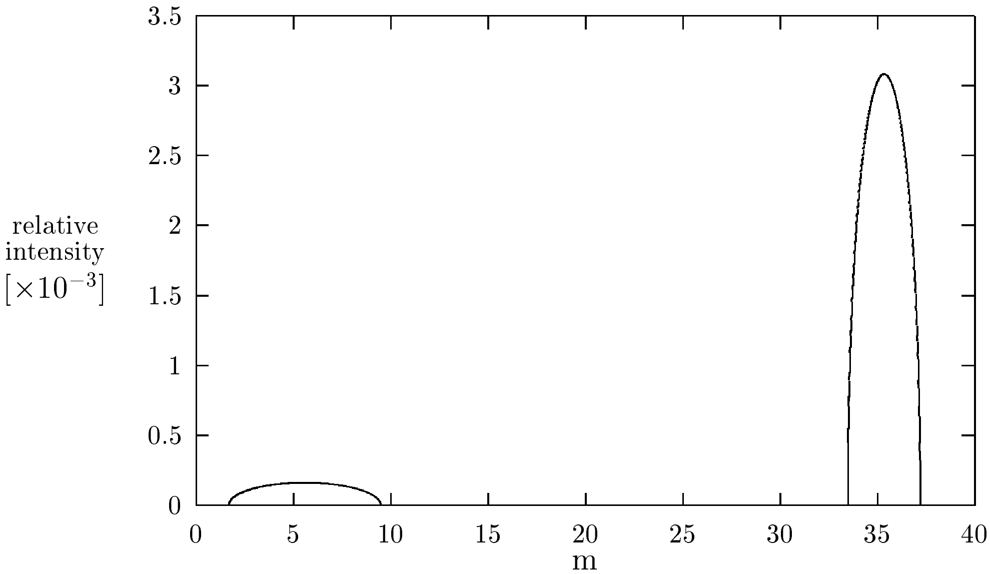

Figure 6.2: The 1-D intensity profile of the binary system in direction perpendicular to the lunar limb

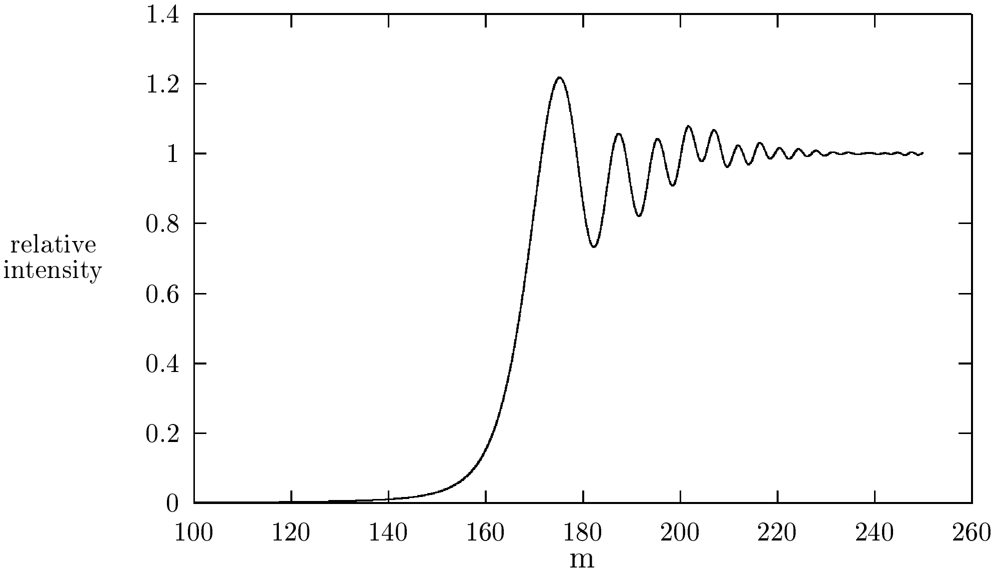

Figure 6.3: The 1-D polychromatic diffraction pattern of the model binary system. The bandwidth $\Delta\lambda$=10nm.

6.2 The Observer

The light from the occulted object is passed through a simulated atmosphere-telescope-detector system that introduces noise, has finite aperture, and requires finite integration time.

We have developed the following algorithm for TDI LO simulations: The CCD is treated as a rectangular array of $n \times n$ pixels. Every pixel is associated with a weighting function (see 5.5.1). We use the same weighting function for every pixel when $n > 8$ because most of the pixels (except around the perimeter of the illuminated area) are illuminated totally. However, when $n < 8$, we use an individual weighting function for every pixel. As the diffraction pattern passes over the telescope, the expected value of irradiance due to the star is computed for every pixel. The expected irradiance on each pixel varies in a perfectly predictive manner as the fringes move across the CCD. However, the irradiance itself is a random variable due to atmospheric turbulence. Representations of random irradiance are computed by generating an array A of $n \times n$ spatially correlated and log-normally distributed random variables. The mean of each random variable in A is set according to the expected irradiance in the diffraction pattern. The covariances between the random variables in A are computed by assuming a particular model for the strength of atmospheric turbulence $C_n^2(h)$ as a function of height h above the ground. The illumination on each pixel is increased by the sky background level, which is assumed to be uniform[2] with a constant mean, and the photon numbers are converted to electron numbers for every pixel. These random numbers represent the expected increments in electron numbers in the pixels during a single exposure, i.e., between two parallel shifts. The actual increments are computed by generating an array B of $n \times n$ random variables with a Poisson distribution (introducing shot noise). The mean value of each Poisson random variable in B is set so that $\overline{B}_{ij} = A_{ij}$. Array B is a representation of the actual increment in electron numbers in the pixels in a single exposure. Array B is added to an array C of $n \times n$ numbers which represent the total number of photo-electrons in each pixel at a given time. After each increment, C is shifted by one step down so that its n^{th} row goes into a buffer S of n elements while its first row is zeroed. S represents the serial shift register in the CCD. The pixels are read out from S one by one in such a way that each output is a Gaussian random variable (introducing read-out noise). The mean of the k^{th} output is S_k and the rms noise is R, the total read-out noise of the CCD. Then the diffraction pattern is shifted according to its speed and the time between two parallel shifts and the whole process is repeated with one exception. After every parallel step the array which is used to generate A is shifted correspondingly to the wind direction and speed. The shifted array is then

[2]The sky appears to be uniform looking through a $10''$ diaphragm.

completed with new random numbers and used to generate the next representation of A. This procedure results in a drifting random irradiance pattern in the pupil plane according to Taylor's hypothesis (see Section 6.2.2).

We discuss this algorithm in detail in rest of the chapter.

6.2.1 Scaling

The moving diffraction pattern in the pupil plane is described by a one-dimensional irradiance distribution $f(y - v_c t)$. f is given in a normalized form ($\lim_{y\to-\infty} f = 0$, $\lim_{y\to\infty} f = 1$) by the **generator** program and has to be scaled and offset according to the flux of the object and sky background, respectively. We use Behr's (1981) formula

$$\begin{aligned} \log W(\lambda, T) &= 2\log D - 0.4 m_V + \log \Delta\lambda - 15.51 - \\ &\quad 5\log\frac{\lambda}{5500} - \frac{6240}{T}\left(\frac{1}{\lambda} - 0.000182\right)10^4 \end{aligned} \tag{6.14}$$

that gives the measured radiant flux W (in Watts) from the source of apparent magnitude m_V and temperature T (in K), at wavelength λ (in Å) using bandwidth $\Delta\lambda$ (in Å) through an aperture of diameter D (in cm). Thus the average photon flux from a star as a function of m_V at effective temperature $T = 6000$ K, observed from above the atmosphere of Earth at $\lambda = 6000$ Å is

$$F_* = 1.1 \times 10^{7-0.4 m_V}\ [\text{photons m}^{-2}\text{s}^{-1}\text{Å}^{-1}]. \tag{6.15}$$

A fraction of the photons are lost due to atmospheric extinction and due to absorption and scattering in the telescope (mirrors, filters, etc.). Additionally, only a fraction of the incident photons are actually detected by the detector; consequently, the output of a detector due to the star alone through an aperture D in wavelength band $\Delta\lambda$ during an exposure τ is estimated as

$$I_* = qF_* \frac{D^2\pi}{4} \tau \Delta\lambda, \tag{6.16}$$

where $q < 1$ accounts for all photon losses. At $\lambda = 6000$ Å, the quantum efficiency of the CCD is assumed to be 0.56. We estimate the atmospheric and optical efficiency as 0.6 at this wavelength, which yields an overall efficiency of $q \simeq 0.34$. Since the telescope pupil is imaged onto $n \times n$ pixels, $D = np$ and $\tau = p/v_c$. Thus the expected increment in electron numbers per exposure p/v_c due to the star alone is

$$\frac{\pi}{4} qF_* \Delta\lambda \frac{n^2 p^3}{v_c}. \tag{6.17}$$

These electrons are distributed among $n^2\pi/4$ pixels on the CCD and the starlight is modulated by $f(y - v_c t)$. Therefore, the increment in electron numbers on pixel (i, j) per step is

$$qF_* \Delta\lambda \sum_j f_{ij} W_j \text{ [electrons]}, \tag{6.18}$$

where f_{ij} is the value of $f(y - v_c t)$ at pixel (i, j) and W_j is the pixel weighting function normalized in such a way that

$$\sum_j W_j = p^2 \frac{p}{v_c}. \tag{6.19}$$

The CCD also receives photons from the sky background through the diaphragm in the focal plane of the telescope. Let the diameter of the diaphragm be b arcsecs. Every square arcsec acts like a faint star that contributes to the illumination on the CCD and eventually to the total number of photo-electrons per step by an amount

$$qF_b \frac{D^2\pi}{4} \tau \Delta\lambda, \tag{6.20}$$

where F_b is the sky flux in photons m^{-2} arcsec^{-2} s^{-1} Å^{-1}. Since the Moon is a fairly red object and the sky background during LO observations is mostly due to the scattered light from the Moon (and from the Earth), we assume $T_{sky} = 4400$ K. If the sky brightness per square arcsec in the visual band is m_V^b then the sky flux from Behr's formula is

$$F_b = 1.4 \times 10^{7-0.4m_V^b} \text{ [photons m}^{-2}\text{arcsec}^{-1}\text{s}^{-1}\text{Å}^{-1}\text{]}. \tag{6.21}$$

There are $b^2\pi/4$ such faint stars visible in the diaphragm; thus, the increment in photo-electrons due to the sky background alone is estimated as

$$qF_b \frac{b^2\pi}{4} \frac{D^2\pi}{4} \tau \Delta\lambda. \tag{6.22}$$

Since the background is assumed to be uniform and the electrons are distributed among $n^2\pi/4$ pixels, the photo-electron increment due to the sky background is computed from

$$qF_b \Delta\lambda \frac{b^2\pi}{4} \frac{p^3}{v_c} \text{ [electrons]}. \tag{6.23}$$

Even with favorable scattering conditions, the sky background seen through a $10''$ diameter diaphragm centered on the mid-point of the dark limb at first or third quarter has been estimated to be equivalent to the flux from a fifth magnitude star (Africano & Montemayor, 1977). It then follows, that $m_V^b \approx 10$ per square arcsec and we adopt this value. Substituting $m_V^b = 10$ into (Eq. 6.21) and F_b into (Eq. 6.23) yields about 50 e^- per step at $\Delta\lambda = 10$ nm, $p = 0.2$ m, $v_c = 600$ m s^{-1}, $b = 10''$.

6.2.2 Simulation of Scintillation Noise

The optical effects of atmospheric turbulence arise from diffraction of light caused by turbulent eddies[3] that are swept across the propagation path by local winds. Turbulent velocity fluctuations in the air generate a statistical temperature field (on the order of 0.1-1 K), which in turn gives rise to random inhomogeneities in the index of refraction. The inhomogeneities are tiny but the cumulative effect of a large number of them is significant. The refractive index variations induce changes in the phase of starlight and these phase differences distort the wavefront, which leads to variations in the level of irradiance on the ground. The irradiance due to a star at the Earth's surface varies spatially and temporally, forming what is often referred to as a stellar shadow pattern (Fig. 6.4). The irregularly changing shadow pattern integrated over an aperture results in scintillation noise. Because the diffracted light of an occulted star passes through the turbulent atmosphere, a spatially and temporary random noise appears on LO diffraction patterns (Fig. 6.5) which interferes with TDI LO observations. The three-dimensional turbulence and the two-dimesional irradiance pattern on the ground require a statistical description. The literature of atmospheric turbulence and wave propagation through turbulent medium is very extensive. A number of monographs exist on wave propagation in random media: Tatarski (1961, 1971), Uscinski (1977), Ishimaru (1978), and Rytov *et al.* (1989). Beran & Oz-Vogt (1994) review the imaging through turbulence in the atmosphere (including analytical as well as numerical results). To reveal the irradiance distribution, numerical simulations can be made (Gozani 1985; Martin &

[3]Localized regions of constant index of refraction, ranging in size from an inner scale, l_0, on the order of millimeters, to an outer scale, L_0, on the order of kilometers.

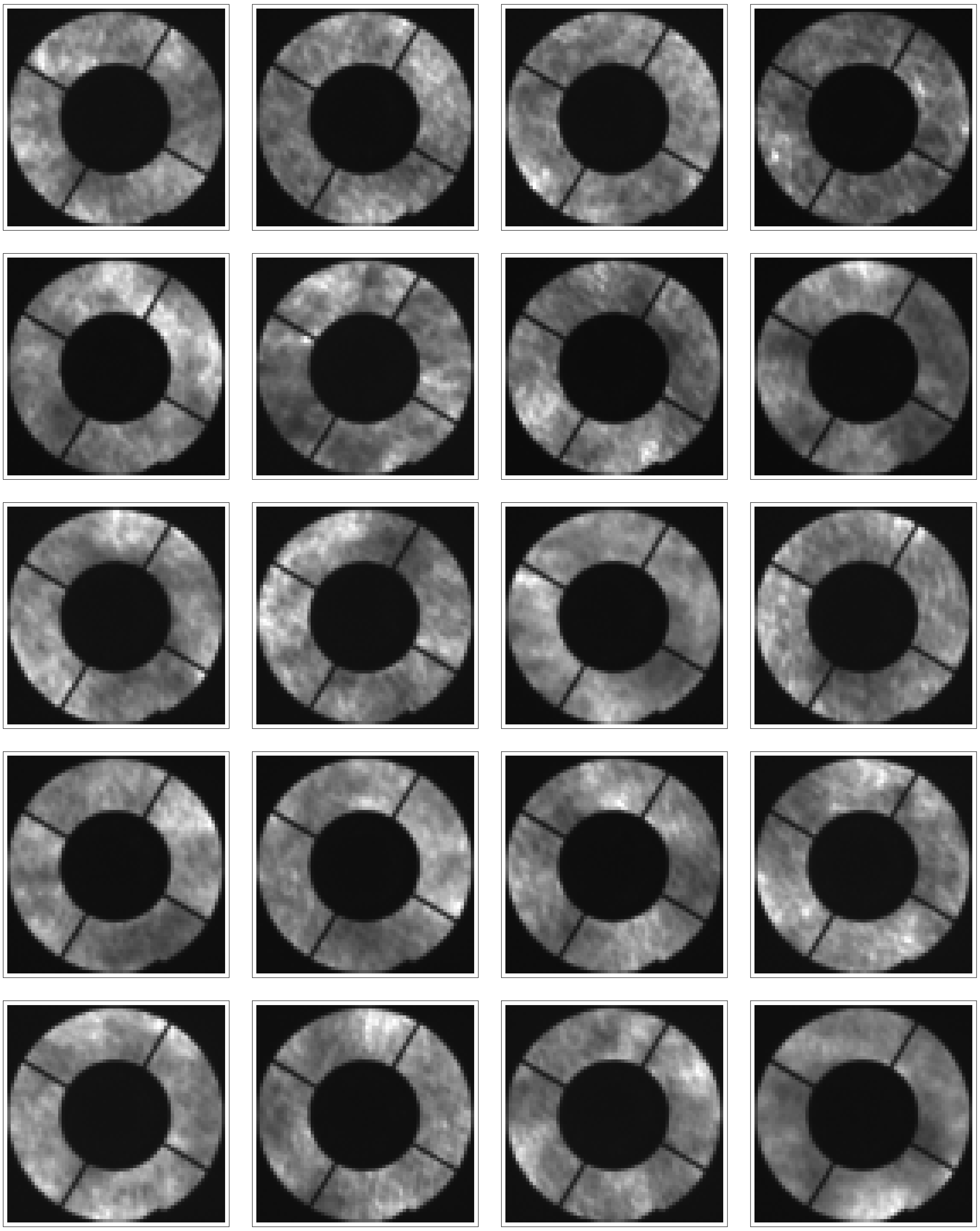

Figure 6.4: Shadow patterns of Sirius recorded in the pupil plane of the 24-inch Seyfert Telescope at Dyer Observatorty. No filter and $\tau_{exp} = 10$ ms.

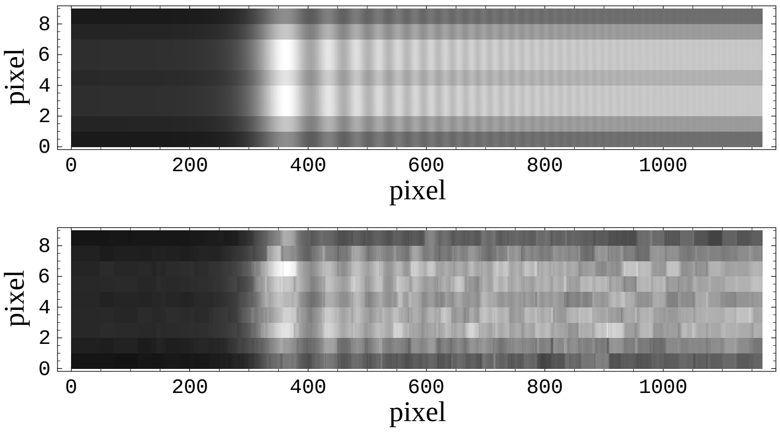

Figure 6.5: Scintillation on a simulated TDI observation. No scintillation (top), strong scintillation (bottom). The pictures are compressed horizontally.

Flatté, 1988; Flatté & Wang, 1993; Flatté *et al.* 1994). Here we do not go into the theory of atmospheric turbulence in detail. Instead, we give a qualitative picture following Dravins *et al.* (1996).

The modeling of shadow patterns often starts with the concept of a phase screen –a thin slab of turbulent air that deforms the smooth incident wavefront. The structure of the shadow pattern depends on the curvature of the wavefront, because it involves focusing and defocusing. Consider a plane wave passing through a phase screen. Irregular phase delays cause the emergent wavefront to become distorted. Each Fourier component of turbulence in the slab corresponds to a sinusoidal phase grating, from which the wavefront emerges with sinusoidal corrugations of spatial period d. We can analyze this wavefront in terms of the first order spectra diffracted by the grating since the corrugations are assumed to be small; therefore, only the first order diffracted waves have appreciable amplitudes. These diffracted waves interfere with the zero-order waves to give a sinusoidally modulated diffraction pattern, with the same period d. Near the phase screen, the first order waves are nearly in phase with the zero-order one, so the intensity modulation is small. Further away from the screen, the phase differences increase. Therefore, the modulation in the shadow pattern also increases, reaching maximum when the first order waves are a half-wave out of phase from the zero-order. At distance z from the screen we have $z^2 + d^2 \simeq (z + \lambda/2)^2$ or $d \simeq \sqrt{\lambda z}$. Thus, diffraction enhances intensity modulations on spatial scale $\sqrt{\lambda z}$, which is the Fresnel-zone size r_F. In particular, higher frequencies are filtered out by the diffraction. For a star near the zenith, r_F is on the order of $5 - 10$ cm. These wave optics effects are diminished for sufficiently short wavelengths, in the geometrical-optics regime, where the phase screen acts like a weak, wavy lens.

The refractive-index variations along a path of propagation modulate the intensity in a multiplicative manner (hence its logarithm in an additive manner), in the sense that if twice the intensity is transmitted, then twice the variation is observed. Therefore, the expected variation of log-intensity is the sum of many random perturbations induced at various places along the path of propagation. As a consequence of the central-limit theorem, if the number of perturbations is very large, the variations of log-intensity follow a normal distribution and the intensity follows a log-normal distribution. Therefore, the probability density of irradiance in the pupil plane is assumed to be

$$p(I) = \frac{1}{\sqrt{2\pi} b I} \exp\left\{ -\frac{(\ln \frac{I}{\bar{I}} - \frac{b^2}{2})^2}{2b^2} \right\}, \tag{6.24}$$

where $b = \sqrt{\ln(\sigma_{sc}^2 + 1)}$, depends on the strength of turbulence and $\sigma_{sc}^2 \equiv \sigma_I^2 / \bar{I}^2$ is the normalized irradiance variance or scintillation index (Fig. 6.6).

The normalized covariance function of irradiance $c(\rho)$ for weak ($\sigma_{sc}^2 < 0.1$) and

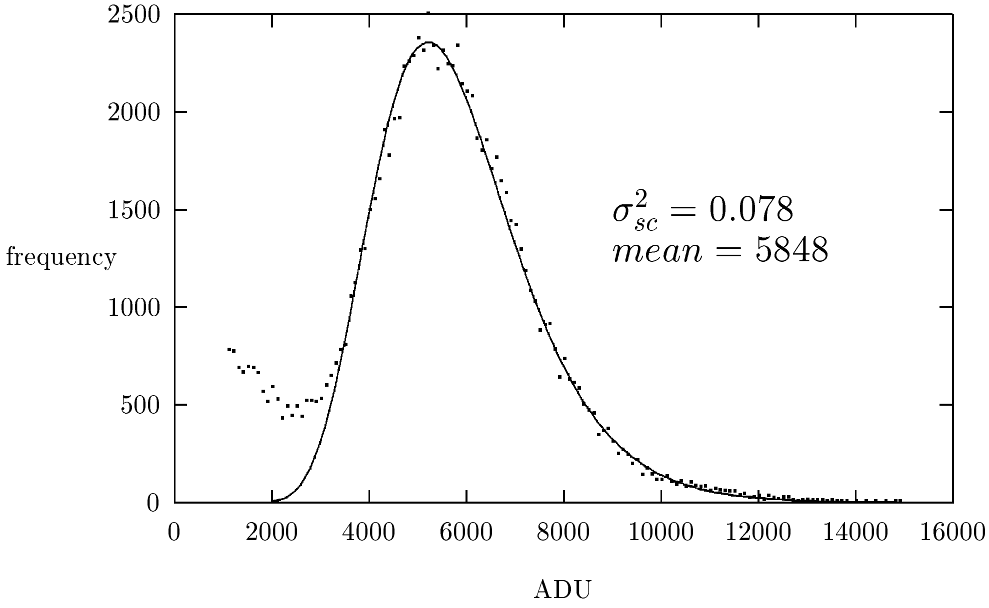

Figure 6.6: Frequencies determined from twenty 64×64 shadow patterns of Sirius. The data can be well approximated with log-normal distribution. The reason of the excess of dark pixels below ADU=3000 is that the only a fraction of the pixels in each 64×64 array are illuminated by the telescope pupil image.

isotropic turbulence is approximated by

$$c(\rho) = 5.21k^2 \int_0^\infty \int_0^\infty \kappa^{-8/3} J_0(\kappa\rho) \sin^2 \left[\frac{\kappa^2(L-z)}{2k}\right] C_n^2(L-z) dz d\kappa, \qquad (6.25)$$

where J_0 is the zero-order Bessel function of the first kind, κ is the spatial wave-number, $C_n^2(z)$ is the refractive-index structure coefficient[4], and k is the optical wave number (Churnside 1990). Letting $\rho = 0$ and introducing $h \equiv L - z$ and $w \equiv \kappa^2 h/2k$

[4]In the inertial subrange the power spectral density $\Phi_n(\kappa)$ associated with isotropic refractive-index fluctuations can be described by a power-law spectrum

$$\Phi_n(\kappa) = 0.033 C_n^2 \kappa^{-11/3},$$

first derived by Obukhov and Kolmogorov.

The value of C_n^2 depends on both local atmospheric conditions and height above the ground. Typical values near the ground vary from $C_n^2 = 10^{-13}$ m$^{-2/3}$ for strong turbulence to $C_n^2 = 10^{-17}$ m$^{-2/3}$ for weak turbulence. Results of measurements indicate that C_n^2 generally decreases by roughly two orders of magnitude as elevation increases from 500 m to 15 km above see level, but the dominant feature of the variation is the existence of many clearly defined layers where strong variations of the refractive index may occur. The dominant layers, which are often found at 2-5 km elevations and in the tropopause 10-12 km above sea level, are generally associated with temperature inversions. Radar measurements reveal that these layers can be less than a meter thick and may extend horizontally for several kilometers.

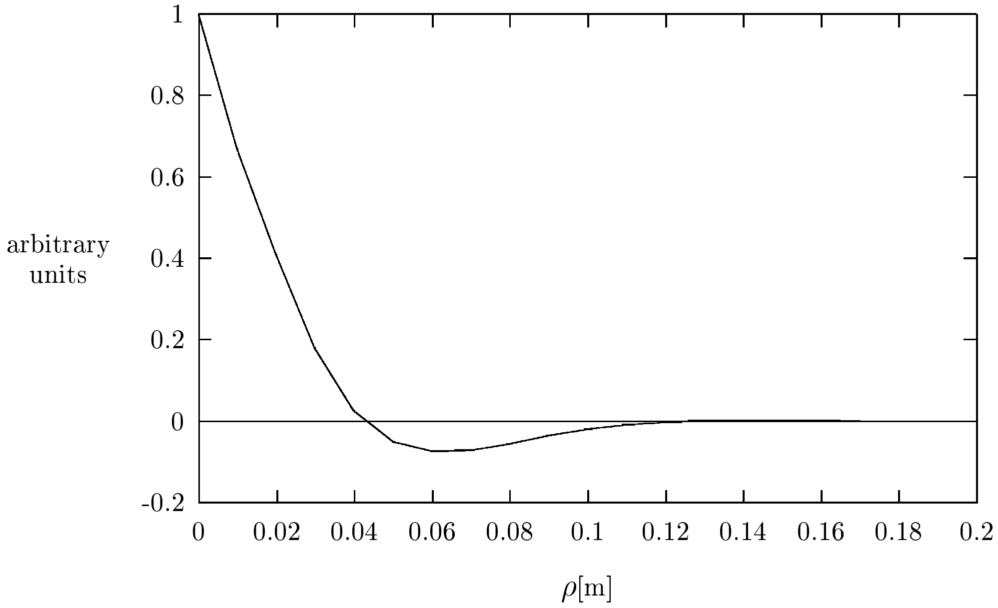

Figure 6.7: The normalized covariance function that was used during computer simulations.

into (Eq. 6.25) gives the scintillation index

$$\sigma_{sc}^2 = 1.46k^{7/6} \int_0^\infty h^{5/6} C_n^2(h) dh \int_0^\infty w^{-11/6} \sin^2 w \, dw \tag{6.26}$$

and, after integration over w, we obtain

$$\sigma_{sc}^2 = 2.25k^{7/6} \int_0^\infty h^{5/6} C_n^2(h) dh. \tag{6.27}$$

Hufnagel (1974) has taken the results of many different measurements of C_n^2 and produced an empirical model for the height dependence of C_n^2 . From a profile of C_n^2 one can compute the normalized covariance function (Eq. 6.25) (see Fig.6.7) and the scintillation index (Eq. 6.27).

The task of generating representations of a homogeneous and locally isotropic random irradiance field with given probability (Eq. 6.24) and normalized spatial covariance functions (Eq. 6.25) can be accomplished in two steps. First, we generate a two-dimensional standard Gaussian white-noise pattern and introduce spatial correlation. Second, we transform the spatially correlated Gaussian pattern to log-normal. The

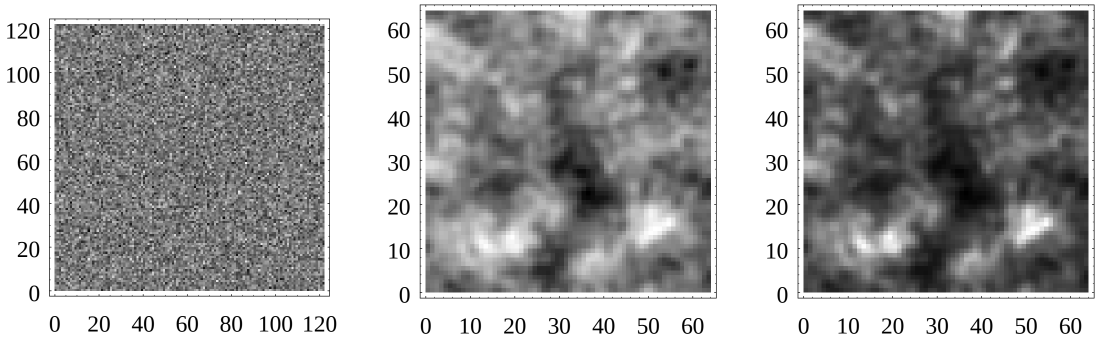

Figure 6.8: Standard Gaussian white noise (left), correlated Gaussian noise (middle) and log-normal noise (right).

spatial correlation is introduced by performing a convolution operation between the Gaussian white-noise pattern and a function computed from the required irradiance covariance function (Fig. 6.8). The convolution retains the Gaussian distribution but changes the mean and variance. We used the transformation

$$y = \frac{\bar{y}}{\sqrt{\sigma_0^2 + 1}} \exp\left[w\sqrt{\ln(\sigma_0^2 + 1)}\right] \tag{6.28}$$

to convert a standard Gaussian random variable w into a log-normal random variable y, where $\bar{y}$ and σ_0^2 are the required mean and normalized variance of y, respectively. By using this algorithm, we generated representations of the random irradiance distribution in the pupil plane (Fig. 6.9). At every point in the pupil plane, the mean irradiance was chosen according to the local star flux. Since there is no scintillation in the scattered background, the background flux was not taken into account. The random irradiance pattern evolves in time. The evolution time scale τ_0 is defined by $\overline{I(\mathbf{x},t)I(\mathbf{x},t+\tau)} \simeq \bar{I}^2$ if $\tau > \tau_0$, i.e., the irradiance at a point in the pupil plane is not correlated over a period of time much longer than τ_0. I have adopted the assumption, introduced by G. I. Taylor in 1938, of frozen turbulence i.e., the approximation that atmospheric structures evolve on time scales longer than those required for the wind

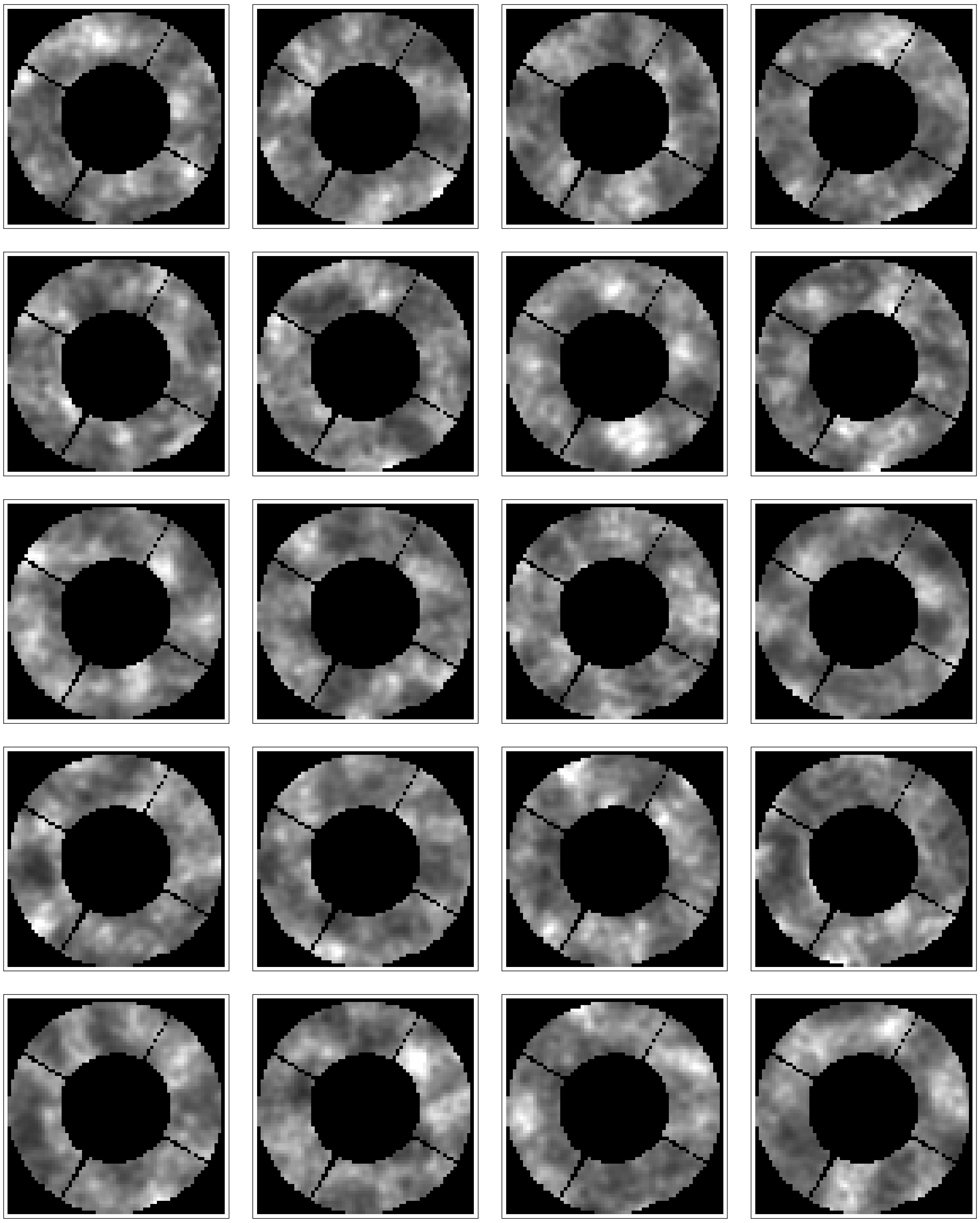

Figure 6.9: Simulated pupil images.

to blow the shadow pattern past the telescope. A wind uniform throughout the turbulence merely drives the irradiance pattern without deformation over the telescope pupil plane, i.e., the bulk velocity of the turbulent pattern is larger than the internal velocities. Focusing on one particular atmospheric layer, Taylor's hypothesis appears to be good approximation. However, Taylor's hypothesis refers to the turbulence and not necessarily to the shadow pattern, as pointed out Dravins *et al.* (1996). The atmosphere may contain many turbulent layers with different velocity vectors; each produces its own shadow pattern that could be relatively long-lived; but the sum of the patterns remains coherent only for the time it takes the wind shear to move the components a distance equal to their size. As differences in wind velocities between different heights may reach 10 m s^{-1} and the size of a shadow is $\simeq$ 10 cm (Fresnel-zone size), the expected lifetime is usually no more than about 10 ms.

Since the typical speed of the passing diffraction pattern is on the order of $600-700$ m s^{-1} and p is usually less than 1 m, the exposures between parallel shifts are in the order of 1 ms or less. Therefore, we have considered the irradiance pattern to be frozen (motionless) during integrations. The time evolution of irradiance is simulated in such a way that, after every shift in the parallel register, the random Gaussian white noise pattern was shifted according to the wind speed and direction. Then the shifted pattern was completed with new elements and the convolution and log-normal transformation were repeated (Fig. 6.10). This procedure resulted in a slowly drifting random irradiance distribution corresponding to Taylor's hypothesis.

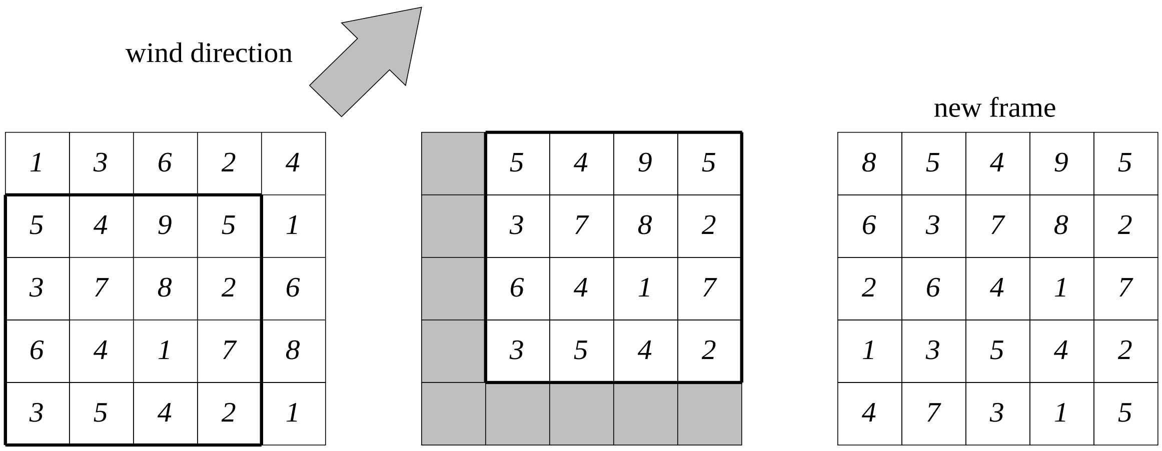

Figure 6.10: The Gaussian white-noise pattern is shifted according to the wind speed and direction. The pattern is completed with new elements and the convolution and log-normal transfomation is repeated.

6.2.3 Sampling

A CCD placed in the pupil plane of a telescope acts like an array of rectangular apertures that integrate the moving spatially correlated random irradiance field. Ideally, in order to simulate TDI on a 10 m telescope one needs a minimum of 64×64 pixels, because the smallest resolvable feature in the diffraction pattern is about $0.1 - 0.15$ m (Young 1971). This means that the computational mesh on which the random irradiance field is generated will contain about 640×640 points if every pixel is divided into 10×10 subpixels for numerical integration. If the diffraction pattern where resolvable features can be found were 150 m ($\simeq$ 1000 rows) in length, then one would need about a thousand frames of 640×640 points. This ideal approach was beyond the capabilities of my computer. Instead, as a computational simplification, I computed the probability density and normalized covariance functions of the stationary random irradiance pattern for the pixel array in advance before the actual simulation. This approach greatly simplifies the computations and results in a much faster program because during the simulation we need to deal with an array of 64×64

points at most instead of 640×640.

Aperture Averaging by Pixels

In the case of stationary[5] and isotropic turbulence, the spatial correlation function Γ of irradiance is independent of time and circularly symmetric, i.e., $\Gamma(\mathbf{x},\mathbf{y},t) = \Gamma(r)$, where $\mathbf{x}$ and $\mathbf{y}$ are two arbitrary points in the pupil plane and $r \equiv |\mathbf{x}-\mathbf{y}|$.

If the characteristic spatial coherence length r_0 (Fried 1966) in the irradiance is small compared to the pixel size, the pixels perform a spatial averaging operation on the irradiance, resulting in fluctuations of the collected power that are smaller than those that would be obtained from a point[6] detector. These fluctuations decrease with increasing pixel sizes. Following the formulation proposed by Tatarski (1961) and Fried (1966), an aperture averaging factor is defined as the ratio of the normalized variance of collected power and the normalized variance of irradiance. The averaging factor depends on the form and size of pixels and on the spatial covariance function of irradiance.

Let $I(\mathbf{x},t)$ be the quasi-monochromatic[7] irradiance distribution in the pupil plane. We assume that $I(\mathbf{x},t)$ is a homogeneous, stationary, and isotropic random process with mean $\bar{I}$ and variance σ_I^2. The power and average power on a pixel (p) is

$$P = \int_{(p)} I(\mathbf{x},t)\, dA \tag{6.29}$$

and

$$\overline{P} = \overline{\int_{(p)} I(\mathbf{x},t)\, dA} = \overline{I(\mathbf{x},t)} \int_{(p)} dA = \overline{I} \int_{(p)} dA, \tag{6.30}$$

[5]The turbulence is assumed to be stationary during the short duration of an LO observation.
[6]A point detector has a characteristic diameter much smaller than the spatial correlation length.
[7]Integrated over the narrow (50-100 Å) bandwidth of observation.

respectively, since $I(\mathbf{x},t)$ is homogeneous. The $\overline{P^2}$ we need to compute the variance of P is given by

$$
\begin{aligned}
\overline{P^2} &= \overline{\left(\int\limits_{(p)} I(\mathbf{x},t)\,dA\right)^2} \\
&= \overline{\int\limits_{(p)} I(\mathbf{x},t)\,dA \int\limits_{(p)} I(\mathbf{x}',t)\,dA'} \\
&= \overline{\int\limits_{(p)}\int\limits_{(p)} I(\mathbf{x},t)I(\mathbf{x}',t)\,dA\,dA'} \\
&= \int\limits_{(p)}\int\limits_{(p)} \overline{I(\mathbf{x},t)I(\mathbf{x}',t)}\,dAdA' \\
&= \int\limits_{(p)}\int\limits_{(p)} \Gamma(\mathbf{x}-\mathbf{x}')\,dAdA' \\
&= \int\limits_{(p)}\int\limits_{(p)} \Gamma(r)\,dAdA',
\end{aligned} \tag{6.31}
$$

where dA and dA' are area elements on the same pixel. At the last two steps we exploited the assumption that $I(\mathbf{x},t)$ results from a homogeneous and isotropic random process; thereby, we can substitute $\Gamma(\mathbf{x}-\mathbf{x}')$ for $\overline{I(\mathbf{x},t)I(\mathbf{x}',t)}$ and $\Gamma(r)$ for $\Gamma(\mathbf{x}-\mathbf{x}')$.

Substituting for $\Gamma(r) = \sigma_I^2 c(r/r_0) + \bar{I}^2$, where $\sigma_I^2 c(r/r_0)$ is the autocovariance of $I(\mathbf{x},t)$,

$$
\overline{P^2} = \sigma_I^2 \int\limits_{(p)}\int\limits_{(p)} c(r/r_0)\,dAdA' + \underbrace{\bar{I}^2 \int\limits_{(p)}\int\limits_{(p)} dAdA'}_{\overline{P}^2} \tag{6.32}
$$

and

$$
\sigma_P^2 = \overline{P^2} - \overline{P}^2 = \sigma_I^2 \int\limits_{(p)}\int\limits_{(p)} c(r/r_0)\,dAdA'. \tag{6.33}
$$

By introducing the normalized variance of the collected power such as $\sigma_p^2 = \sigma_P^2/\bar{P}^2$ and recalling the scintillation index σ_{sc}^2, we found that the variance of the power on a pixel is

$$\sigma_p^2 = c_{00}\,\sigma_{sc}^2, \tag{6.34}$$

where

$$c_{00} = \frac{\int\limits_{(p)}\int\limits_{(p)} c(r/r_0)dAdA'}{\int\limits_{(p)}\int\limits_{(p)} dAdA'}. \tag{6.35}$$

$c_{00} \in (0,1)$ characterizes the efficiency of pixels to average the irradiance fluctuations. c_{00} is a function of only p/r_0. If p is large compared to r_0, then $c_{00} \ll 1$; consequently, $\sigma_p^2 \ll \sigma_{sc}^2$, i.e., the pixels effectively filter the irradiance fluctuations. When p is comparable to or less than r_0, the averaging effect is minor and the collected power has essentially the same variance as the irradiance the optical range of the spectrum and varies as $\lambda^{6/5}$ with wavelength.

If $r_0 \simeq p$, the power fluctuations on adjacent pixels are strongly correlated. The degree of covariance between two pixels is computed from

$$c_{ij} = \frac{\int\limits_{(p_i)}\int\limits_{(p_j)} c(r/r_0)\,dAdA'}{\int\limits_{(p_i)}\int\limits_{(p_j)} dAdA'}, \tag{6.36}$$

where p_i and p_j are two arbitrary pixels in the array (Fig. 6.11).

The procedure can be summarized as followes: from a C_n^2 profile I compute $c(r)$ with (Eq. 6.25) and σ_{sc}^2 from (Eq. 6.27), and c_{ij} from (Eq. 6.36). With c_{ij} in hand, the function W_{ij} is computed by solving the equation

$$\sum_k \sum_l W_{kl} W_{k-i,l-j} = c_{ij} \tag{6.37}$$

numerically. These calculations are all done before an actual simulation starts. Then W_{ij} is used in the simulation program to generate random irradiance fields.

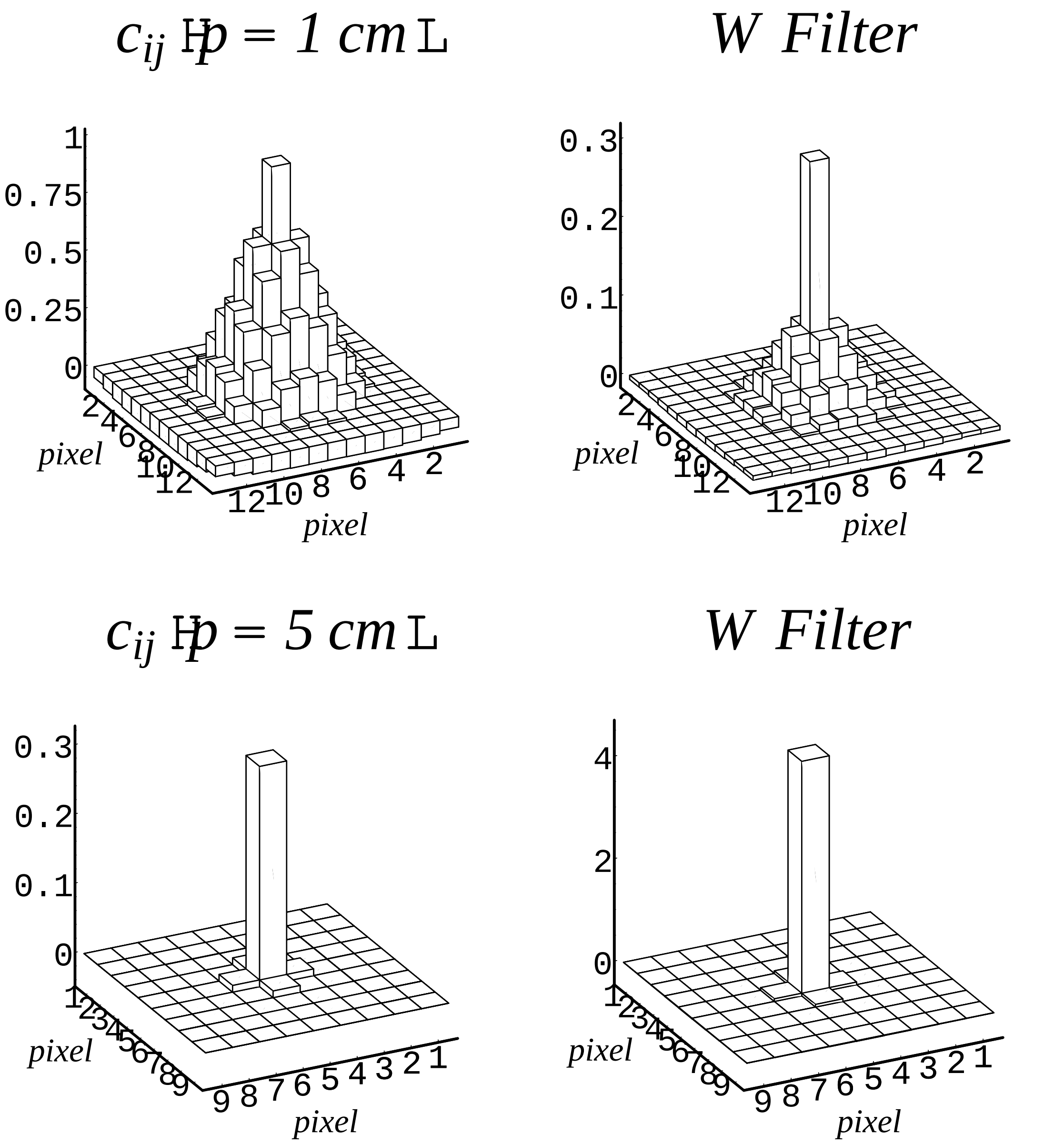

Figure 6.11: Covariance coefficients c_{ij} and the corresponding W filters. The convolution of the standard Gaussian noise with the W filter introduces spatial correlation between pixels.

Statistics of Photoelectron Numbers in CCD Pixels

While scintillation can be negligible during times of exceptionally good atmospheric conditions and detector noise can be reduced further with improved design and manufacturing of CCDs, shot noise is unavoidable.

Under the assumption that a photon is equally likely to arrive at a photon detector at any time, the number n of photo-electrons at the output of the detector is a Poisson random variable with mean $q\overline{m}$, where q is the quantum efficiency of the detector and $\overline{m}$ is the average photon flux. The probability density function of n is

$$p_n(n) = \frac{(q\overline{m})^n}{n!} e^{-q\overline{m}}. \tag{6.38}$$

The atmospheric turbulence generates a spatially and temporally correlated random irradiance field in the aperture plane of a telescope. It is known from observations that the irradiance m can be approximated by log-normal statistics with the density function

$$p_m(m) = \frac{1}{\sqrt{2\pi} bm} \exp\left\{ -\frac{(\ln \frac{m}{\overline{m}} - \frac{b^2}{2})^2}{2b^2} \right\}, \tag{6.39}$$

where $b = \sqrt{\ln(\sigma_{sc}^2 + 1)}$ and $\sigma_{sc}^2 = \sigma_m^2 / \overline{m}^2$ is the normalized irradiance variance or scintillation index. Let the instantaneous photon flux on a point detector in the pupil plane of a telescope be m. The diameter of this point detector should be small compared to the spatial coherence length r_0 and is usually less than 1 cm. The probability of detecting n photoelectrons by a point detector is given by

$$p_n(m) = \sum_{m=0}^{\infty} \frac{(qm)^n}{n!} e^{-qm} p_m(m) \tag{6.40}$$

since the probability of flux m is $p_m(m)$. The mean value of n is

$$\bar{n} = \sum_{n=0}^{\infty} n p_n(m) = \sum_{m=0}^{\infty} e^{-qm} p_m(m) \sum_{n=1}^{\infty} \frac{(qm)^n}{(n-1)!}. \tag{6.41}$$

By changing $n \to n+1$, it is easy to recognize that the second sum is $qm\, e^{qm}$. Hence, the mean value of n is

$$\bar{n} = q \sum_{m=0}^{\infty} m\, p_m(m) = q\overline{m}. \tag{6.42}$$

The variance σ_n^2 in n can be computed in the following way:

$$\begin{aligned}
\overline{n^2} &= \sum_{n=0}^{\infty} n^2 p_n(m) = \sum_{m=0}^{\infty} e^{-qm} p_m(m) \sum_{n=1}^{\infty} n \frac{(qm)^n}{(n-1)!} \\
&= \sum_{m=0}^{\infty} e^{-qm} p_m(m) \sum_{n=0}^{\infty} (n+1) \frac{(qm)^n}{n!} qm \\
&= \sum_{m=0}^{\infty} e^{-qm} p_m(m)\, qm \left(\sum_{n=1}^{\infty} \frac{(qm)^n}{(n-1)!} + \sum_{n=0}^{\infty} \frac{(qm)^n}{n!} \right) \\
&= \sum_{m=0}^{\infty} e^{-qm} p_m(m)\, qm \left(qm \sum_{n=0}^{\infty} \frac{(qm)^n}{n!} + \sum_{n=0}^{\infty} \frac{(qm)^n}{n!} \right) \qquad (6.43) \\
&= \sum_{m=0}^{\infty} qm(qm+1) p_m(m) \\
&= q^2 \sum_{m=0}^{\infty} m^2 p_m(m) + q \sum_{m=0}^{\infty} m\, p_m(m) \\
&= q^2 \overline{m^2} + q\overline{m}, \qquad (6.44)
\end{aligned}$$

and

$$\begin{aligned}
\sigma_n^2 &= \overline{n^2} - \bar{n}^2 = q^2 (\overline{m^2} - \overline{m}^2) + q\overline{m} \\
&= q^2 \sigma_m^2 + q\overline{m}. \qquad (6.45)
\end{aligned}$$

By substituting the scintillation index we find

$$\sigma_n^2 = \sigma_{sc}^2 \bar{n}^2 + \bar{n}. \tag{6.46}$$

If the scintillation is negligible, i.e., $\sigma_{sc}^2 = 0$, the photo-electron number follows Poisson statistics, with $\sigma_n^2 = \bar{n}$. However, $\sigma_{sc}^2 \neq 0$, so the term $\sigma_{sc}^2 \bar{n}^2$ becomes dominant with increasing irradiance. This is why taking only the shot noise into account gives over optimistic results for bright stars.

We can modify (Eq. 6.46) by taking into account the finite size of pixels, with (Eq. 6.34), which yields

$$\sigma_n^2 = c_{00}\sigma_{sc}^2\bar{n}^2 + \bar{n}, \tag{6.47}$$

where $\overline{n}$ is now the mean electron number in a pixel after an exposure that is short compared to the atmospheric coherence time.

6.2.4 CCD Noise

There are many noise sources associated with CCD detectors (Janesick 1991, Holst 1996). These noise sources are not treated independently in our simulation. Instead, we present them as a single quantity in units of equivalent electrons at the detector output. We also assume that the contribution of the external read-out electronics to the noise is negligible compared to the detector noise. Since the detector noise results from a number of independent noise sources, we selected the simplest Gaussian noise model with rms noise specified by manufacturers. We usually used rms noise $R = 15$ e^- during our calculations. Our results are not sensitive to the actual value of R because the sky-noise is usually much stronger.

6.2.5 Simulation of Conventional LO Observations

We used a slightly modified version of the TDI simulator program for simulating conventional observations. The telescope aperture is divided into $n \times n$ pixels as in case of TDI but there is no synchronous charge transfer among pixels. The diffraction pattern is shifted in front of the telescope in steps and, after each step, the increment in photo-electrons in the pixels is added to a buffer called the counter. The aperture of the telescope is set by n and the integration time is set by the number of steps before reading out and resetting the counter. We used the same scintillation model.

6.3 The Reducer

The purpose of the reducer programs is to extract the maximum amount of astrophysically important information from the simulated LO light curves. The usual approach (Nather & McCants 1970) is model fitting. Usually five parameters are used: the brightness of the star; the brightness of the background; the time of the geometric occultation; the scale factor (speed) of the diffraction pattern; and if the SNR is sufficiently high, the angular diameter of the source assuming that it is either a uniformly illuminating circular disc or a fully limb-darkened disc. If there is evidence that the source is a binary, two, in some cases three additional parameters are used: the brightness of the companion; the angular separation between the two objects; and the angular diameter of the companion. In many cases the SNR is not high enough to obtain an accurate estimate for the angular size of the source and only an upper limit can be claimed. However, from occultation traces of large bright stars like Antares, even the one-dimensional intensity profile along the star can be extracted (Richichi & Lisi 1990).

We only wanted to demonstrate the difference between the conventional and TDI lunar occultation light curves and explore the new possibilities permitted by the higher SNR in TDI mode. Our reducer program searches for the minimum χ^2 in a five-parameter space.

6.4 Results of Computer Simulations

In order to demonstrate the potential of TDI we first simulated the observation of a $m_V = 6$, K5 III star. The expected angular diameter of such a star is $\phi \approx 2$ mas; therefore we used the generator program to comput the diffraction pattern of a uniform circular disc of diameter 2 mas at $\lambda = 600$ nm (Fig. 6.12). Then we

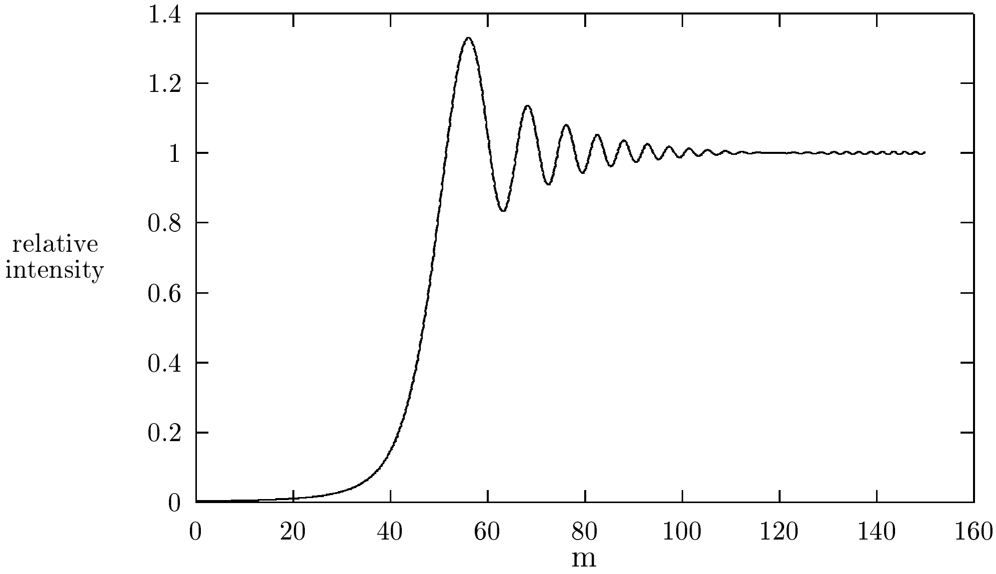

Figure 6.12: The straight-edge diffraction pattern of a uniformly illuminating disc of diameter $\phi = 2$ mas at $\lambda = 600$ nm, $\Delta\lambda = 20$ nm.

computed four light curves:

- conventional telescope (Fig. 6.13) ($D = 2.2$ m, integration time $\tau = 1.1$ ms, bandwidth $\Delta\lambda = 20$ nm, diaphragm $b = 10''$, efficiency $\kappa = 0.1$, $\sigma_{sc}^2 = 1.0$),
- TDI on the same telescope (Fig. 6.14) ($p = 0.2$ m, $n = 11$, $v = 700$ m s^{-1}, $\Delta\lambda = 20$ nm, $b = 10''$, efficiency $\kappa = 0.34$, no binning, $\alpha = \varphi = 0$, $\sigma_{sc}^2 = 1.0$),
- TDI on a 10 m telescope (Fig. 6.15) ($p = 0.2$ m, $n = 49$, all the other parameters are the same as above),

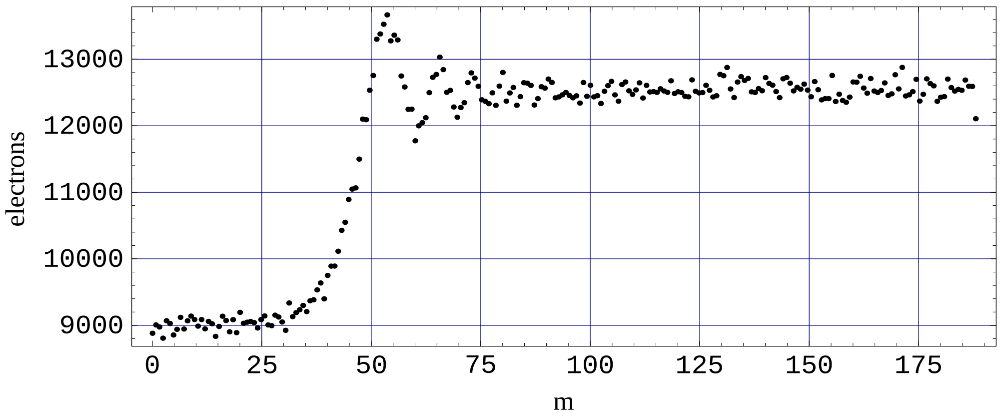

Figure 6.13: Simulated straight-edge diffraction light curve of a uniformly illuminating disc of $m_V = 6$, $\phi = 2$ mas at $\lambda = 600$ nm, $\Delta\lambda = 20$ nm, obtained with a conventional $D = 2.2$ m telescope. The speed of the shadow is 700 ms^{-1} with respect to the observer and the integration time is $\tau = 1.1$ ms.

- TDI on a 10 m telescope (Fig. 6.16) ($p = 0.5$ m, $n = 19$, all the other parameters are the same as above),

We selected $D = 2.2$ m because this size is often referred to as the practical maximum in LO observations.

We also computed a set of light curves for the model double star system (Fig. 6.1) by assuming that the system has an integrated magnitude of $m_V = 6$ (Figs. 6.17, 6.18, 6.19). If we compare these light curves to the theoretical light curve (Fig. 6.3) it is evident that the TDI method has great potential on large telescopes.

On the light curve recorded with the conventional method three, and perhaps four, fringes are visible and the light curve consists of a total of 250 points. TDI on the same telescope provides four times more data points and, although the SNR is not better, the larger number of data points results in higher accuracy during the data reduction. As many as seven fringes are evident. TDI on a 10 m telescope shows its true potential. At least 11 fringes are obvious, and the SNR is very high. The number of fringes is limited only by the broad wavelength band which can be limited. We

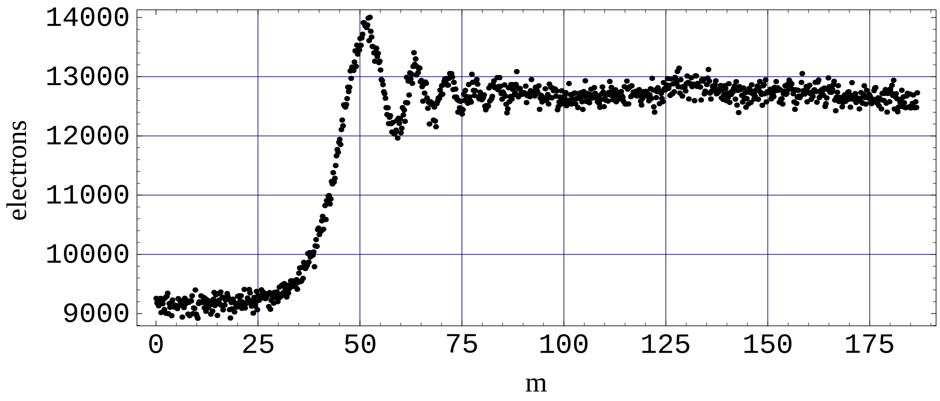

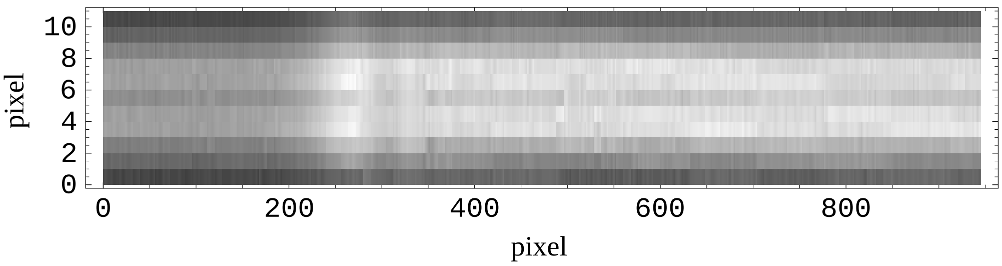

Figure 6.14: Simulated straight-edge diffraction light curve of a uniformly illuminating disc of $m_V = 6$, $\phi = 2$ mas at $\lambda = 600$ nm, $\Delta\lambda = 20$ nm, obtained with TDI on a $D = 2.2$ m telescope. The speed of the shadow is 700 ms^{-1} with respect to the observer and the projected pixel size is $p = 0.2$ m.

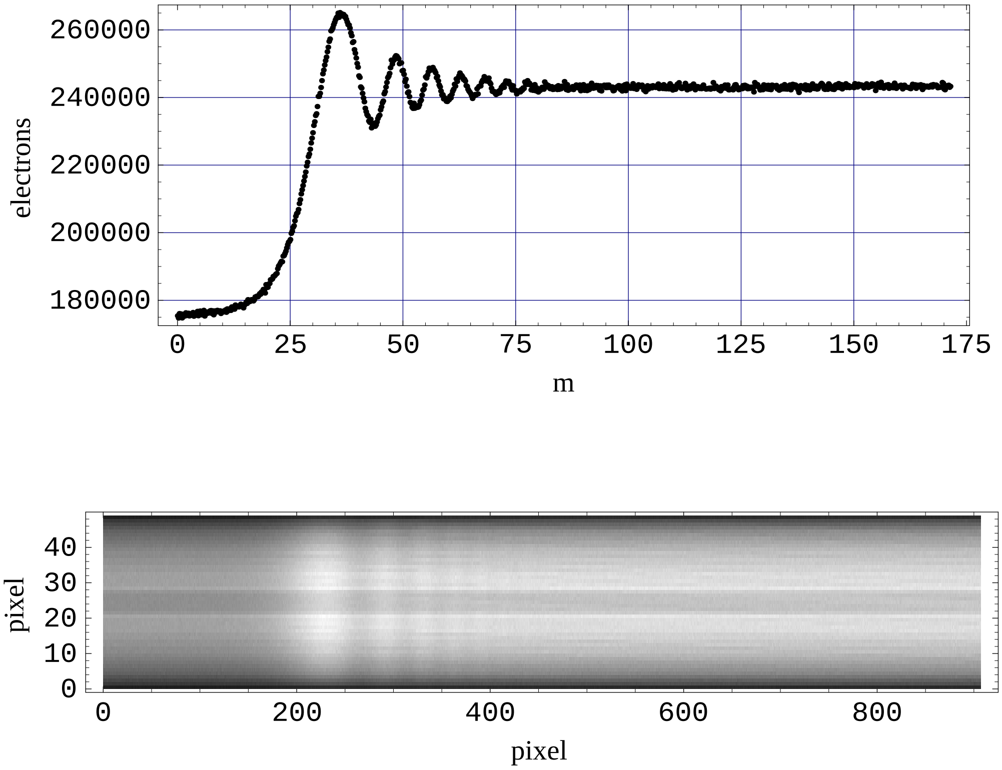

Figure 6.15: Simulated straight-diffraction light curve of a uniformly illuminating disc of $m_V = 6$, $\phi = 2$ mas at $\lambda = 600$ nm, $\Delta\lambda = 20$ nm, obtained with TDI on a $D = 10$ m telescope. The speed of the shadow is 700 ms^{-1} with respect to the observer and the projected pixel size is $p = 0.2$ m.

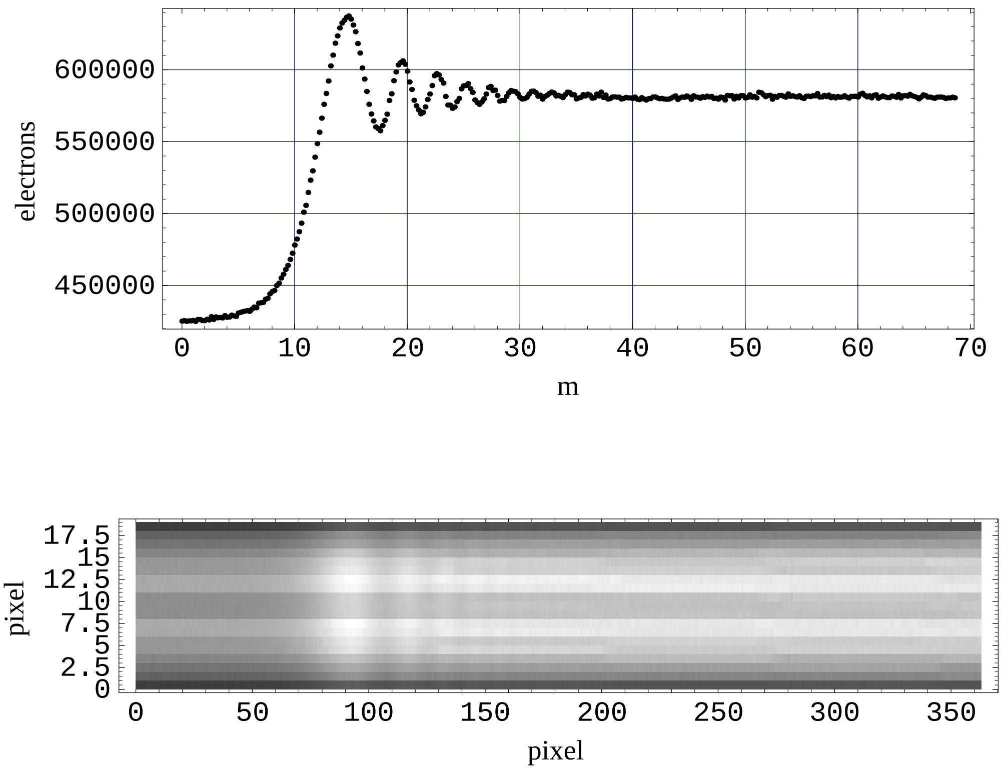

Figure 6.16: The same parameters as (Fig. VI.15) except the projected pixel size is $p = 0.5$ m.

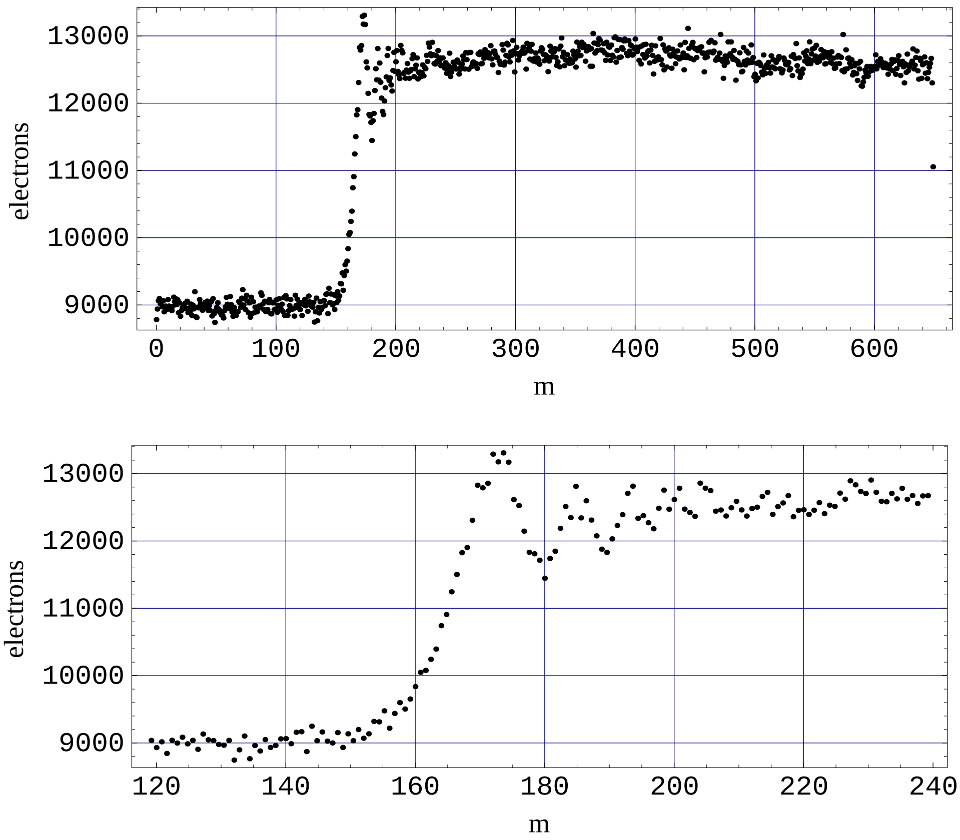

Figure 6.17: The model double star system (Fig. VI.1) observed with the conventional method on a 2.2 m telescope. The bottom picture is a close up of the transition.

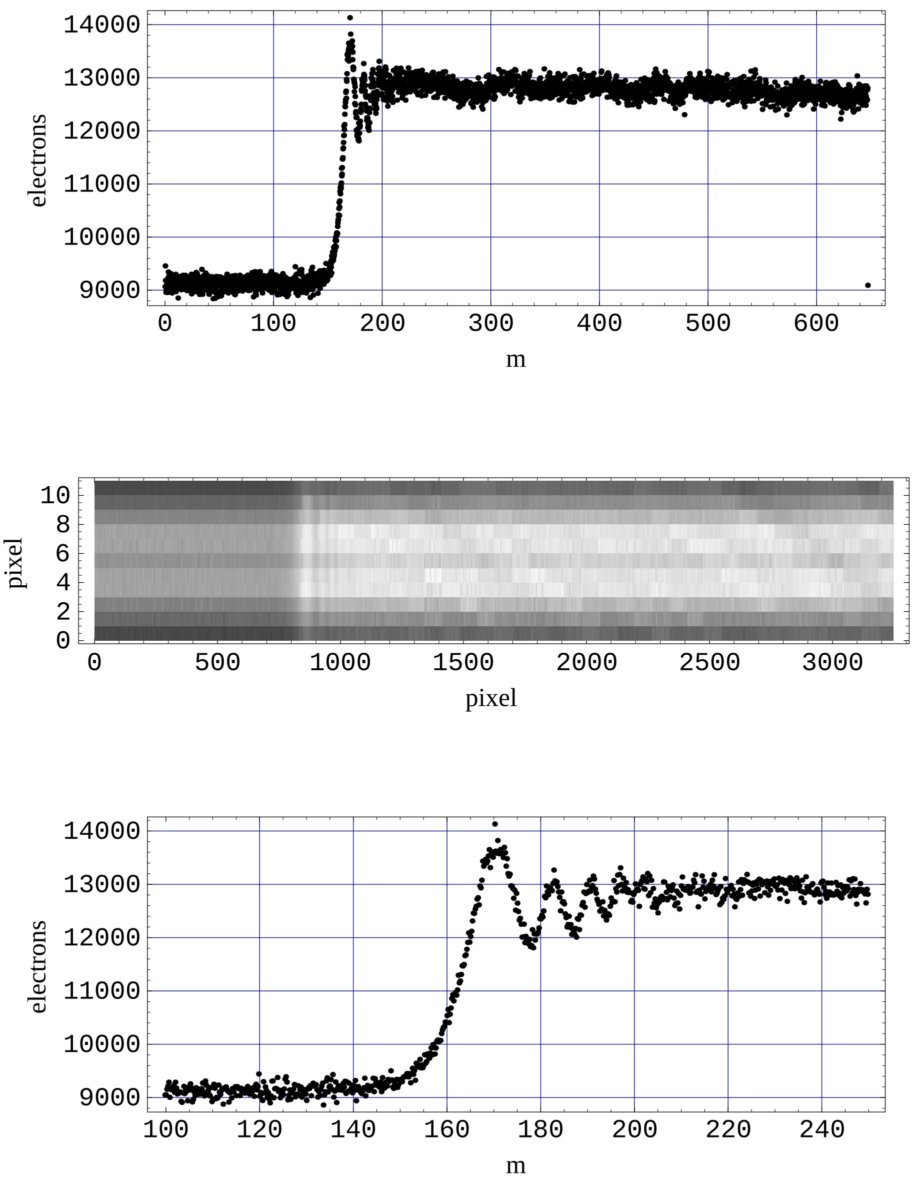

Figure 6.18: The double star system (Fig. VI.1) observed with the TDI method on a 2.2 m telescope, $p = 0.2$ m.

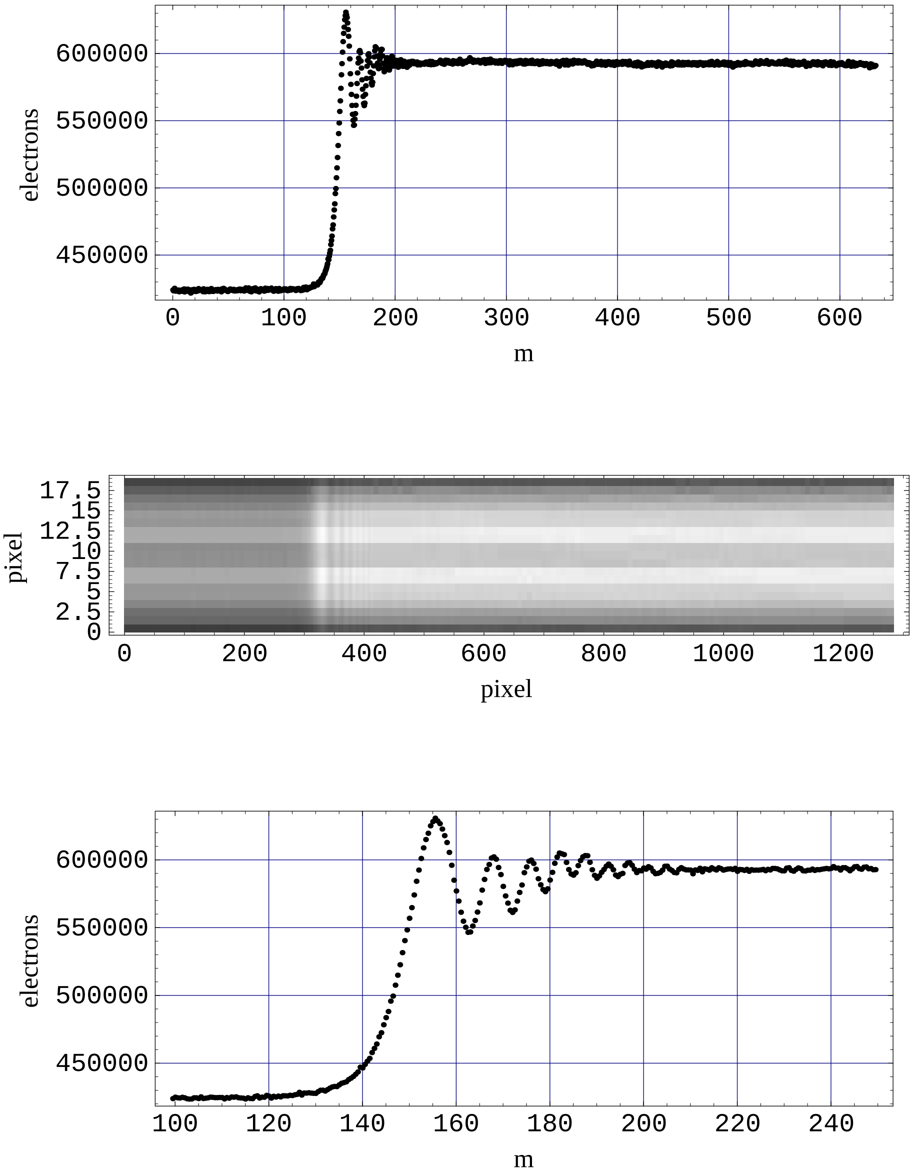

Figure 6.19: The double star system observed with the TDI method on a 10 m telescope, $p = 0.5$ m. ($m_V = 6$, $\lambda = 600$ nm, $\Delta\lambda = 20$ nm).

fitted both the conventional light curve and the 10 m TDI light curves with a set of test functions to find out the angular diameter of the object. From the conventional light curve we obtained $\phi = 1.9 \pm 0.28$ mas (3σ), while from the 10 m TDI light curve $\phi = 1.98 \pm 0.041$ mas (3σ). This result demonstrates the superiority of the TDI method. The diameter of the star agrees with the exact value within 2% at the 99.7 confidence level. The diameter of the star is well estimated by the conventional method, too, but with a relative error of 15% at the same confidence level.

It is clear from these synthetic TDI observations why the unknown lunar slope at the contact point of the occultation is not such a big problem. As long as we can see fringes in the output we can compute α from the inclination of the fringes and from φ (Eq. 5.42) and restore the output. After restoration we can add the output rows together to obtain a TDI light curve for further data processing.

CHAPTER VII

COMPARISON OF THE SIGNAL TO NOISE RATIOS OBTAINABLE BY THE TWO METHODS

Following the analysis in Sturmann (1994) we compare the SNR for a telescope of diameter D working in conventional mode to that for a telescope of diameter nD (where $n \geq 1$) working in TDI mode. The two telescope are equivalent from the point of view of the distortion they cause in the light curve (see Section 5.2). In TDI mode, both the background signal and the star signal are increased by a factor of n^2; thus,

$$SNR_{CNV} \approx \frac{S}{\sqrt{S + B + \sigma^2_{scintillation,CNV}}} \tag{7.1}$$

$$SNR_{TDI} \approx \frac{n^2 S}{\sqrt{n^2 S + n^2 B + \sigma^2_{scintillation,TDI} + \sigma^2_{CCD}}}, \tag{7.2}$$

where all noises associated with the CCD are included in σ^2_{CCD}.

We can compare the SNRs by defining the Gain as

$$\text{Gain} \equiv \frac{\text{SNR}_{TDI}}{\text{SNR}_{CNV}} \approx n^2 \sqrt{\frac{S + B + \sigma^2_{scintillation,CNV}}{n^2 S + n^2 B + \sigma^2_{scintillation,TDI} + \sigma^2_{CCD}}}. \tag{7.3}$$

The variances due to scintillation can be compared by taking into account the averaging effect of pixels (in TDI mode) and of the telescope aperture (in conventional mode) over the random shadow pattern. As we have seen in (Section 6.2.3), a number c_{00} (see Eq. 6.35) can be used to characterize the efficiency of an aperture to average irradiance fluctuations. Since the aperture size of the conventional telescope (D) is selected to be the same as the projected size of one pixel to the TDI telescope and there are $n^2\pi/4$ pixels illuminated in case of the TDI telescope, we estimate

$$\sigma^2_{scintillation,CNV} \simeq c_{00}\sigma^2_{sc}, \tag{7.4}$$

$$\sigma^2_{scintillation,TDI} \leq n^2 c_{00}\sigma^2_{sc}. \tag{7.5}$$

If the covariance is negligible between pixels, then $\sigma^2_{scintillation,TDI} \simeq n^2 c_{00}\sigma^2_{sc}$. Substituting (Eq. 7.4) into (Eq. 7.3) yields

$$\text{Gain} = n^2 \sqrt{\frac{S + B + c_{00}\sigma^2_{sc}}{n^2 S + n^2 B + n^2 c_{00}\sigma^2_{sc} + \sigma^2_{CCD}}}. \tag{7.6}$$

If σ^2_{CCD} is negligible compared to the shot and scintillation noises, then

$$\text{Gain} \simeq n. \tag{7.7}$$

We assume (Lang 1971, Richichi 1996) that the achievable angular resolution varies as SNR^{-1}; a Gain of n implies n times larger angular resolution capability.

I have computed how the SNR varies as a function of the apparent visual magnitude m_V using the scintillation index σ^2_{sc} and the projected pixel width p as parameters (Figs. 7.1, 7.2, 7.3). The illumination in the pupil plane was uniform and was varied according to m_V. The background was kept constant at $m_V^{bg} = 10$ square arcsecs^{-1}. The SNR was determined from the output of the observer program by computing the mean of the *star signal* = *total signal* − *background* and dividing this mean by the rms fluctuation of the *total signal*. It might seem surprising how SNR > 1000 can be achieved with a detector capable of handling a maximum of 350000 e^- per pixel. Taking only the shot noise into account, the SNR could not be higher than $\sqrt{350000} \simeq 590$ at even zero background. However, every output point is the sum of approximately n^2 pixels; thus, the SNR in principle could be as high as $590n$. The

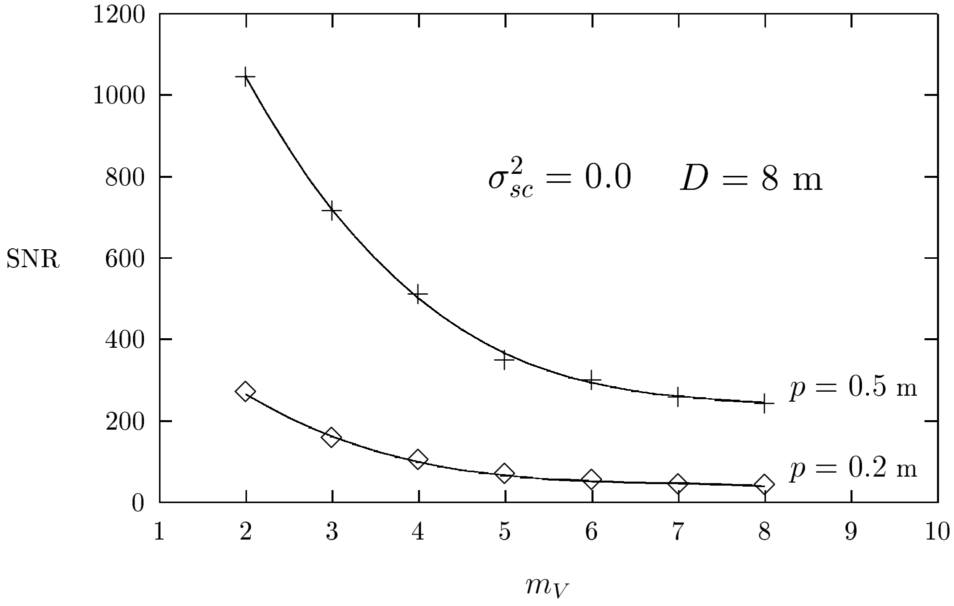

Figure 7.1: The SNR as a function of visual magnitude V. In the absence of atmospheric turbulence ($\sigma_{sc}^2 = 0.0$), a 8 m telescope would provide SNR over a thousand at $m_V = 2$ and $p = 0.5$.

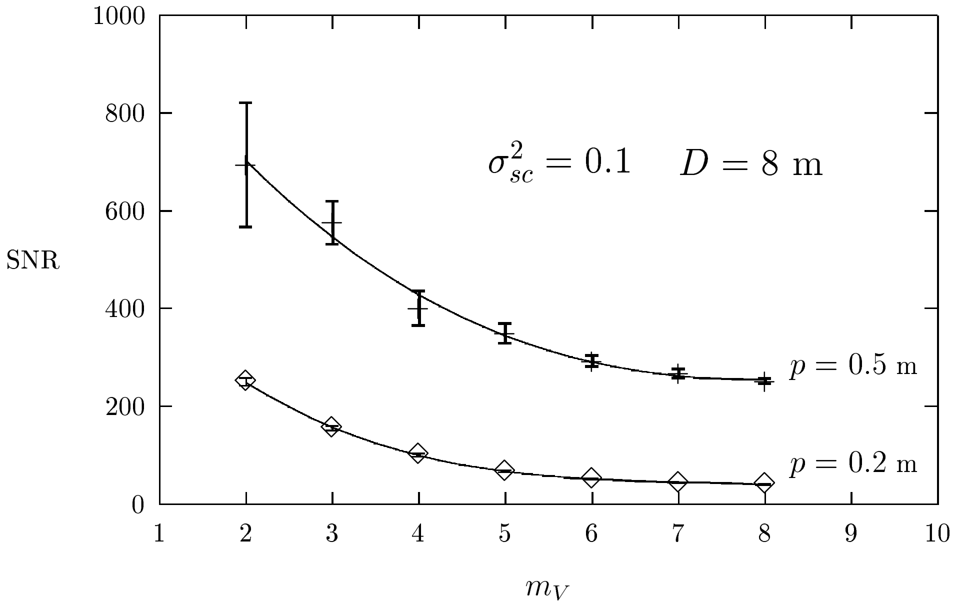

Figure 7.2: At $\sigma_{sc}^2 = 0.1$ the SNR decreases gradually and it is about 400 for a star of $m_V = 4$

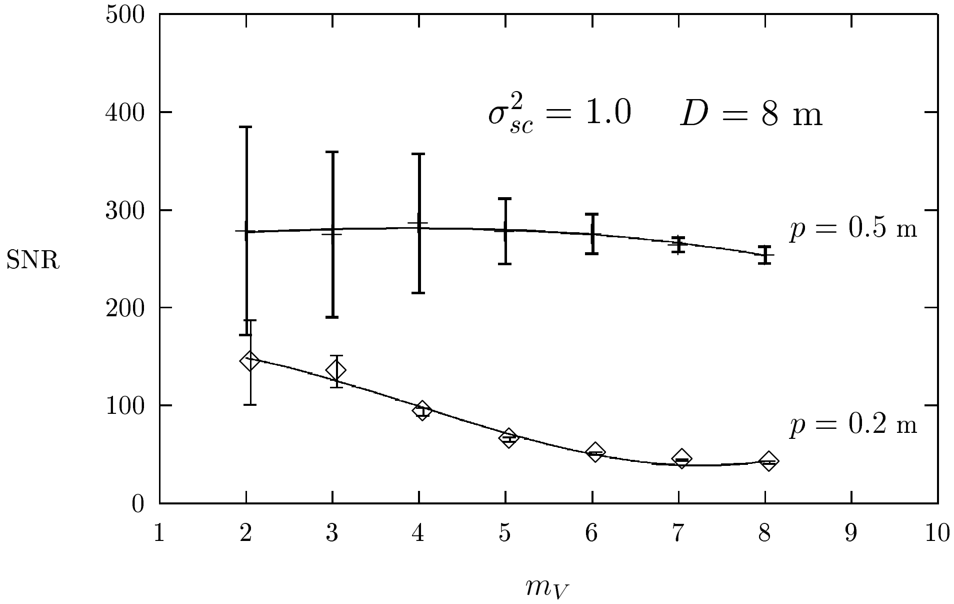

Figure 7.3: At strong turbulence ($\sigma_{sc}^2 = 1.0$), the SNR saturates for bright stars at about 280 for $p = 0.5$ m but the large error bars indicate that the SNR can be as high as 400 and as low as 160.

background signal decreases the SNR because it contributes only to the noise but not to the signal.

In the absence of atmospheric turbulence, an 8 m thelescope would provide SNR > 1000 for the brightest stars at $p = 0.5$ m (Fig. 7.1). We see that the anticipated SNR varies dramatically with increasing atmospheric turbulence (see Fig. 7.2 and Fig. 7.3). I believe a reasonable value for σ_{sc}^2 is below 0.1 under good observational circumstances, which predicts SNR ≈ 500 for a bright ($m_V = 4$) star with an 8 m telescope. Now the question is, what can be done with such a high quality light curve? We return to this question in Chapter X.

CHAPTER VIII

RESOLVABLE STARS WITH TDI BASED ON THE BARNES-EVANS RELATION

The definition of the visual surface-brightness parameter F_V (Barnes & Evans, 1976) is

$$F_V \equiv 4.2207 - 0.1V_0 - 0.5 \log \phi, \tag{8.1}$$

where V_0 is the unreddened apparent magnitude in Johnson's $UBVRI$ photometric system and ϕ is the stellar angular diameter expressed in mas. Wesselink (1969) demonstrated a tight relation between the visual surface brightness and the unreddened color index $(B-V)_0$. Barnes, Evans & Parsons (1976a, 1976b) have discussed in more detail the surface brightness as a function of several optical color indices such as $(B-V)_0$, $(R-I)_0$, and $(V-R)_0$. The best relationship (Fig. 8.1) was found for the index $(V-R)_0$ and is well defined for the entire range of stellar temperatures, without any dependence on luminosity class (which is not the case for $(B-V)_0$). Later Barnes, Evans & Moffet (1978) improved the relationship by adding 40 new stars to the 52 stars used in the previous calibration. The new calibration strengthened the previous assertion that the $F_V - (V-R)_0$ relation is independent of luminosity class and applicable to all spectral types from $O4$, to $M8$, S and C, as well as for white dwarfs. Di Benedetto (1993) discussed the effective temperatures of giants and supergiants cooler than the Sun based on the $F_V - (V-K)_0$ calibration.

By using the Barnes-Evans relation I have estimated the number of stars resolvable with TDI as well as with the conventional method. I used the tabulated $F_V - (V-R)_0$

relation (Barnes, Evans & Moffet, 1978, p. 298) for $-0.20 \leq (V-R)_0 \leq 0.78$ and

$$F_V = 3.841 - 0.321\,(V-R)_0 \tag{8.2}$$

for $(V-R)_0 \geq 0.80$ to obtain F_V as a function of $(V-R)_0$.

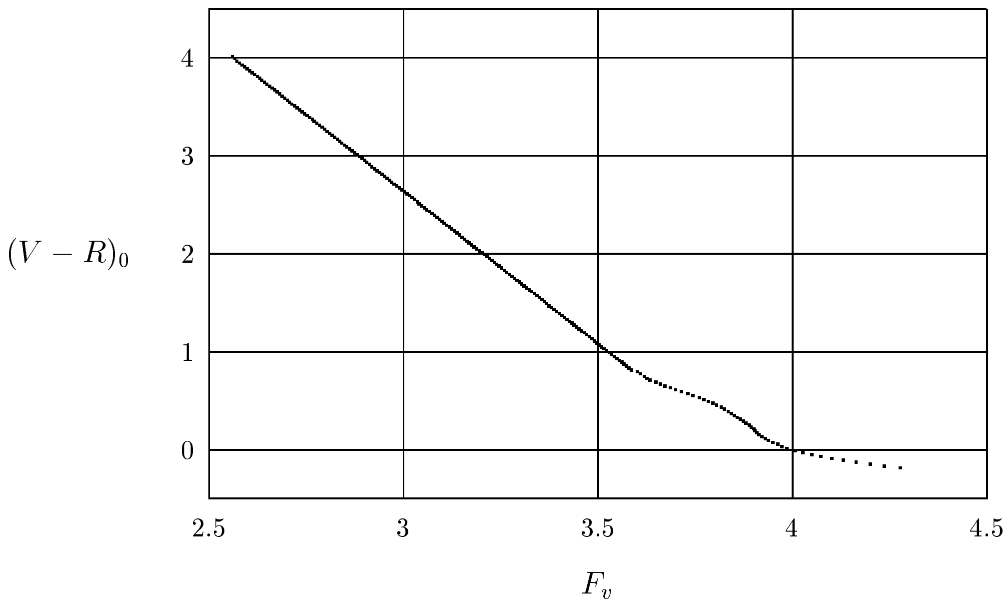

Figure 8.1: The empirical relationship between the visual surface brightness parameter F_V and the unreddened color index $(V-R)_0$.

Substituting (Eq. 8.2) into (Eq. 8.1), I solved the equation for V_0 at a set {0.1, 0.2, 0.5, 1.0, 2.0, 5.0, 10.0, 20.0, 50.0} mas of parameter ϕ. From the SAO Catalog, I extracted all (20413) stars that is occulted by the Moon [1].

Since there are no color indices in the SAO Catalog, only spectral types, I determined the $(V-R)_0$ color indices for the different spectral types from Johnson (1966). Each box (Fig. 8.2) represents a spectral type (from $B0$ to $M8$) and visual magnitudes in 1^m increments. The numbers in the boxes are the actual numbers of stars available for LO study extracted from the SAO catalog. The dashed curves

[1]The actual number must be a little higher because I did not take into account the finite size of the Earth.

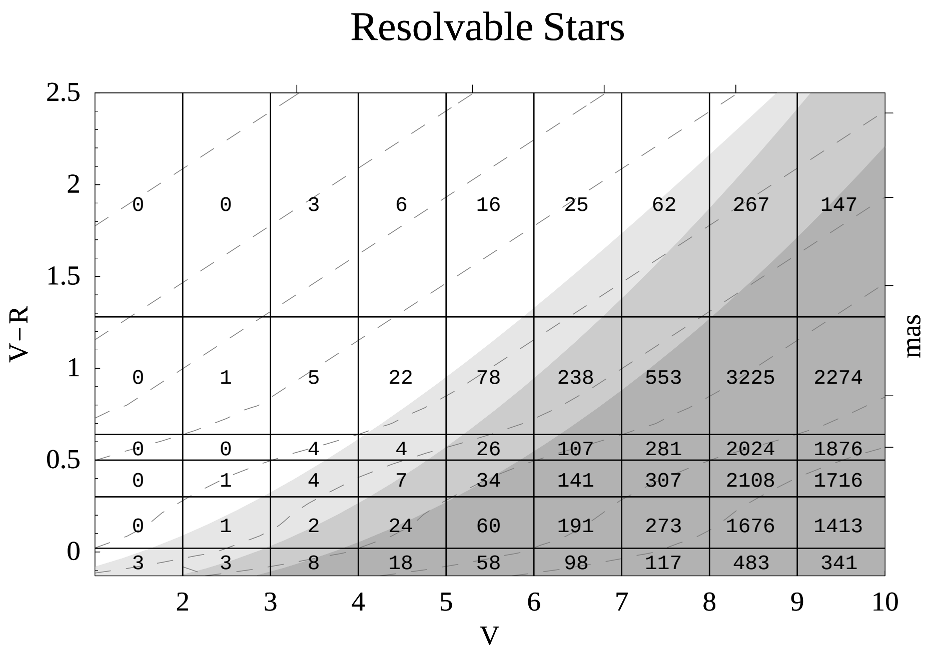

Figure 8.2: The number of stars in the SAO Catalog that can be occulted by the Moon sorted in boxes corresponding to V_0 and spectral type from $B0$ to $M8$. The stars situated above the shaded areas are resolvable with both the conventional and the TDI technique used on a 2-m telescope. The border between the differently shaded areas represent the angular resolution limit of a 2 m telescope using the conventional LO technique (no shading-light gray), for a 2 m telescope with TDI (ligh gray-medium gray) and for a 10 m telescope with TDI (medium gray-dark gray).

represent the angular sizes of stars from 0.1 mas (lower right) to 50.0 mas (upper left) computed from the Barnes-Evans relation. The border between the differently shaded areas represent the angular resolution limit of a 2 m telescope using the conventional LO technique (no shading-light gray), for a 2 m telescope with TDI (ligh gray-midium gray) and for a 10 m telescope with TDI (medium gray-dark-gray). Those stars (about 150) which are situated above the shaded areas are resolvable by both the conventional and the TDI technique used on a 2-m telescope. The stars in the dark gray shaded area are unresolvable even with 10 m telescope using TDI. According to these calculations, while there are about 150 stars resolvable with the conventional method, a 2-m telescope with TDI could increase this number by 50% and a 10-m telescope with TDI by about 500%. The angular resolution of a 10-m telescope is better than 0.5 mas for stars brighter than $V = 6$.

Evans (1957) and more recently Richichi (1990) found evidence of asymmetries in the intensity profile of Antares that might be due to very strong turbulence in the outer layer of the star. The improved SNR provided by the TDI method could be used to measure second-order effects on light curves due to asymmetric intensity profiles of late type giant stars.

CHAPTER IX

EXPERIMENTS

In this chapter I describe three benchtop experiments I have conducted during this dissertation research. Setting up a benchtop experiment had the additional benefit of allowing me to work with the camera any time not only on clear nights.

9.1 Lunar Occultation Simulator

The purpose of this experiment was to provide a simple and inexpensive way to test

- whether the HPC-1 CCD camera available at Dyer Observatory could be operated in TDI mode,
- if yes, whether the camera was fast enough for lunar occultation studies.

The answer to the first question is yes, to the second, no.

In this experiment, a moving target was imaged onto the CCD. I have developed the necessary software routines to track the moving image by shifting the charges in the CCD. By changing the speed of the target I have tested how fast the tracking could be done. At the maximum achievable tracking rate, the rate at which the charges were shifted across the CCD was 17 ms/row. Even if the entire aperture of the 24-inch telescope were imaged onto a single row, the necessary tracking rate would be 1.2 ms/row at the slowest possible shadow speed for a real LO event. Hence, real LO observations can not be carried out with this camera. The 17 ms/row maximum tracking rate is most likely due to the internal synchronization of the parallel shift register of the CCD to the 60 Hz line voltage (1/60 Hz $\simeq$ 17 ms). Since schematics of the camera electronics were not available and the manufacturer (Spectra Source) was uncooperative, this is only a possible explanation and not necessarily the right one.

Experimental Setup

A glass protractor plate 27 mm in diameter (Edmund Scientific #E39,455) with fine divisions was rotated with a small regulated DC motor (MicroMo 1219M012G + 10/1k64:1 + HEM1212M10) in front of a 10X microscope objective (Edmund Scientific 36132). The divisions were illuminated by a red LED driven by a variable current source. An adjustable diaphragm (Edmund Scientific 32621) and a ground glass plate (Edmund Scientific 43720) was placed in the image plane of the microscope objective (see Fig. 9.1). The diaphragm represented the primary aperture of a telescope and the fine divisions on the rotating protractor represented equidistant line elements in the diffraction pattern of an occulted star. The maximum diameter of the diaphragm was 10 mm. The 10 mm aperture corresponded to a 10-m telescope. The rotation speed of the protractor was set in such a way that, at 1 m ms^{-1} shadow speed, the 1 mm spot in the object plane[1] was swept by the divisions in 10 ms. Any shadow speed below 1 m ms^{-1} could be set by simply decreasing the rotation speed of the protractor. For example, a rotation speed of 50 mm s^{-1} corresponded to a shadow speed of 0.5 m ms^{-1}. The 10X microscope objective scaled down the necessary rotation speed

[1]A spot of 1 mm in diameter in the protractor is visible in the diaphragm plane when the diameter of the diaphragm is 10 mm.

by a factor of 10 and also minimized the error due to the fact that the divisions on the protractor were positioned as radial spokes of a circle, i.e., they were not parallel to one another. By adjusting the diaphragm from 1 mm to 10 mm, I could simulate different telescope apertures between 1 and 10 m. A 4X microscope objective (Melles Griot 04 OAS 006) was used to image the diaphragm (telescope aperture) onto the CCD. The actual size of the image on the CCD was 2.5 mm ($\sim$ 100 px) when using a 10 mm aperture.

The glass protractor was off axis to the optical axis of the microscope objectives. By rotating the protractor around the optical axis we could change the inclination of the divisions with respect to the rows of the CCD, thereby simulating alignment errors due to the lunar limb.

The brightness of the illumination of the protractor was adjusted to provide the same irradiance on the CCD as a star with a given magnitude at a given telescope aperture.

After calibrating the LED one could choose a telescope aperture, shadow speed, and star brightness by setting the diaphragm, motor speed, and the brightness of the LED, respectively. Then I could fine tune the parallel charge transfer rate (tracking rate) in order to determine the sharpest possible image of the moving line elements of the diffraction pattern (protractor divisions) for a given experimental setup. This procedure could be repeated at different limb inclinations by rotating the rotation axis of the protractor around the optical axis of the system.

This simple experimental setup could be used to carry out hardware and software tests during the development of a dedicated TDI camera.

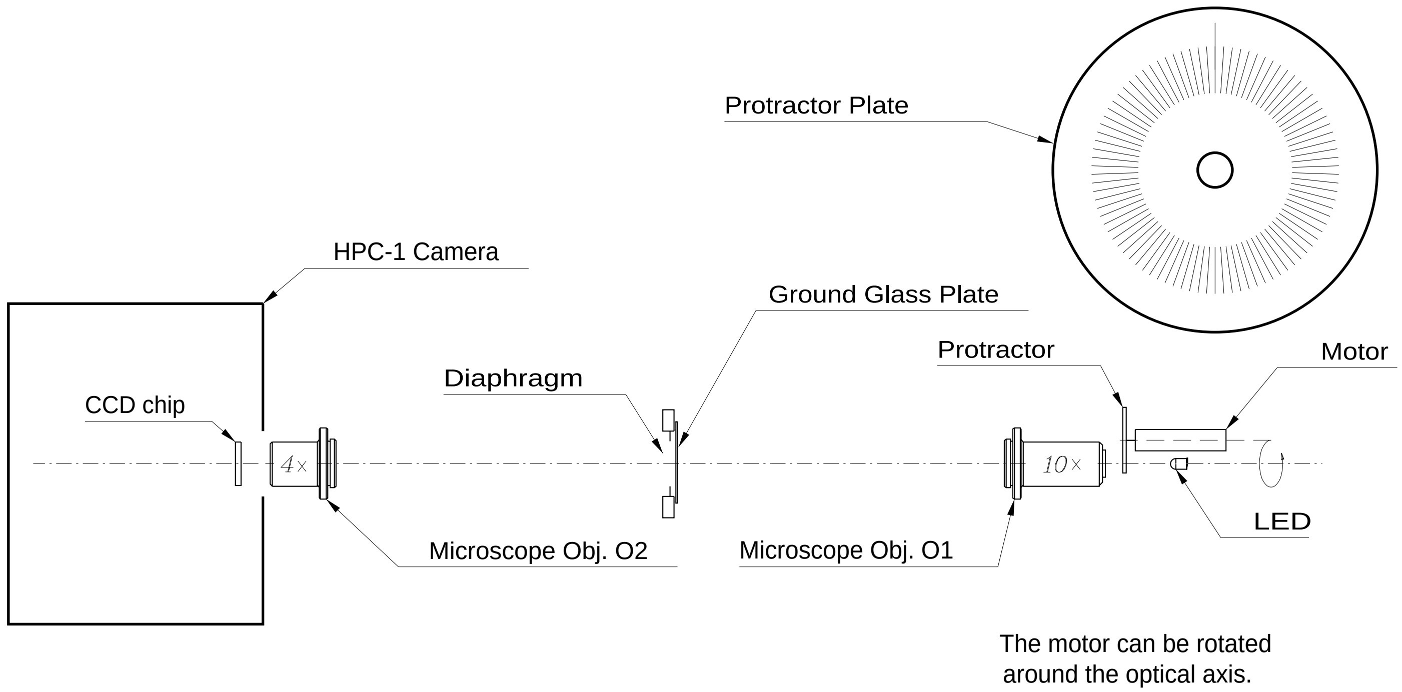

Figure 9.1: Experimental setup of the LO simulator

In order to vary the charge transfer rate in the parallel register, I built a programmable trigger source. This work was done by installing a second i8254 timer IC in the clock I built earlier for occultation observations. The second i8254 can be programmed to request interrupts from the host processor with any rate from 1 ms and up, in 10 μs steps. The parallel transfers in the CCD were initiated by an interrupt service routine in which the standard camera handler functions, provided by the camera manufacturer, were called.

As a by-product of this experiment, the camera now can be used in TDI mode as well as in the conventional still-image mode. This means that the sidereal motion of the sky can be compensated for by shifting the charges in the CCD instead of moving the telescope itself. I have made several experimental observations in TDI mode with the 24-inch telescope at the Dyer Observatory (Fig. 9.2). With minor effort one could implement the similar but even more versatile drift-scanning method (Mackay 1982). Both TDI and drift-scanning have numerous benefits over conventional CCD imaging, especially in sky surveys of low surface brightness objects.

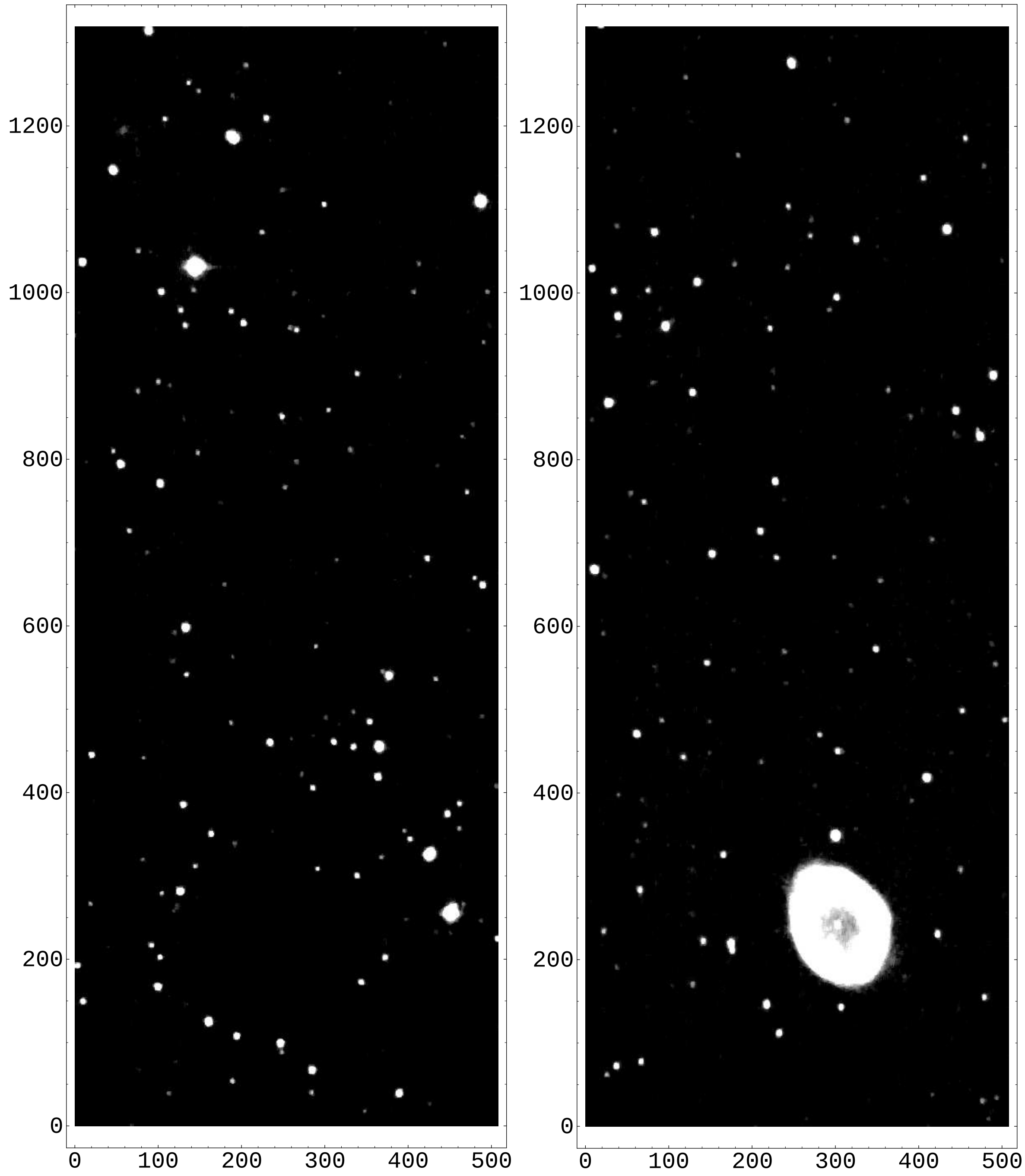

Figure 9.2: This broad band 512×2620 pixel picture of the Ring Nebula (M57) was taken in TDI mode with the HPC-1 camera in the Cassegrain focus of the 24-inch telescope at Dyer Observatory. The pixel scale is $0''.57$/px. The effective exposure is 23 s. North is right and west is down.

9.2 Sensitivity Variation Along Individual Pixel

Only one phase is held at high potential in CCDs during integrations. Applying a positive voltage to a gate causes the mobile positive holes in the p-type silicon to migrate toward the ground. The region, which is void of holes under each gate held at positive potential, is the depletion region. If a photon whose energy is greater than the energy gap of p-type silicon is absorbed in the silicon, it produces an electron-hole pair. If the electron pair was created in a depletion region, the electron stays within the depletion region whereas the hole migrates to the ground electrode. The electron is kept in a potential well under the positive gate. Electrons continue to accumulate in potential wells under positive gates during integrations. If an electron-hole pair was not created in a depletion region, the probability of losing the electron by recombination is high. Therefore, one would expect that the probability of detecting photons (collecting the associated electrons) is not uniform along a CCD. The probability is higher for those electrons that are released close to an active electrode. If the probability of electron detection is not uniform, then the effective diameter of the telescope (Eq. 5.5) has to be modified, because that was based on the assumption of uniform sensitivity[2].

Pixels are 3-D structures so the probability of collecting a photoelectron in a potential well also depends on the depth at which each electron is created. The penetration depth of a photon is wavelength-dependent and so the probability is also wavelength- dependent. The penetration depth is smaller for blue photons than for red photons so I predicted stronger variation in sensitivity for blue photons. The net effect of the variation in detection probability is already involved in the quantum

[2]This is true for not only TDI observations but any observation involving CCDs.

efficiency of the CCD; however, the spatial characteristics of this variation also can be important in modeling TDI LO occultations. Therefore, I have attempted to measure the variation in detection probability along individual pixels.

I created a very narrow line image by projecting a 3 mm long, 10 μm wide air slit (Melles Griot 04 PSM 002) onto the CCD by demagnifiying the slit with a 4x microscope objective (Melles Griot 04 OAS 006). At a numerical aperture of the microscope objective of 0.12, the line image on the CCD was approximately 4 μm wide at $\lambda = 680$ nm, the wavelength of the light emitted by the LED. Objectives with higher numerical aperture could not be used because the CCD was mounted 0.8 inches behind a window; therefore, the image distance had to be larger than this. The line image was adjusted parallel to the rows of the CCD. The line image was shifted in 5 μm steps parallel to the rows. After each step, the slit was illuminated by flashing a red LED for a short amount of time. The time was selected to provide a signal well above the noise level of the camera. Since the diffusion time scale of electrons is short compared to the read-out rate (17 ms/row) any variation that might be present in detection probability is small and due to recombination. After every LED flash, the same sub-window that contained the line image was read out and stored. During the data processing, the pixel values in a single column were added together. Only a single column was used and not the average of several columns, because there was no way to assure that the line image is indeed parallel to the rows due to the thinness of the line image.

If there were no variation in detection probability along pixels, then the sum of pixel values along a single column would be uniform regardless of the position of the line image on the pixel. However, if the probability varies, then the sum also varies periodically.

Let $L(x)$ be the intensity profile of the line-image and $S(x)$ the sensitivity along pixels. Let us assume that $S(x)$ is periodic, with period p the pixel size. After flashing the LED, the signal in the j^{th} pixel along the selected column is proportional to

$$P_j(u) = \int_{(j-1)p}^{jp} L(x-u)S(x)\,dx, \tag{9.1}$$

where u is the displacement of the line-image from an arbitrary starting point. Summing P_j over the column we obtain

$$Q(u) = \sum_j P_j(u) = \sum_j \int_{(j-1)p}^{jp} L(x-u)S(x)\,dx. \tag{9.2}$$

If the subwindow is sufficiently broad, then $Q(u)$ can be estimated by

$$Q(u) = \int_{-\infty}^{\infty} L(x-u)S(x)\,dx. \tag{9.3}$$

$Q(u) = const$ if $S(x) = const$ and if the energy in the LED flashes is constant. If $S(x) \neq const$, then it is periodic with period p and, therefore, we can expand it in the Fourier series

$$Q(u) = \int_{-\infty}^{\infty} L(x-u)\sum_k s_k e^{\frac{2\pi i}{p}kx} dx = \sum_k s_k \int_{-\infty}^{\infty} L(x-u) e^{\frac{2\pi i}{p}kx} dx. \tag{9.4}$$

Substituting for $x' = x - u$ yields

$$Q(u) = \sum_k \left[s_k \int_{-\infty}^{\infty} L(x') e^{\frac{2\pi i}{p}kx'} dx' \right] e^{\frac{2\pi i}{p}ku}. \tag{9.5}$$

Thus, $Q(u)$ is also periodic with the same period p and its Fourier coefficients are

$$q_k = s_k \int_{-\infty}^{\infty} L(x') e^{\frac{2\pi i}{p}kx'} dx'. \tag{9.6}$$

We can obtain q_k-s by expanding the measured function $Q(u)$. Then the Fourier components of pixel sensitivity $S(x)$ are

$$s_k = \frac{q_k}{\int\limits_{-\infty}^{\infty} L(x')e^{\frac{2\pi i}{p}kx'}dx'}. \tag{9.7}$$

Because $L(x)$ is presumably an even function, we find

$$s_k = \frac{q_k}{\int\limits_{-\infty}^{\infty} L(x')\cos\frac{2\pi}{p}kx'\,dx'}. \tag{9.8}$$

In the first experiment I observed a variation of about 10% in sensitivity using a

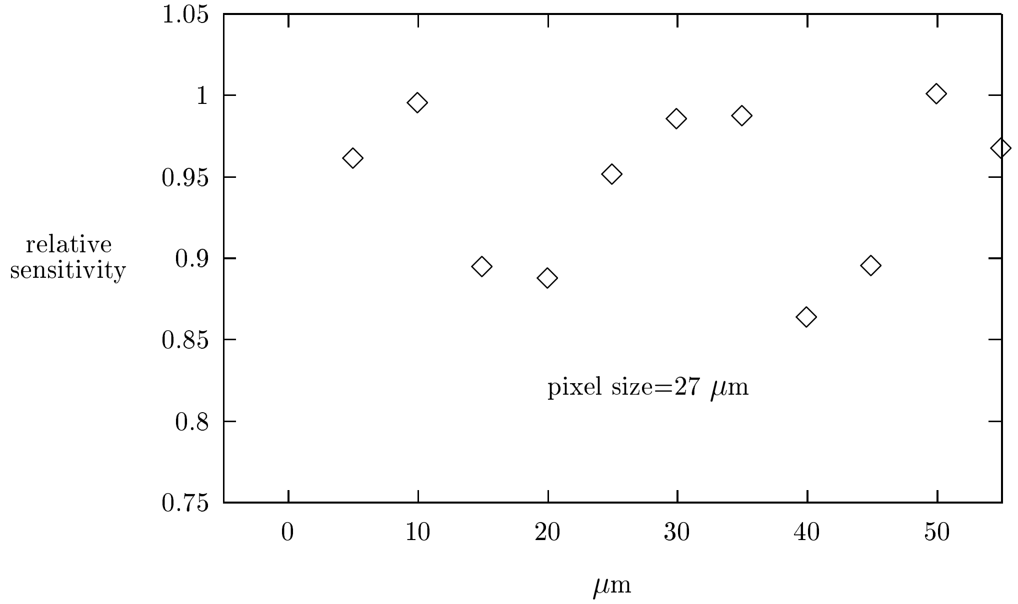

Figure 9.3: Sensitivity variations along individual pixels.

red LED. However, I could not reproduce that result later. Therefore, this result is inconclusive. The measuring setup would have to be improved in order to test if there were any measurable variation present. Lack of funds precluded further testing; in addition, for the purpose of this research project, the small possible variation I observed did not justify any additional effort.

Nevertheless, it would be interesting to do this measurement again with an improved setup and perhaps mapping a pixel in 2-D by a small point image instead of a line image.

9.3 Calibration of the HPC-1 CCD Camer

The CCD must be calibrated in order to relate the analog-to-digital (ADU) units to actual photo-electron numbers.

Following Janesick (Janesick 1991), if n is the electron number in a pixel, a random variable with Poisson distribution, then

$$\frac{\overline{n}}{\sigma_n^2} = 1, \tag{9.9}$$

where $\overline{n}$ is the mean electron number and σ_n^2 is its variance. Let m be the signal obtained from the camera in ADU be

$$\overline{m} = \frac{\overline{n}}{\mathrm{GAIN}(e^-/\mathrm{ADU})} \tag{9.10}$$

and

$$\sigma_m^2 = \frac{\sigma_n^2}{\mathrm{GAIN}^2} \; . \tag{9.11}$$

It then follows that

$$\frac{\overline{m}}{\sigma_m^2} = \frac{\overline{n}}{\mathrm{GAIN}} \frac{\mathrm{GAIN}^2}{\sigma_n^2} = \mathrm{GAIN} \tag{9.12}$$

and the read-out noise R in electrons is

$$\mathrm{R}(e^-) = \mathrm{GAIN}\ \sigma_m. \tag{9.13}$$

In practice, say a 20×20 pixel box is selected on the CCD array in a clear area, i.e., one with no hot or dark pixels or other blemishes. First, two dark frames are taken and subtracted pixel by pixel and the standard deviation of the resulting frame is computed, which is equal to $\sqrt{2}\sigma_n$, where σ_n is the read noise floor (all in units of ADU). Next a signal level is chosen such that the standard deviation of the signal is much larger than the standard deviation associated with the noise floor. Three frames are obtained: a dark frame (to provide the system offset information) and two identical LED-illuminated frames. Subtracting the dark frame from one of the signal frames and taking the mean ADU value provides the mean signal value S, and subtracting one signal frame from the other and calculating the standard deviation yields the value $\sqrt{2}\sigma_S$, where σ_S is the standard deviation in S. Then the gain of the camera can be written as

$$\text{GAIN}(e^-/\text{ADU}) = \frac{S}{\sigma_S^2 - \sigma_n^2}. \tag{9.14}$$

This is a fast method but one with limited accuracy because the gain is determined at only one signal level. I have followed another method due to Janesick (1991) to measure the *photon transfer curve* of the camera. The photon transfer curve is a plot of random noise, σ_S, as a function of signal, S in ADU, generated by the CCD. Usually, there are three distinct noise regimes that can be identified in plots like (Fig. 9.4). The first regime, the read noise floor, σ_R, represents the intrinsic noise measured under totally dark conditions. This noise is associated with on-chip amplifier noise and any other noise sources that are independent of the signal level. As the illumination on the CCD is increased, the noise becomes dominated by the shot noise of the signal. This is the middle region of the curve. Since the uncertainty in the quantity of charge present in any pixel (the noise) is proportional to the square root of the number of incident photons (the signal), the slope here is 1/2. The third

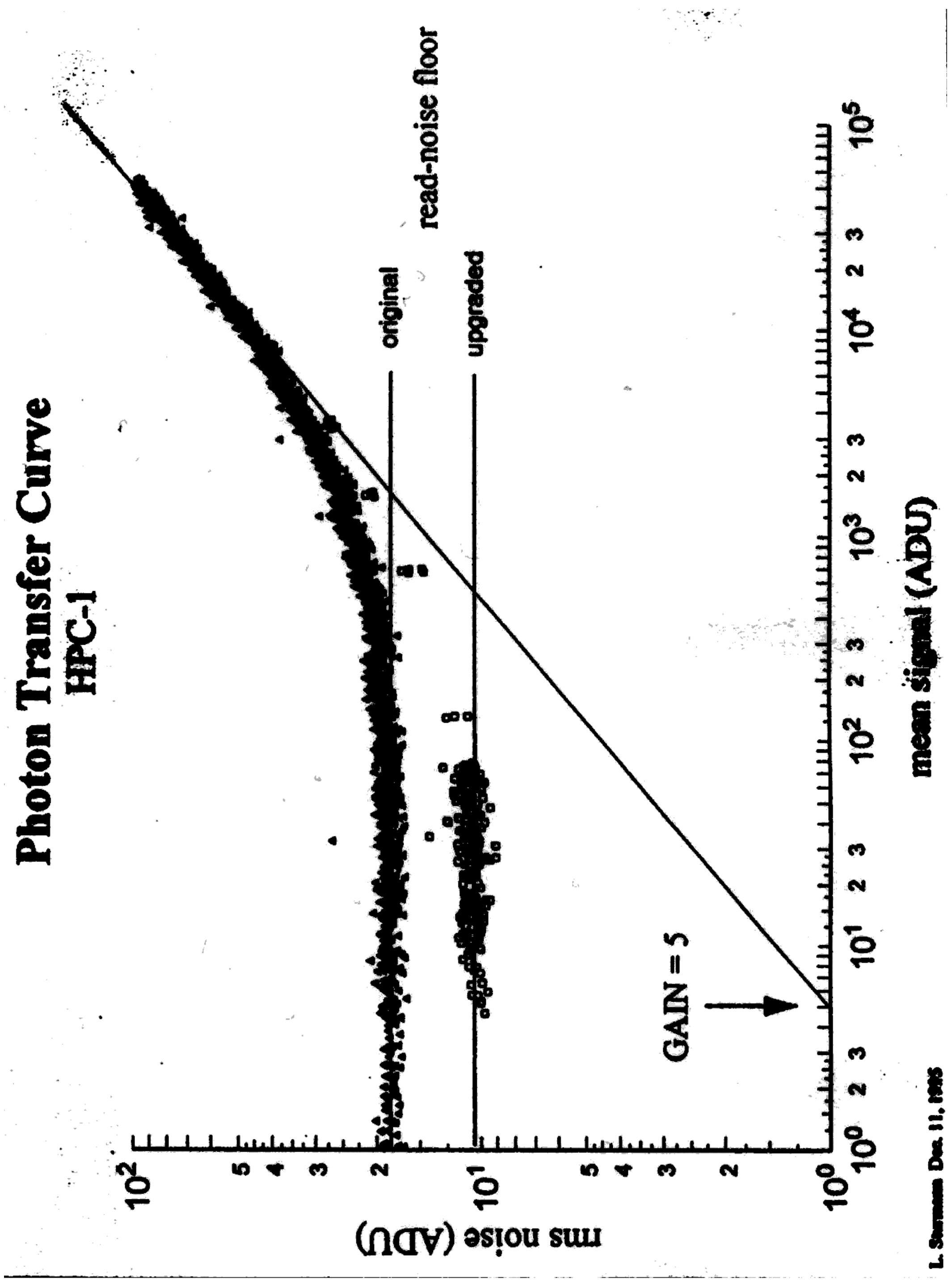

Figure 9.4: Photon transfer curve generated by the HPC-1 camera at Dyer Observatory (20 × 20 subarray and red LED).

regime is[3] governed by fixed pattern noise resulting from sensitivity differences among pixels. Because of processing variations during manufacturing (photo-mask alignment error, for example), each pixel exhibits its own collecting volume and characteristic responsivity. Noise produced by pixel nonuniformity is proportional to signal and consequently produces a characteristic slope of unity. Full well is achieved at some illumination level in the fixed pattern noise regime and is seen as a break in the slope of one. At this point charge spreads between pixels, a phenomenon called blooming.

The curve is generated by varying the exposure sequence, beginning with a dark frame. Then the total amount of incident light is increased and the signal and noise levels are measured. The uniform illumination on the CCD is achieved by utilizing a 6-inch integrating sphere (Lab Sphere) in front of the camera.

The abscissa of every point was obtained from

$$S = \frac{1}{400}\sum_{i=1}^{400}(S_i - Bias_i), \tag{9.15}$$

where $Bias$ is the fixed average electrical offset which was found from a single dark exposure derived from the same pixel region.

Noise data for the ordinate is found by calculating the standard deviation of the 400 pixels after pixel-to-pixel nonuniformity is removed. Pixel nonuniformity is eliminated by differencing, pixel by pixel, two identical frames taken at the same exposure level. The variance, σ_s^2, of this differenced frame is given by

$$\sigma_S^2 = \frac{1}{2\times 400}\sum_{i=1}^{400}(S_i - S_i')^2. \tag{9.16}$$

To carry out this measurement that includes many data points, I had a set up that measured automatically without human intervention.

[3]This region is missing rfom this plot because the low illumination level

The gain of the camera was found to be five. This is reasonable since the full well for the CCD chip is about 350,000 e^-, which can be covered by the 65535 digital levels of the built-in 16-bit analog-to-digital converter at a gain of five.

CHAPTER X

CONCLUSION

The goal of this dissertation was to show the potential benefits of the application of the TDI method in LO studies in comparison to the conventional method of LO observations. The notable scientific advance is the use of a novel charge transfer scheme that greatly increases the sensitivity compared to conventional recording techniques, resulting in improved SNRs and angular resolution. The TDI method enables us to extend the lunar occultation technique to large telescopes and faint objects. With this method not only are large telescopes usable but they are favored for LO studies; with the largest available telescopes, we can achieve better than 2% accuracy in angular diameters for stellar objects larger than 1 mas and brighter than $m_V = 6$. The improvement in angular resolution is due to the high SNR compared to that obtainable with the conventional method. Additionally, the 2-D output of a TDI camera can be used to obtain information about the lunar limb where the occultation occured thereby opening a way to freeing light curves from limb effects. The TDI method does not require any special instrumentation. In fact, TDI CCD cameras are readily available from several vendors. However, note that this method is best on large telescopes.

APPENDIX A

INTRODUCING SPATIAL CORRELATION IN AN UNCORRELATED RANDOM PATTERN

In this Appendix, we present a method to introduce spatial correlation in uncorrelated random fields. This method was followed in our simulations of random shadow patterns in the pupil plane of a telescope in Chapter 6.2.2.

Let u be a 2-dimensional, homogeneous, stationary random field with standard Gaussian white-noise distribution. Then the mean and variance of u are $\overline{u} = 0$ and $\sigma_u^2 = 1$, respectively, and the spatial correlation function[1] $\Gamma_u(\mathbf{x}, \mathbf{x}') = \overline{u(\mathbf{x})u(\mathbf{x}')} = \delta(\mathbf{x} - \mathbf{x}')$.

Let $W(\mathbf{x})$ be an integrable function, normalized such that

$$\iint\limits_{-\infty}^{+\infty} W(\mathbf{x}) d^2x = 1. \tag{1.1}$$

We introduce spatial correlation in the Gaussian random pattern by performing a convolution of the random pattern with a function W such that $w \equiv u * W$, where $*$ indicates convolution. Then $\overline{w} = \overline{u}$ because, from the definition of w,

$$\begin{aligned} w(\mathbf{x}) &= \iint_{-\infty}^{+\infty} u(\mathbf{x} - \mathbf{x}') W(\mathbf{x}')\, d^2x' \\ \overline{w(\mathbf{x})} &= \iint_{-\infty}^{+\infty} \overline{u(\mathbf{x} - \mathbf{x}')} W(\mathbf{x}')\, d^2x' \end{aligned} \tag{1.2}$$

and, since u is homogeneous and W is normalized,

$$\overline{w} = \overline{u} \underbrace{\iint_{-\infty}^{+\infty} W(\mathbf{x}')\, d^2x'}_{=1}. \tag{1.3}$$

[1] The spatial correlation function equals the covariance function since $\overline{u} = 0$.

The correlation function $\Gamma_w(\mathbf{s})$ of w is

$$
\begin{aligned}
\Gamma_w(\mathbf{s}) &= \overline{w(\mathbf{x})w(\mathbf{x}+\mathbf{s})} && (1.4)\\
&= \overline{\iint_{-\infty}^{+\infty} u(\mathbf{x}-\mathbf{x}')W(\mathbf{x}')\,d^2x' \iint_{-\infty}^{+\infty} u(\mathbf{x}+\mathbf{s}-\mathbf{x}'')W(\mathbf{x}'')\,d^2x''} && (1.5)\\
&= \overline{\int\cdots\int_{-\infty}^{+\infty} u(\mathbf{x}-\mathbf{x}')u(\mathbf{x}+\mathbf{s}-\mathbf{x}'')W(\mathbf{x}')W(\mathbf{x}'')d^2x'd^2x''} && (1.6)\\
&= \int\cdots\int_{-\infty}^{+\infty} \overline{u(\mathbf{x}-\mathbf{x}')u(\mathbf{x}+\mathbf{s}-\mathbf{x}'')}W(\mathbf{x}')W(\mathbf{x}'')d^2x'd^2x'' && (1.7)\\
&= \int\cdots\int_{-\infty}^{+\infty} (\overline{u}^2+\sigma_u^2\delta(\mathbf{x}''-\mathbf{x}'+\mathbf{s}))W(\mathbf{x}')W(\mathbf{x}'')d^2x'd^2x'' && (1.8)\\
&= \overline{u}^2+\sigma_u^2\iint_{-\infty}^{+\infty} W(\mathbf{x}')W(\mathbf{x}'-\mathbf{s})d^2x' && (1.9)\\
&= \iint_{-\infty}^{+\infty} W(\mathbf{x}')W(\mathbf{x}'-\mathbf{s})d^2x', && (1.10)
\end{aligned}
$$

since u is a standard Gaussian random variable. Because $\overline{u} = 0$, the covariance function $C_w(\mathbf{s})$ is identical with the correlation function $\Gamma_w(\mathbf{s})$ that is equal to the convolution of W with itself. If W is circularly symmetric, then C_w is that too, i.e., the field is isotropic.

The variance σ_w^2 of w is

$$\sigma_w^2 = C_w(\mathbf{0}) = \iint\limits_{-\infty}^{+\infty} W^2(\mathbf{x}')d^2x' < 1. \qquad (1.11)$$

Therefore, in order to generate a random field with a given covariance function C_w, it is necessary to compute a function W by solving the equation $C_w = W * W$ and then to convolve a standard Gaussian white noise pattern with W. The convolution leaves the mean value unchanged but the variance decreases according to (1.11). By the transformation $w \to w/\sigma_w$, the variance $\sigma_w^2 = 1$ can be restored and w remains standard Gaussian.

APPENDIX B

TRANSFORMATION OF RANDOM VARIABLES

This Appendix describes how to transform standard Gaussian random variables into log-normal random variables. This algorithm was used in Chapter 6.2.2.

Theorem 1 *If w is a standard Gaussian random variable, then $y \equiv a\exp(bw)$, $(a, b > 0)$ is log-normal.*

Since w is standard Gaussian, its probability density function is

$$p_w(w) = \frac{1}{\sqrt{2\pi}} \exp\left\{-\frac{w^2}{2}\right\}. \tag{2.1}$$

The transformation $y \equiv a\exp(bw)$ $(a, b > 0)$ is a monotonic function of w. The probability of $P[y \leq y_0]$ is equal to the probability of $P[w \leq \frac{1}{b}\ln\frac{y_0}{a}]$, i.e.,

$$\int_0^{y_0} p_y(y)\,dy = \int_0^{\frac{1}{a}\ln\frac{y_0}{b}} p_w(w)\,dx. \tag{2.2}$$

By introducing y into the second integral such that $w = \frac{1}{b}\ln\frac{y}{a}$,

$$\int_0^{y_0} p_y(y)\,dy = \int_0^{y_0} \frac{1}{ay} p_w(\frac{1}{b}\ln\frac{y}{a})\,dy \tag{2.3}$$

is true for any allowed values of a and b. Therefore, since the arguments of the two integrals must be equal, we can write

$$p_y(y) = \frac{1}{ay} p_w(\frac{1}{b}\ln\frac{y}{a}) = \frac{1}{\sqrt{2\pi}by} \exp\left\{-\frac{(\ln\frac{y}{a})^2}{2b^2}\right\}. \tag{2.4}$$

It also can be shown, that

$$\bar{y} = \int_0^{\infty} y\,p_y(y)\,dy = a\exp\left\{\frac{b^2}{2}\right\}, \tag{2.5}$$

$$\overline{y^2} = \int_0^\infty y^2\, p_y(y)\, dy = a^2 \exp(2b^2) \tag{2.6}$$

and the variance of y is

$$\sigma_y^2 = \overline{y^2} - \bar{y}^2 = \bar{y}^2 \left[\exp(b^2) - 1\right]. \tag{2.7}$$

The normalized variance of y, given by

$$\sigma_0^2 = \frac{\sigma_y^2}{\bar{y}^2} = \exp(b^2) - 1, \tag{2.8}$$

is a function only of b. For a required normalized variance σ_0^2 we have to select b such that

$$b = \sqrt{\ln(\sigma_0^2 + 1)} \tag{2.9}$$

and then

$$\bar{y} = a\sqrt{\sigma_0^2 + 1}. \tag{2.10}$$

For a given mean $\bar{y}$, a has to be selected such that

$$a = \frac{\bar{y}}{\sqrt{\sigma_0^2 + 1}}. \tag{2.11}$$

The transformation which transforms a standard Gaussian random variable w into a log-normal random variable y with predefined normalized variance σ_0^2 and mean $\bar{y}$ is

$$y = \frac{\bar{y}}{\sqrt{\sigma_0^2 + 1}} \exp\left[w\sqrt{\ln(\sigma_0^2 + 1)}\right]. \tag{2.12}$$

APPENDIX C

SPECTRAL COMPONENTS COMBINE INCOHERENTLY

Following Born & Wolf (1975), let us investigate the intensity at point O due to a source S radiating with spectral energy distribution $e(k)$ and $k = 2\pi/\lambda$. The electric field $\mathbf{E}$ at O due to a single spectral component of the radiation can be described as

$$\mathbf{E} = \mathrm{Re}\left[\mathbf{A}(\mathbf{r})e^{-ikct}\right] = \frac{1}{2}\left[\mathbf{A}(\mathbf{r})e^{-ikct} + \mathbf{A}^*(\mathbf{r})e^{ikct}\right], \tag{3.1}$$

where c is the speed of light. $\mathbf{A}(\mathbf{r}) = (a_1(\mathbf{r})e^{ig_1(r)}, a_2(\mathbf{r})e^{ig_2(r)}, a_3(\mathbf{r})e^{ig_3(r)})$ is a complex vector where $a_i(\mathbf{r})$ and $g_i(r)$ are real functions. The intensity of light is defined as the time average of the amount of energy which crosses a unit area perpendicular to the direction of energy flow in unit time and it is proportional to

$$I \sim \left\langle \mathbf{E}^2 \right\rangle .$$

Let us take two spectral components $g(k)\frac{e^{ik(s-ct)}}{s}$ and $g(k')\frac{e^{ik'(s-ct)}}{s}$ and compute the intensity at O due to these two waves. The instantaneous intensity $i(t)$ at O is given by

$$\begin{aligned} i(t) &= \left(g(k)\frac{e^{ik(s-ct)}}{s} + g(k')\frac{e^{ik'(s-ct)}}{s}\right)\left(g(k)\frac{e^{-ik(s-ct)}}{s} + g(k')\frac{e^{-ik'(s-ct)}}{s}\right) && (3.2)\\ &= \frac{g^2(k)}{s^2} + \frac{g^2(k')}{s^2} + \frac{2g(k)g(k')}{s^2}\cos((k-k')(s-ct)) && (3.3)\\ &= i + i' + 2g(k)g(k')\cos((k-k')(s-ct)), && (3.4) \end{aligned}$$

where we also introduced $i \equiv g^2(k)/s^2$ and $i' \equiv g^2(k')/s^2$ as the intensities at O due to the two spectral components alone.

The function $i(t)$ is a rapidly oscillating function if $k \neq k'$ with constant mean $i + i'$. The frequency of oscillation $f = (k - k')c \simeq 2\pi c\Delta\lambda/\lambda^2$ is high for optical radiation. At $\lambda = 600$ nm, $f \simeq 5.2 \times 10^{21} \Delta\lambda$ Hz, which is well beyond the capabilities of modern detectors even at $\Delta\lambda$ as narrow as 1 nm. Therefore, every detector and every measurement averages $i(t)$ over a much longer time τ than $1/f$. The average intensity I over a time τ is

$$\begin{aligned} I &= \langle i(t) \rangle = i + i' + 2g(k)g(k')\frac{1}{\tau}\int_0^\tau \cos((k-k')(s-ct))dt & (3.5) \\ &= i + i' + \frac{2g(k)g(k')}{s^2}\cos\left((k-k')\left(s-\frac{c\tau}{2}\right)\right)\frac{\sin\left((k-k')\frac{c\tau}{2}\right)}{(k-k')\frac{c\tau}{2}}. & (3.6) \end{aligned}$$

When $k = k'$, the observable intensity $I = 4i$ is four times the intensity due to a single spectral component alone. When $k \neq k'$, the last term in (3.5) drops rapidly and reaches its first zero when $(k-k')\frac{c\tau}{2} = \pi$. Thus the condition for observable interference between the two spectral components of a broad spectrum is $(k-k')\frac{c\tau}{2} \ll \pi$. Substituting $k = 2\pi/\lambda$ yields

$$\frac{\tau}{\frac{1}{c}\frac{\lambda^2}{\Delta\lambda}} \ll 1. \qquad (3.7)$$

Thus, when τ is long compared to $\tau_c \equiv \frac{1}{c}\frac{\lambda^2}{\Delta\lambda}$, which is always the case for optical frequencies, there is no observable interference between two spectral components, i.e., the spectral components combine incoherently and the total intensity is $i + i'$. τ_c is called the coherence time and $l_c = c\tau_c = \lambda^2/\Delta\lambda$ is the length of coherence.

The arguments above are true for any two spectral components of a broad spectrum[1].

[1]The definition of bandwidth for a broad band is somewhat arbitrary. In our argument bandwidth means that there are not significant spectral components farther apart than $\Delta\lambda$ in the band.

APPENDIX D

SURFACE BRIGHTNESS PARAMETER

We show how to derive the equation used by Barnes and Evans (1976) to define the surface brightness parameter F_V.

Start with

$$\pi f = \pi F \frac{\phi^2}{4}. \tag{4.1}$$

πf and πF are the bolometric flux (erg cm^{-2}s^{-1}) at the Earth and at the surface of a star, respectively, and ϕ is the apparent angular diameter of the star in mas. Using the relations

$$\pi f = const.10^{-0.4 m_{bol}} \tag{4.2}$$

and

$$\pi F = \sigma T_e^4 \tag{4.3}$$

and

$$m_{bol} = V_0 + C \tag{4.4}$$

by substituting into 4.1 and taking the logarithm, we obtain

$$-0.4\,(V_0 + C) + const. = 4 \log T_e + 2 \log \phi. \tag{4.5}$$

By rearranging the equation and calibrating for the Sun ($T_e = 5800$ K, $\phi = 959.63$", $m_{bol\odot} = -26.85$, we find $const = 4.2207$ and thus obtain the equation

$$\log T_e + 0.1C = 4.2207 - 0.1V_0 - 0.5 \log \phi. \tag{4.6}$$

F_V which is the surface brightness parameter is defined as the right-hand side of the equation. F_V is linearly related to the unreddened visual magnitude V_0 and can be calculated for stars of known angular diameter.

REFERENCES

Barbe, D. F. 1976, in Solid State Imaging, ed. P. G. Jespers, F. Van de Wiele, and M. H. White (Leyden, The Netherlands, Nordhoff).

Barnes, T. G., Evans, D. S. 1976, MNRAS, **174,** 489.

Barnes, T. G., Evans, D. S., & Parsons, S. B. 1976, MNRAS, **174,** 503.

Barnes, T. G., Evans, D. S., & Moffet, T. J. 1978, MNRAS, **183,** 285.

Behr, A. 1981, in Landolt & Börnstein, VI/2a, Ed. K. Schaifers and H. H. Voigt, Springer, p. 24.

Born, M., & Wolf, E. 1975, *Principles of Optics,* Pergamon Press. Inc., New York.

Beran M. J & Oz-Vogt, J. 1994, in *Progress in Optics vol.* XXXIII, Ed. E. Wolf, North-Holland, p. 321.

Chamberlain, S., Savvas, G., Washkurrak, W. & Williams, D., 1990, *Charge-coupled devices and solid state optical sensors*, Proc. of SPIE, (A91-37528 15-33), Bellingham, WA.

Cousins, A. W. J., Guelke, R. 1953, MNRAS, **113**, 776.

Di Benedetto, G. P., Rabbia, Y. 1987, A&A, **299**, 243.

Di Benedetto, G. P. 1993 ApJ, **270**, 315.

Diercks, H., Hunger, K. 1952, Zs. f. Ap, **31**, 182.

Dravins, D., Lindgren, L. & Mezey, E. 1997, PASP, **109**, 173.

Dyck, H. M., Benson, J. A., Ridgway, S. T., & Dixon, D. J. 1992, AJ, **104**, 1982.

Eddington, A. S. 1909, MNRAS, LXIX. 3, 178.

Evans, D. S., Heydenrych, J. C. R., & van Wyk, J. D. N. 1953, MNRAS, **113**, 781.

Evans, D. S. 1955, AJ, **60**, 432.

Evans, D. S. 1970, AJ, **75**, 589.

Evans, D. S. 1971, AJ, **76**, 1107.

Evans, D. S., Edwards, D. A., Frueh, M., McWilliam, A., & Sandmann, W. H. 1985, AJ, **90**, 2360.

Flatté, S. M. & Wang, G. 1993, JOSA A, **10**, 11.

Flatté, S. M., Bracher, C. & Wang, G. 1994, JOSA A, **11**, 7.

Fried, D. L. 1966, JOSA, **56**, 1372.

Gies, D. R., McKibben, W. P., Kelton, P. W., Opal, C. B., & Sawyer, S. 1990, AJ, **100**, 1601.

Gozani, J. 1985, JOSA, **2**, 12.

Hetmanzev, G. G. & Ginzburg, V. L. 1950, J. Exp. Theoret. Phys. (in Russian), **20**, 347.

Holst, G. C. 1996, *CCD Arrays, cameras, and displays*, SPIE.

Hoyle, F. 1958, *Paris Symposium on Radio Astronomy*, 529.

Hufnagel, R. E. 1974, in *Technical Digest, Topical Meeting on Optical Propagation through Turbulence*, OSA, Washington, DC.

Ishimaru, A. 1978, *Wave Propagation and Scattering in Random Media*, Academic Press, New York.

Jackson, J. 1950, Observatory, **70**, 215.

Janesick, J. R. 1991, *CCD Camera Design and Application*, SPIE Short Courses 44.

Lang, K. R. 1971, in *Highlights of Astronomy*, ed. C. de Jager, Dordrecht, Reidel, p. 626.

Leinert, Ch., Haas, M., Richichi, A., Zinnecker, H. & Mundt. R. 1991, A&A, **250**, p. 407.

Mackay, C. D. 1982, in *Istrumentation in Astronomu IV*, SPIE, **331**.

MacMahon, P. A. 1908, MNRAS, LXIX 2, 126

Mason, B. 1994, Ph.D. Dissertation, CHARA, Georgia State University.

Martin, J. M. & Flattó, M. 1988, Appl. Opt. **27**, 2111.

McAlister, H. A. 1985, *Ann. Rev. Astron. Astrophys.,* **23,** p. 59.

Moffet, T. J., Barnes, T. G., & Evans, D. S. 1978 AJ, **83**, 820.

Morbey, C. L. 1972, Pub. Dom. Ap. Obs., **14**, 45.

Morbey, C. L. 1974, AJ, **79**, 1304.

Mozurkewich, D. *at al.* 1990, AJ, **101**, 2207.

Murdin, P. 1971, ApJ, **169**, 615.

Nather, R. E., Evans D. S. 1970, AJ, **75**, 575.

Nather, R. E. 1970, AJ, **75**, 583.

Nather, R. E., McCants, M. M. 1970, AJ, **75**, 963.

Richichi, A. 1987, Mem. S. A. It., **58,** 431.

Richichi, A. & Lisi, F. 1990, A&A, **230**, 355.

Richichi, A. & Lisi, F. & Giacomo, A. Di. 1990, A&A, **254**, 149.

Richichi, A. 1993, *IAU Symp.* **158**, p. 71.

Richichi, A., Calamai, G., & Leinert, Ch. 1994, A&A, **286**, 829.

Richichi, A., Baffa, C., Calamai, G., & Lisi, F. 1996, AJ, **112**, 2786.

Richichi, A., Calamai, G., Leinert, Ch., Stecklum, B., & Trunkovsky, E. M. 1994, A&A, **309**, 163.

Ridgway, S. T. 1977, AJ, **82**, 511.

Ridgway, S. T., Joyce, R. R., White, N. M., & Wing, R. F. 1980, ApJ, **235**, 126.

Ridgway, S. T., Jacoby, G. H., Joyce, R. R., Siegel, M. J., & Wells, D. C. 1982, AJ, **87**, 680.

Rytov, S. M., Kravtsov, Yu. A. & Tatarski, V. I. 1989, *Principles of Statistical Radiophysics 4. Wave Propagation Thrrough Random Media*, Sringer, Berlin.

Scheuer, P. A. G. 1962, Austral J. Phys, **15,** 333.

Simon, D. A., Hodapp, K. W., Becklin, E. E. 1990, ApJ, **360**, 106.

Simon, M., Chen, W. P., Howell, R. R., Benson, J. A., & Slowik, D. 1992, ApJ, **384**, 212.

Schmidtke, P. C., Personal communication.

Stecklum, B. 1987, AJ, **94**, 201.

Sturmann, L. 1994, PASP, **106**, 1165.

Tatarski, V. I. 1961, *Wave Propagation in a Turbulent Medium*, McGraw-Hill, New York.

Tatarski, V. I. 1971, *The Effects of Turbulent Atmosphere on Wave Propagation*, U.S. Dept. of Commerce, TT-68-50464, Springfield, Virginia.

Uscinski, B. J. 1977, *The elements of Wave Propagation in Random Media*, McGraw-Hill, New York.

Véron-Cetty, M. P., Véron, P. 1991, ESO Scientific Reports #10.

Warner, B., *High Speed Astronomical Photometry*, Cambridge Univerity Press, Cambridge, 1988.

Washkurak, W., William, D., Chamberlain, S. & Savvas, G. 1989, in *Current Developments in Optical Engineering and Commercial Optics*, Eds. Robert E. Fischer, Harvey M. Pollicove & Warren J. Smith, Proc. SPIE, **1168**, p. 430.

Wesselink, A. J. 1969, MNRAS **158**, 1.

White, N. M. 1981, Lowell Obs. Bull. **167**, 60.

White, N. M., Feierman, B. H. 1987, AJ, **94**, 751.

Whitford, A. E. 1939, ApJ, **89**, 472.

Williams, J. D. 1939, ApJ, **89**, 467.

Zaratsky, D., Shectman, S. A. & Bredthauer, G. 1996, PASP, **108**, 104.